Technical Report

Pattern Recognition and Image Processing Group
Institute of Visual Computing and Human-Centered Technology
TU Wien
Favoritenstrasse 9-11/193-03
A-1040 Vienna AUSTRIA
Phone: +43 (1) 58801 - 18661
Fax: +43 (1) 58801 - 18697
E-mail: aysylu@prip.tuwien.ac.at
URL: http://www.prip.tuwien.ac.at/

PRIP-TR-156 5. Dezember 2022

From Circles to Generalized Conics: Enriching the Properties of 2D Shape Representation and Description

(improved version of the dissertation)

Aysylu Gabdulkhakova[1]

[1]Supported by Vienna PhD School of Informatics

Abstract

Like every type of human activity, research is intertwined with knowledge and experience. It aims at systematic exploration of phenomena in order to expand views and possibilities of solving a particular problem. In computer vision, the conventional way of measuring the distance between two objects is to find a pair of closest points belonging to them. When using the Euclidean metric, the equidistant set of a point is a circle. This thesis presents the alternative solutions (with an emphasis on 2D space), involving the implications for shape representation and description. They rely on other types of equidistant sets: conics (ellipse and hyperbola) and generalized conics (multifocal ellipse and hyperbola).

The first solution rests on the fact that a circle is a special case of an ellipse, implying a pair of coinciding focal points. Among the variety of ellipse properties, a constant distance sum to the pair of focal points enables defining a metric. It measures the distance between a point and a line segment bounded by the focal points. This metric defines an increment in the line segment length when moving from one focal point to another through the point of interest. The immediate advantages over the classical approach are computational efficiency and independence of the line segment discretization.

The second solution exhibits the key property of multifocal ellipse – each of its points has the same distance sum to the set of focal points. This concept alternatively defines the distance from a point to the collection of points. Such an interpretation is valuable in optimization problems, which can, in turn, benefit from efficient image processing techniques for solving their tasks.

The third solution reflects a necessity in image processing techniques like skeletonization not only to find the distance to an object but also to find a set of points that are equidistant from a pair of objects. By definition, a multifocal hyperbola contains the points that have a constant difference between the distance sums to the pair of point sets. Assuming the focal point to be any geometric shape, the multifocal hyperbola with the associated zero distance value is an equidistant set to the pair of objects.

The central notion behind this thesis is a generalization. Starting with a circle, a special case of an ellipse, it considers a generalized conic – a further conceptual extension. This transformation is reflected in the analysis of the geometric properties of these curves: from the conventional facts to the innovative findings. Such an approach enables explaining the existing and proposed methodologies through a prism of the single theoretical framework.

Contents

List of Acronyms

CED	Confocal-Ellipse-based Distance. 9, 14–17, 52–56, 58, 71, 79–82, 87, 88, 91, 92, 95, 96, 108, 136
CEF	Confocal Elliptic Field. 16, 18, 52, 57–60, 62–64, 66–68, 70, 73, 86, 130, 136, 137
$\mathrm{CEF}_{\mathrm{DT}_1}$	Confocal Elliptic Field in terms of DT_1. 75–77, 82, 86
$\mathrm{CEF}_{\mathrm{DT}_2}$	Confocal Elliptic Field in terms of DT_2. 72, 73, 76, 79–86, 101, 119
$\mathrm{CEF}_{\mathrm{DT}_\infty}$	Confocal Elliptic Field in terms of DT_∞. 76–78, 82, 86
$\mathrm{CEF}_{\mathrm{DT}}$	Confocal Elliptic Field in terms of DT. 16, 18, 73–76, 78, 79, 81, 86, 137
CI	Center of the Incircle. 92–94, 113
CMEF	Confocal Multifocal Elliptic Field. 16, 18, 52, 65, 67, 68, 70, 73, 86, 130, 131, 136, 137
$\mathrm{CMEF}_{\mathrm{DT}_2}$	Confocal Multifocal Elliptic Field in terms of DT_2. 73, 80, 81, 85, 86
$\mathrm{CMEF}_{\mathrm{DT}}$	Confocal Multifocal Elliptic Field in terms of DT. 18, 78, 79, 81, 82, 86, 137
CMHF	Confocal Multifocal Hyperbolic Field. 16, 18, 52, 65–68, 70, 73, 86, 130, 131, 136, 137

List of Mathematical Notations

(P, Q)	Line segment defined only by the endpoints P and Q. 58, 61, 72
$\overline{PQ}$	Line segment connecting points P and Q. 20, 22, 31, 32, 46, 54, 56, 58, 59, 61–64, 71, 72, 74, 77, 78, 80, 93–99, 105, 113, 115, 124
$\langle , \rangle$	Scalar (or dot) product. 19
$\mathsf{C}(O; r)$	Circle with the center at O and the radius r. 25, 95, 96, 109
$\mathsf{E}(F_1, F_2; a)$	Ellipse defined by the focal points F_1 and F_2 and the length of the semi-major axis a. 24, 27, 55
$\mathsf{E}(a)$	Member of a family of confocal ellipses. Parameter a denotes the length of the semi-major axis. 27, 28, 53–55
$\mathsf{H}(F_1, F_2; a)$	Hyperbola defined by the focal points F_1 and F_2 and the length of the semi-transverse axis a. 26, 27
$\mathsf{H}(a)$	Member of a family of confocal hyperbolas. Parameter a denotes the length of the semi-transverse axis of a hyperbola. 27, 28

$\mathsf{ME}(w_1F_1, ..., w_NF_N; c)$	Multifocal ellipse defined by N focal points $F_1, F_2, ..., F_N$, their corresponding weights $w_1, w_2, ..., w_N$ and the distance value c. 30, 31, 36, 45, 46
$\mathsf{ME}(c)$	Member of a family of confocal multifocal ellipses. Parameter c denotes the total distance sum to the focal points. 35
$\mathsf{MH}(w_1F_1, ..., w_NF_N \vert \nu_1G_1, ..., \nu_MG_M; c)$	Multifocal hyperbola defined by the two sets of focal points, $\mathcal{F} = \{w_1F_1, ..., w_NF_N\}$ and $\mathcal{G} = \{\nu_1G_1, ..., \nu_MG_M\}$ and the distance value c. 33, 43, 48
$\mathsf{MH}(c)$	Member of a family of confocal multifocal hyperbolas. Parameter c denotes the absolute difference between the distance sums to two sets of focal points. 35, 42, 43
$\mathsf{P}(F, l)$	Parabola defined by the focal point F and the line l. 22
ε	Eccentricity of a conic. 24, 26
f	Half of the distance between the focal points of an ellipse or a hyperbola. 23–26, 28, 54, 72
a	Length of the semi-major axis of an ellipse, or length of the semi-transverse axis of a hyperbola. 23–28, 54, 56, 72
b	Length of the semi-minor axis of an ellipse, or length of the semi-conjugate axis of a hyperbola. 24–27, 56, 72
$\mathcal{D}_{\mathcal{F}}$	Grayscale image representing the result of DT generated from the set of feature elements $\mathcal{F}$. 70
$\mathcal{D}_{\mathcal{F}}(P)$	Value of the pixel P in the distance field generated from the set $\mathcal{F}$. 71, 73, 83
$\mathcal{D}_F$	Distance field generated from the point F. 71, 73, 83, 85
R	Receptive field. 59
S_{ij}	Separating curve between the receptive fields R_i and R_j. 59

$\mathcal{DE}_{F_1F_2}$	Grayscale image representing the sum of two DT_2s generated from the feature elements F_1 and F_2. 71
$\overline{\mathcal{DE}}_{F_1F_2}$	Grayscale image representing the normalized sum of two DT_2s generated from the feature elements F_1 and F_2. The normalization is performed by subtraction of the length of $\overline{F_1F_2}$ from each pixel value. 71, 72, 83, 84
$\mathcal{DH}_{F_1F_2}$	Grayscale image representing the normalized difference of two DT_2s generated from the feature elements F_1 and F_2. 71
$\mathcal{DR}$	Receptive field in discrete space. 72, 84
$\mathcal{DS}_{ij}$	Separating curve between the receptive fields $\mathcal{DR}_i$ and $\mathcal{DR}_j$ in discrete space. 72, 84
τ	Threshold. 72, 84
$\mathsf{d}_{CED}(\mathsf{E}(a_1), \mathsf{E}(a_2))$	Confocal-Ellipse-based Distance (CED) between two confocal ellipses, $\mathsf{E}(a_1)$ and $\mathsf{E}(a_2)$. 53, 54, 57
$\mathsf{d}_{CED}(P, l)$	Distance from point P to line segment l in terms of CED. 54, 55, 58, 59, 61, 63, 77, 92, 96
$\mathsf{d}_{\infty}(P, Q)$	Chessboard distance between points P and Q. 74, 77, 78
$\mathsf{d}_1(P, Q)$	City-Block distance between points P and Q. 74, 77
$\mathsf{d}_2(P, Q)$	Euclidean distance between points P and Q. 20, 22, 24–26, 30, 33, 45–49, 52, 55, 58, 61–64, 71, 93–96, 99, 104, 105, 113–115
$\mathsf{d}_{HD}(P, l)$	Distance from a point P to a line segment l in terms of HD. 52, 89
I^2_{binary}	Two-dimensional binary image. 70–73, 82, 83
I^N	N-dimensional digital image. 68
$\mathbb{Z}_{\geq 0}$	Set of non-negative integer numbers. 68
$\mathbb{R}$	Set of real numbers. 19–22, 24–28, 30, 31, 33, 35, 45, 48, 52–54, 58, 59, 61, 62, 64, 68, 88, 89, 92, 109

$\mathcal{F}$	Set of objects. 57–59, 61, 65, 66, 70–73, 82–85, 88, 89, 91, 92
$\mathcal{VD}_{\mathcal{S}}$	Voronoi Diagram (VD) defined on the finite set of sites $\mathcal{S}$. 89
$\mathcal{VR}$	Voronoi region. 88, 89
$\mathcal{VR}^E$	Elliptic Line Voronoi region. 92

CHAPTER 1

Introduction

Do not disturb my circles!

Archimedes of Syracuse

Digitization of real-world objects considers simplifying their original properties in a format that a computer can process. Among the great variety of pictorial aspects, like color, texture, and motion, *shape* characterizes a silhouette. In this context, a 2D shape is a binary image defining a projection extent of 3D object onto a 2D plane. Processing the complete collection of shape pixels is a computationally expensive and cumbersome procedure. Thus, the shape is commonly further simplified by selecting an appropriate representation covering only the essential characteristics [47]. The result of this process is known as *shape representation.* It plays a crucial role in a broad spectrum of applications: document analysis, tumor recognition, analysis of particle trajectories, computer-aided design of mechanical parts and buildings, analysis of human gait, and fingerprint/face/iris detection [47].

This thesis explores the geometrical properties of conic sections (*ellipse*, *hyperbola*) and generalized conics (*egg-shape*, *hyperbolic shape*, *multifocal ellipse*, *multifocal hyperbola*). Such properties are analyzed from the computer vision perspective to enrich the capabilities of existing 2D shape representation methods. For example, one of the basic representations bounds the shape

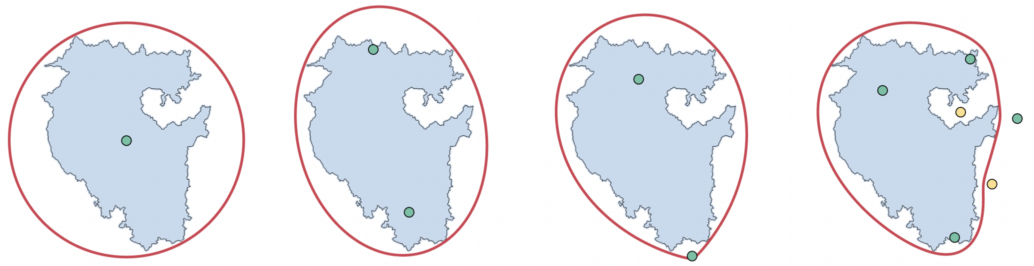

(a) circle (b) ellipse (c) egg-shape (d) multifocal hyperbola

Figure 1.1: Representing the shape with a primitive

with a geometric primitive [47]. In Figure 1.1a, the shape (blue) is represented by a *circle* (red), which requires the center position (green) and the radius to express the complete area of pixels. Since the shape is elongated, the circle contains a lot of background pixels. An *ellipse* (Figure 1.1b) is defined by the pair of focal points (green) and the distance value. Compared to the circle, the ellipse better approximates the shape and reflects its orientation and elongation. Providing the weight to one of the focal points creates an *egg-shape* (Figure 1.1c). It improves the ellipse representation by encoding additional semantic information – the shape becomes narrower while moving from top to bottom. Finally, having two sets of focal points, where one is considered as positively weighted (green) and the other – as negatively weighted (yellow), generates a *multifocal hyperbola* (Figure 1.1d). In contrast to the above primitives, it characterizes the shape concavity. In this example, the circle is the most compact representation, whereas the ellipse, egg-shape, and multifocal hyperbola contain less outliers and provide more semantic information.

Any point in space is mapped to a unique ellipse generated from a given pair of points [78]. This geometric property is used to compute a distance from a point to a line segment. Figure 1.2 illustrates two house shapes (blue). The wall is approximated by a line segment with two endpoints (red circles). Assuming the endpoints as focal points enables associating each pixel with a parameter of an ellipse that contains this pixel (left house in Figure 1.2). In classical aproaches, the line segment is expressed by all points belonging to it. The distance values propagate from these points as circles, and each pixel is mapped to a radius of a smallest circle (right house in Figure 1.2). The

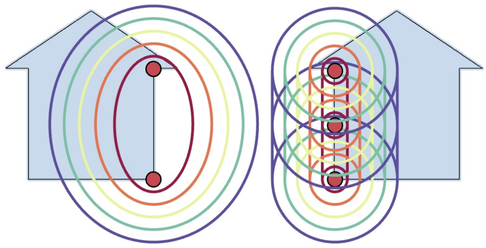

Figure 1.2: Distance from the house wall. The colors indicate distance values

clear benefits of ellipse-based metric are the independence of line segment discretization and computational simplicity. The applications include space tessellation (Chapter 6), shape representation with skeletons (Chapter 7), shape smoothing, and optimal path planning (Chapter 8). In addition, the ellipse-based metric enriches the classical representations by reflecting the relative line segment length.

1.1 Criteria for Shape Representation

A vast number of shape representation methods in the literature are broadly classified as *contour-based* and *region-based* [109,143,213]. The distinction lies in using points on the shape boundary [23,155] or also in its interior [28,29,180]. Costa et al. [47] distinguish the third group of approaches – *transform-based*. They cover techniques such as Fourier transform and represent the shape by the transform coefficients. Assuming the possibility of shape reconstruction from its representation, the methods are categorized as *information preserving* and *information non-preserving* [47,109]. The shape representation provides a basis for extracting semantically meaningful information for characterization, classification, or recognition. A process of collecting quantitative information about the object from its representation is called *characterization* or *shape description*. A selection of shape descriptor is influenced by the requirements of particular applications, desirable shape properties, and subjective factors, such as preferences and experience of researchers. The shape descriptors involve numeric characteristics, like an area, a perimeter, a thickness, a curvature of parts, and many more, which reasonably represent sufficient and relevant information for further analysis.

Several authors [33,114,208] defined a set of criteria to support systematic evaluation of various shape representations. The considered properties are qualitative, rather than quantitative, measures. Marr and Nishihara [114] emphasized the properties related to computational parameters (*accessibility*), robustness (*sensitivity, stability*), and applicability (*scope* and *uniqueness*) of methods. Brady [33] focused on relation between the global and local representations by considering characteristics such as *propagation, rich local support, smooth extension and subsumption.* Yang et al. [208] provided the requirements for efficiency and perceptual similarity with human intuition. Regarding the existing evaluation schemes [33, 114, 208], this thesis takes the following criteria into consideration:

- *scope* of representation defining shape classes where the corresponding technique is applicable;
- *uniqueness* indicating the presence of one-to-one mapping between the shape representation/description and the shape;
- *invariance* to transformations, such as translation, rotation, and scaling;
- *stability/robustness* to the impact of noise and occlusions;
- *accuracy* to preserve subtle shape details;
- *efficiency* in terms of computational complexity;
- *abstraction* of the representation to multiple scales or hierarchical levels.

1.2 Generalized Conics in Shape Representation

This thesis introduces the region- and contour-based shape representation and description concepts that rely on the geometric properties of conics and their generalizations. It explains the existing and proposed methods within the single theoretical framework. The central source of inspiration behind this work is the generalization property of ellipse: it can degenerate into a point, a line segment, and a circle. The metric Confocal-Ellipse-based Distance (CED) uses this property to measure the distance between a point and a line segment (Chapter 4-5).

CED provides valuable advantages over the classical space tessellation method called Voronoi Diagram (VD) (Chapter 6). The proposed Elliptic Line Voronoi Diagram (ELVD) avoids the decomposition of line segments with common endpoint since the obtained Voronoi edge does not contain an area. ELVD is a representation that implicitly prioritizes the acute angles and comparably long line segments. This property mitigates the effect of outliers and noise in skeletonization (Chapter 7) and is beneficial in the applications such as optimal path planning and contour smoothing (Chapter 8).

Generalizing the properties of conic sections by considering infinitely many focal points results in a powerful geometric object called generalized conic (Chapter 3). The discovered and derived properties broaden the scopes of shape representation and description. For instance, the new types of primitives, namely an egg-shape and a hyperbolic shape with corner, expand the possibilities to represent the shape. Compared to the ellipse, they require only one additional parameter – a weight at one of the focal points. Another example adopts the convexity property of multifocal ellipse to solve the optimization problems, such as optimal facility location (Chapter 8).

1.3 Structure of the Thesis and Contributions

Formalization of real-world scenarios in computer vision enforces a transition from continuous to discrete space. In particular, *discrete geometry* is a study of combinatorial, geometric, and topological properties of objects like points, lines, rectangles, ellipses, spheres, and cubes that are used in contrast to smooth surfaces [38]. *Digital geometry* is a branch of discrete geometry that has an expanding role in computer vision and computer graphics. It analyzes digitized objects (for instance, two-dimensional (2D) images and three-dimensional (3D) samples of the surface of the scanned objects) from the point of graph-theoretical and combinatorial concepts [94].

The necessity to develop computationally efficient data structures and algorithms for inherently geometric problems gave rise to *computational geometry* as an independent discipline in the 1970s. The fundamental concepts developed in this field are successfully used in various domains: robotics, computer graphics, geographic information systems, computer-aided design and manufacturing, and pattern recognition [49]. As a result, the term *computational geometry* has multiple domain-specific connotations [58, 62, 63, 118, 122, 151, 174]. In this thesis, the definition is adopted from [151] and [174] and considers a systematic study of data structures and algorithms for geometric problems from the point of their computational complexity. The synergy of the two disciplines, *discrete and computational geometry*, bridges the gap between mathematics and computer science [52]. For a problem that is geometric in nature, a successful application-driven solution takes two considerations into account [49]:

1. Understanding of geometric properties that are useful for the given problem.

2. Finding the appropriate data structures and algorithmic techniques that enable efficient usage of the above properties.

In relation to the thesis, Chapter 2 starts with the formal definitions of the basic mathematical notions that are sufficient for following the discussion. It further introduces the conic sections and their relevant properties. Chapter 3 expands the discussion towards the generalized conics. It presents not only the facts mentioned in the existing literature but also the geometric findings with a practical value in the computer vision domain.

Chapter 4 discusses the proposed metric, called Confocal-Ellipse-based Distance (CED), that computes the distance between a point and a line segment. Its properties are analyzed through a comparison with the classical approach, the Hausdorff Distance (HD). Afterwards, the chapter explores the properties of the distance field, the Confocal Elliptic Field (CEF), that relies on CED as a proximity measure. Eventually, the properties of generalized conics provide a basis for the creation of the Confocal Multifocal Elliptic Field (CMEF) and the Confocal Multifocal Hyperbolic Field (CMHF).

Chapter 5 establishes a connection between CEF and digital space. To compute the distance fields, it is proposed to apply the classical image processing technique, called Distance Transform (DT). In this regard, the resultant representation has the name Confocal Elliptic Field in terms of DT ($\mathrm{CEF}_{\mathrm{DT}}$). Due to the discrete nature of the approach, the properties of the original CEF are revisited. The underlying concept behind $\mathrm{CEF}_{\mathrm{DT}}$ is not limited to the use of the Euclidean distance. Therefore, $\mathrm{CEF}_{\mathrm{DT}}$ is discussed in relation to the metric impact on the resultant representation after substituting the Euclidean distance with City-Block and Chessboard.

Chapters 6 and 7 gain a deeper insight into the properties of CEF. The proposed Elliptic Line Voronoi Diagram (ELVD) and Elliptic Line Voronoi

Skeleton (ELVS) can be considered generalizations of the classical Voronoi Diagram (VD) and Voronoi Skeleton (VS).

The presented theoretical findings have a potential to be applied in the computer vision domain. Chapter 8 exemplifies the practical problems where the advantage of the developed techniques can be vividly illustrated.

This thesis summarizes the research work published in proceedings of the international conferences together with additional findings that improve understanding of the content:

1. Aysylu Gabdulkhakova, Walter G. Kropatsch: *Confocal Ellipse-based Distance and Confocal Elliptical Field for polygonal shapes.* In Proceedings of the International Conference on Pattern Recognition, pages 3025–3030, 2018 [66]

2. Aysylu Gabdulkhakova, Maximilian Langer, Bernhard W. Langer, Walter G. Kropatsch: *Line Voronoi Diagrams Using Elliptical Distances.* In Proceedings of the Joint IAPR International Workshop on Structural, Syntactic, and Statistical Pattern Recognition, pages 258–267, 2018 [69]

3. Aysylu Gabdulkhakova, Walter G. Kropatsch: *Generalized conics: properties and applications.* In Proceedings of the International Conference on Pattern Recognition, pages 10728–10735, 2020 [67]

4. Aysylu Gabdulkhakova, Walter G. Kropatsch: *Generalized conics with the sharp corners.* In Proceedings of the Iberoamerican Congress on Pattern Recognition, pages 419–429, 2021 [68]

The present work covers a wide range of topics starting with the theoretical discussions and finishing with the practical applications. Despite such a variety, the core value behind this thesis is the introduction of the generalized conics into the field of computer vision. The contributions can be listed as follows:

1. study of the geometric properties of conic sections and generalized conics;

2. analysis of an egg-shape and a hyperbolic shape with corners, and introduction of the method for deriving their parameters;

3. introduction of the metric CED and analysis of its properties;

4. introduction of the distance fields CEF, CMEF, and CMHF;
5. introduction of the discrete distance fields $\mathrm{CEF_{DT}}$, $\mathrm{CMEF_{DT}}$, and $\mathrm{CMHF_{DT}}$;
6. analysis of $\mathrm{CEF_{DT}}$ under City-Block and Chessboard distances;
7. reconsideration of CEF from the point of ELVD and analysis of the properties;
8. reconsideration of CEF from the point of ELVS and analysis of the properties;
9. comparison of the proposed representations with the state-of-the-art;
10. demonstration of the computer vision applications using the derived concepts.

CHAPTER 2

Conics in Analytic Geometry

This chapter covers the mathematical notions and properties underlying this research work. In the beginning, it introduces the basic concepts that give a solid foundation to follow the discussion about conics with a special emphasis on an ellipse and a hyperbola. The description of each type of conics accounts for nomenclature and geometric properties. In particular, the definitions of ellipse and hyperbola are the keystones to the proposed metric, whereas the concept of confocal conics - to the proposed distance field. Despite the variety of geometry branches, here, the focus is on the Euclidean and analytic geometry which are necessary for computer vision.

2.1 Preliminaries

This section briefly introduces the definitions and notations that facilitate understanding of the work.

Definition 1 (Euclidean space)**.** *Euclidean space is the finite N-dimensional vector space, $\mathbb{R}^N$, with a scalar (or dot) product. The scalar product is a function $\langle , \rangle : \mathbb{R}^N \times \mathbb{R}^N \rightarrow \mathbb{R}$, such that for any elements $x,\ y,\ z \in \mathbb{R}^N$ the following axioms hold true:*

1. $\langle x, y \rangle = \langle y, x \rangle$ *– symmetry*

2. $\langle x+z, y\rangle = \langle x, y\rangle + \langle z, y\rangle$ – *distributivity*

3. $\langle \alpha x, y\rangle = \alpha\langle x, y\rangle$, $\alpha \in \mathbb{R}$ – *linearity in the first argument*

4. $\langle x, x\rangle \geq 0$, $\langle x, x\rangle = 0 \Leftrightarrow x = 0$ – *positive-definiteness*

Definition 2 (Point)**.** *A point P is a primitive notion in the Euclidean space that has no dimensional attributes, like length, area, or volume.*

Definition 3 (Line segment)**.** *A line segment $\overline{PQ}$ is a straight path connecting a pair of points P and Q. It has a one-dimensional attribute which is a length.*

A coordinate system is a method that enables defining the position of a point in space numerically. Such a concept makes it possible to solve geometric problems analytically.

Definition 4 (Cartesian coordinates)**.** *A Cartesian coordinate system (also called rectangular coordinates) defines N mutually perpendicular axes with the common origin O. A point is defined by an N-tuple of real numbers $P = (p_1, p_2, ..., p_N)$, called coordinates, that express the signed distances from the origin.*

The Euclidean distance (also referred to as L_2-metric) measures the line segment length in the Cartesian coordinates.

Definition 5 (Euclidean distance)**.** *The Euclidean distance between two points in the Euclidean space, $P = (p_1, p_2, ..., p_N)$ and $Q = (q_1, q_2, ..., q_N)$, is defined as:*

$$\mathsf{d}_2(P, Q) = \sqrt{(p_1 - q_1)^2 + (p_2 - q_2)^2 + ... + (p_N - q_N)^2} \tag{2.1}$$

Definition 6 (Barycentric coordinates)**.** *A barycentric coordinate system defines a point with the reference to an N-simplex expressed by the vertices $V_1,\ V_2, \ldots,\ V_{N+1}$. If placing the masses $m_1, m_2, ..., m_{N+1}$ at the vertices makes P the center of mass of the N-simplex (or the barycenter), then the $(N+1)$-tuple $(m_1 : m_2 : ... : m_{N+1})$ is called homogeneous barycentric coordinates.*

Property 1 (Multiplying the barycentric coordinates by a non-zero constant)**.** *The points $P = (m_1 : m_2 : ... : m_{N+1})$ and $Q = (km_1 : km_2 : ... : km_{N+1})$ are the same, thus, multiplying the barycentric coordinates by the non-zero scalar value k has no effect [46].*

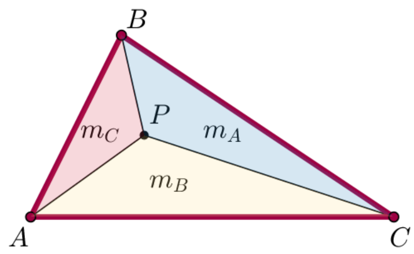

Figure 2.1: Interpreting the barycentric coordinates by the areas of sub-triangles

Property 2 (Geometric interpretation of the barycentric coordinates)**.** *Let $P = (m_A : m_B : m_C)$ be the barycenter of the 2-simplex formed by the vertices A, B, and C with the corresponding masses m_A, m_B, and m_C. The areas of the sub-triangles $\triangle PBC$, $\triangle PAC$, and $\triangle PAB$ are proportional to the barycentric coordinates of P (Figure 2.1) [46]:*

$$m_A = \frac{\Delta_{PBC}}{\Delta_{ABC}},\ m_B = \frac{\Delta_{PAC}}{\Delta_{ABC}},\ m_C = \frac{\Delta_{PAB}}{\Delta_{ABC}} \tag{2.2}$$

Definition 7 (Metric)**.** *A metric is a function $\mathbb{R}^N = \mathbb{R}^N \times \mathbb{R}^N \to \mathbb{R}$ such that every two elements $X, Y \in \mathbb{R}^N$ are associated with a unique non-negative number, which satisfies the following conditions (axioms of the metric space):*

1. *non-negativity:* $\rho(X, Y) \geq 0$
2. *identity of indiscernibles:* $\rho(X, Y) = 0 \Longleftrightarrow X = Y$
3. *symmetry:* $\rho(X, Y) = \rho(Y, X)$
4. *triangle inequality:* $\rho(X, Y) + \rho(Y, Z) \geq \rho(X, Z)$, $\forall Z \in \mathbb{R}^N$

Definition 8 (Level set)**.** *A level set is defined by the points where the given function takes on a particular value.*

2.2 Conic Sections

The classical definition of *conic sections*, or *conics*, considers an intersection of a plane with a (circular) double napped cone [78].

Definition 9 (Right circular cone)**.** *Consider a triangle $\triangle AVV'$ with the right angle $\widehat{VV'A}$. Rotating $\triangle AVV'$ about $\overline{VV'}$ creates a right circular cone. The point V is called vertex and a line containing $\overline{VV'}$ is called cone axis.*

Definition 9 describes a special cone that is sufficient for the discussion of conic sections. The general definition is provided in [70].

Definition 10 (Double napped cone)**.** *A double napped cone is a surface obtained by placing a pair of cones in a way that their vertices and axes coincide. In this case, each cone is called nappe.*

Definition 11 (Conic section)**.** *A conic section, or a conic, is a curve formed at the intersection of a double napped cone with a plane that does not pass through its vertex [78].*

Figure 2.2 shows the intersections (red) of the double napped right circular cone (blue) with the plane (gray). Slicing one nappe produces either an ellipse (Figure 2.2a) or a parabola (Figure 2.2c). A circle is a special case of the ellipse, obtained by cutting the nappe perpendicularly to the cone axis (Figure 2.2b). The plane intersection with both nappes creates a hyperbola (Figure 2.2d). In this thesis, a focus is on the ellipse and hyperbola.

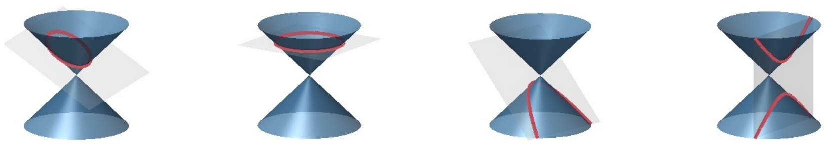

(a) ellipse (b) circle (c) parabola (d) hyperbola

Figure 2.2: The conic sections

2.2.1 Parabola

Visually, a parabola is a U-shaped curve that is mirror-symmetric with regard to some axis (Figure 2.3a). Here, l expresses a fixed line called *directrix*, while F is a fixed point called *focus*. The point V, called *vertex*, is an intersection between the parabola and its symmetry axis. The line segment between the focus and the vertex, $f = \mathsf{d}_2(F, V)$, defines the *focal distance*. Consider now the formal definition of this conic section.

Definition 12 (Parabola)**.** *A parabola, denoted as* $\mathsf{P}(F, l)$*, is the locus of points equidistant from both - the focus* F *and the directrix* l*:*

$$\mathsf{P}(F,l) = \{P \in \mathbb{R}^2 : \mathsf{d}_2(P,F) = \inf\{\mathsf{d}_2(P,L) \mid L \in l\}\} \tag{2.3}$$

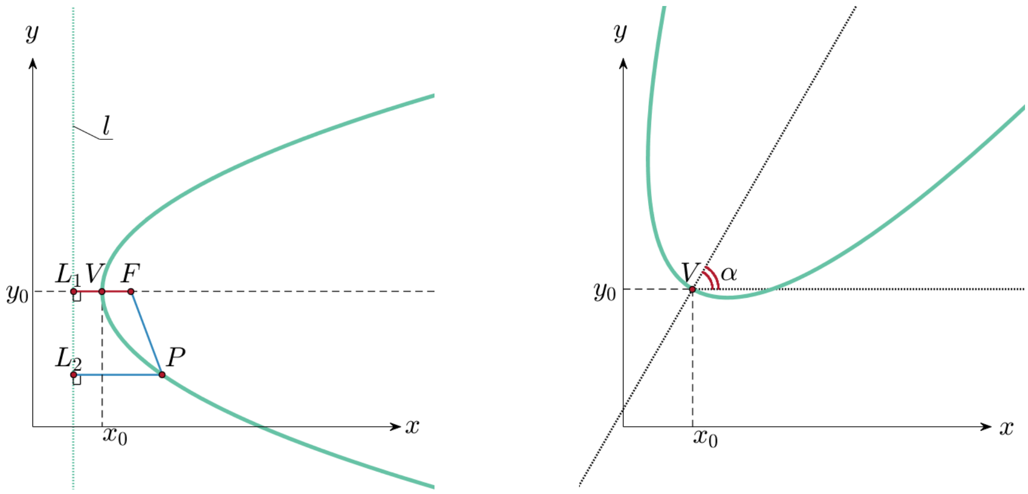

(a) translation by (x_0, y_0) (b) counterclockwise rotation by α

Figure 2.3: The parabola in the 2D Cartesian coordinate system

This is illustrated in Figure 2.3a. Let V be the vertex, P - an arbitrary point of the parabola, F - the focus, l - the directrix. Then, Definition 12 leads to the following equalities: $\mathsf{d}_2(V, L_1) = \mathsf{d}_2(V, F)$ and $\mathsf{d}_2(P, L_2) = \mathsf{d}_2(P, F)$.

Implicit Representation

The parabola rotated by the angle θ in the counterclockwise direction with the vertex $V(x_0, y_0)$, as shown in Figure 2.3b, is implicitly defined as:

$$((x - x_0)\sin\alpha + (y - y_0)\cos\alpha)^2 = 4f((x - x_0)\cos\alpha - (y - y_0)\sin\alpha) \tag{2.4}$$

Explicit Representation

Alternatively, the parabola is defined in the parametric form:

$$\begin{cases} x - x_0 = ft(t\cos\alpha - 2\sin\alpha) \\ y - y_0 = ft(t\sin\alpha + 2\cos\alpha) \end{cases}, \tag{2.5}$$

where t is a parameter that ranges from $-\infty$ to $+\infty$.

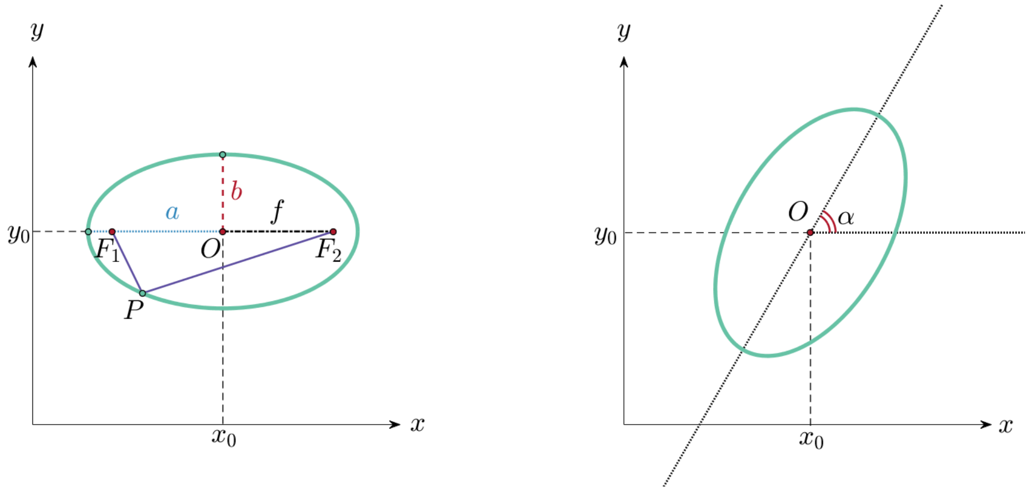

(a) translation by (x_0, y_0)

(b) counterclockwise rotation by α

Figure 2.4: The ellipse in the 2D Cartesian coordinate system

2.2.2 Ellipse

The ellipse in the 2D Cartesian coordinate system is shown in Figure 2.4a. It has two axes, *major* and *minor*, that intersect at the center O. The halves of the major and minor axes are referred to as *semi-major* and *semi-minor* axes correspondingly. The major axis has a length of $2a$ and passes through the focal points F_1 and F_2, which are located symmetrically at the distance f from the center. The minor axis is perpendicular to the major axis and has a length of $2b$. Formally this type of conic is defined below.

Definition 13 (Ellipse)**.** *An ellipse, denoted as* $\mathsf{E}(F_1, F_2; a)$*, is the locus of points such that the sum of their distances to two focal points* F_1 *and* F_2 *is constant:*

$$\mathsf{E}(F_1, F_2; a) = \{P \in \mathbb{R}^2 : \mathsf{d}_2(P, F_1) + \mathsf{d}_2(P, F_2) = 2a\} \tag{2.6}$$

The following equation makes a link between the parameters a, b, and f:

$$a^2 = b^2 + f^2 \tag{2.7}$$

Another way to relate these parameters is connected to *eccentricity*, denoted as ε. It shows the degree of ellipse elongation and is formally defined as:

$$0 \leq \varepsilon = \frac{\sqrt{a^2 - b^2}}{a} = \frac{f}{a} < 1 \tag{2.8}$$

As follows from (2.7) and (2.8), the length of the semi-major axis satisfies the condition $a > f = \frac{1}{2}\mathsf{d}_2(F_1, F_2)$. In the special cases, the ellipse degenerates into a circle ($f = 0$, $\varepsilon = 0$, $b = a$) and into a line segment ($f \to a$, $\varepsilon \to 1$, $b \to 0$).

Definition 14 (Circle)**.** *A circle, denoted as* $\mathsf{C}(O; r)$*, is the locus of points which distance to the point* O *is constant:*

$$\mathsf{C}(O; r) = \{P \in \mathbb{R}^2 : \mathsf{d}_2(P, O) = r\} \tag{2.9}$$

Implicit Representation

Consider the ellipse in the 2D Cartesian coordinate system rotated by the angle α in the counterclockwise direction about its center at $O(x_0, y_0)$ (Figure 2.4b). Then, each point $P(x, y) \in \mathbb{R}^2$ of the ellipse satisfies the following equation:

$$\frac{((x - x_0)\cos\alpha - (y - y_0)\sin\alpha)^2}{a^2} + \frac{((x - x_0)\sin\alpha + (y - y_0)\cos\alpha)^2}{b^2} = 1 \tag{2.10}$$

Explicit Representation

Alternatively, the ellipse is parametrically defined as:

$$\begin{cases} x - x_0 = a\cos\theta\cos\alpha - b\sin\theta\sin\alpha \\ y - y_0 = a\cos\theta\sin\alpha + b\sin\theta\cos\alpha \end{cases}, \tag{2.11}$$

where θ is a parameter that ranges from 0 to 2π.

2.2.3 Hyperbola

As illustrated in Figure 2.5a, the hyperbola contains two non-intersecting curves, called *branches* [78]. Observe the shortest line segment connecting the branches. Its two endpoints, V_1 and V_2, are called *vertices*, and its midpoint O is called *center*. Notice the two lines intersecting each other at the center. While moving away from the center, they approach the hyperbola branches. These lines are called *asymptotes*. The hyperbola has two axes: *transverse* and *conjugate* [108]. The transverse axis is formed by the line segment connecting the vertices V_1 and V_2. This line segment has a length of $2a$. The conjugate axis is perpendicular to the transverse axis. Here, b is the distance between

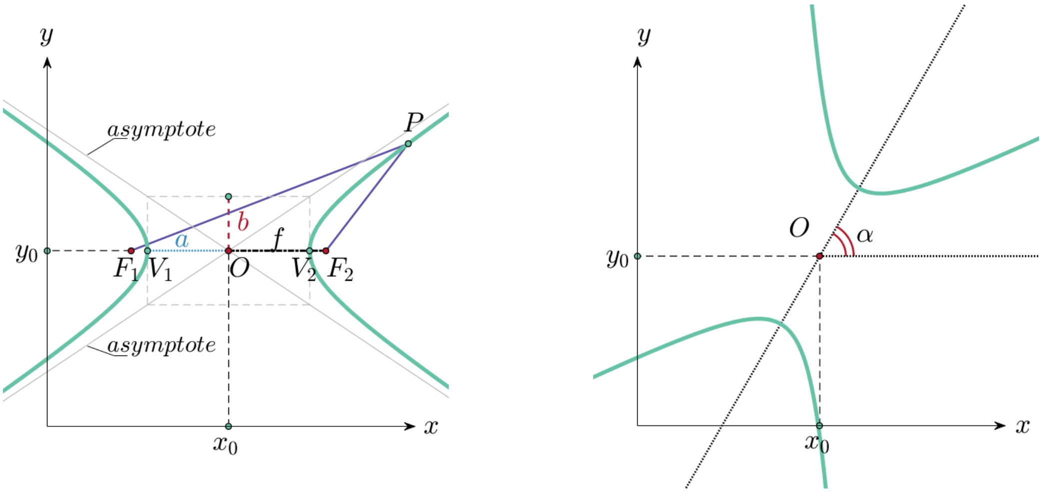

(a) translation by (x_0, y_0)

(b) counterclockwise rotation by α

Figure 2.5: The hyperbola in the 2D Cartesian coordinate system

the vertex and intersection point of the two lines: the asymptote and tangent to the hyperbola branch passing through that vertex. The focal points, F_1 and F_2, belong to the line containing the vertices. They are symmetric to each other with respect to the center. The half of the distance between the focal points is denoted as f. The hyperbola branches are symmetric regarding the transverse and conjugate axes [78].

Definition 15 (Hyperbola)**.** *A hyperbola, denoted as* $\mathsf{H}(F_1, F_2; a)$*, is the locus of points with the constant absolute difference between the distances to the focal points* F_1 *and* F_2*:*

$$\mathsf{H}(F_1, F_2; a) = \{P \in \mathbb{R}^2 : |\mathsf{d}_2(P, F_1) - \mathsf{d}_2(P, F_2)| = 2a\ \} \tag{2.12}$$

Compared to the ellipse (2.7), the relation between a, b, and f is:

$$f^2 = a^2 + b^2 \tag{2.13}$$

The *eccentricity* value of hyperbola, ε, is computed as:

$$1 < \varepsilon = \frac{\sqrt{a^2 + b^2}}{a} = \frac{f}{a} \tag{2.14}$$

When ε tends to 1, the branches flatten along the line containing the transverse axis. With the growth of ε to infinity, the branches approach lines parallel to the conjugate axis until they degenerate into the line.

Property 3. *The tangent to a hyperbola branch at the vertex is perpendicular to the transverse axis [108].*

Implicit Representation

Assume the hyperbola rotated by α degrees in the counterclockwise direction about its center at $O(x_0, y_0)$ (Figure 2.5b). Each of its points $P(x, y) \in \mathbb{R}^2$ satisfies the equation:

$$\frac{((x-x_0)\cos\alpha-(y-y_0)\sin\alpha)^2}{a^2}-\frac{((x-x_0)\sin\alpha+(y-y_0)\cos\alpha)^2}{b^2}=1 \tag{2.15}$$

Explicit Representation

The parametric form defining the hyperbola is:

$$\begin{cases} x-x_0=\pm a\cosh\theta\cos\alpha-b\sinh\theta\sin\alpha \\ y-y_0=\pm a\cosh\theta\sin\alpha+b\sinh\theta\cos\alpha \end{cases}, \tag{2.16}$$

where the parameter $\theta \in \mathbb{R}$.

2.3 Confocal Conics

The previous section discusses each conic section and its properties individually. Here, in contrast, the focus is on a family of conics that share the same focal points and have various associated sums of the distances (Figure 2.6a).

Definition 16 (Confocal ellipses (or hyperbolas))**.** *The ellipses (or hyperbolas) sharing the common focal points, F_1 and F_2, are called confocal ellipses (or hyperbolas).*

As follows from Definition 16, when related to the confocal ellipses (or hyperbolas), the original ellipse or hyperbola notation $\mathsf{E}(F_1, F_2; a)/\mathsf{H}(F_1, F_2; a)$ is simplified by using only the parameter a. In other words, $\mathsf{E}(a)/\mathsf{H}(a)$.

Property 4 (Uniqueness of confocal ellipse and hyperbola passing through a point)**.** *Given any point $P \in \mathbb{R}^2$ there is exactly one level set from the family of confocal ellipses (hyperbolas) that passes through it [78]:*

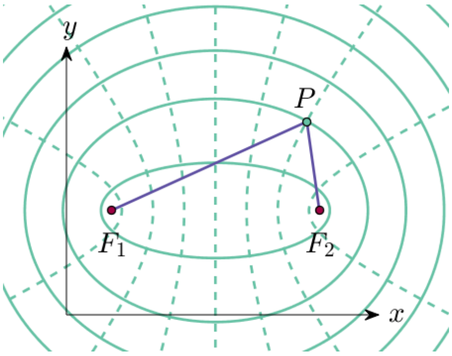

(a) confocal conics

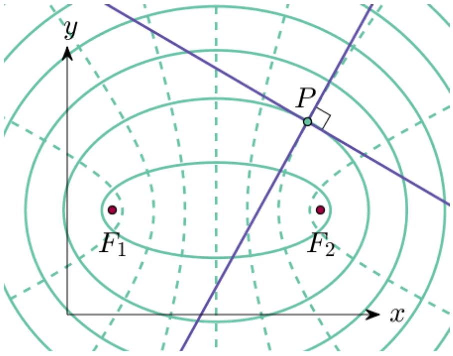

(b) orthogonality of the tangents at P

Figure 2.6: The confocal ellipses (solid) and hyperbolas (dashed) from the focal points F_1 and F_2. Here, P is an intersection point of the ellipse and the hyperbola

$$\bigcup_{a>f} \mathsf{E}(a) = \mathbb{R}^2 \tag{2.17}$$

$$\bigcup_{0<a<f} \mathsf{H}(a) = \mathbb{R}^2 \tag{2.18}$$

Property 5 (Confocal ellipse and hyperbola intersect orthogonally)**.** *The tangents to the confocal ellipse and hyperbola at the point of their intersection are mutually orthogonal [78] (Figure 2.6b).*

According to Properties 4 and 5, the families of confocal ellipses and hyperbolas form the orthogonal coordinate system, called *elliptic coordinate system* [78]. It has an application in, for instance, astronomy [50] and physics [188, 196].

CHAPTER 3

Generalized Conics in Analytic Geometry

This chapter is based on the following publications:

Aysylu Gabdulkhakova, Walter G. Kropatsch:
Generalized conics: properties and applications. In Proceedings of the International Conference on Pattern Recognition, pages 10728–10735, 2020 [67]

Aysylu Gabdulkhakova, Walter G. Kropatsch:
Generalized conics with the sharp corners. In Proceedings of the Iberoamerican Congress on Pattern Recognition, pages 419–429, 2021 [68]

The conics can be generalized into a class of higher-order curves by taking infinitely many focal points. Each focal point is associated with a real number that reflects its weight. First generalization modifies Definition 13 to have a constant sum of the weighted distances to the set of focal points [71,75,120,172]. Second generalization is based on Definition 15 and takes two sets of focal points with weights. A level set satisfies the constant absolute difference of weighted distance sums to the points in these sets [71, 120]. In the literature, there is a variety of other generalizations. Nagy et al. [127,201] introduced an additional division of the constant sum by the set size, so the level sets reflect the average distances to the set of focal points. Glaeser et al. [71] considered the weighted distance sums, as well as the weighted sums of distance products. Lamé curves [99] show a different way of generalization by substituting the degree of 2 in the equation (2.10) with the degree of N, where N is a rational number. In the special case, where N is strictly greater than 2 [74], these curves are referred to as superellipses. By increasing the degree, the shape gradually transforms to a rectangle [83]. As compared to the generalized conics, superellipses neither consider varying the number of focal points, nor preserve the constant distance sum to focal points. The latter is clear on an example of a square (the special case of a rectangle): a distance from its center to a point at a corner is greater than to any other point of this square.

Regarding the naming conventions, the generalized conics are referred to as polyconics [120] or multifocal curves [71]. For the constant weighted distance sums, there exist works about polyellipses [120], multifocal ellipses [60, 71], n-ellipses [172], Tschirnhaus´sche Kurven [194], k-ellipses [131], egglipses [164], Cartesian ovals [206] and ovals [116]. For the constant absolute differences of weighted sums, there are references to generalized [75] and multifocal [71] hyperbolas. This thesis respects the following nomenclature. The generalized conics are curves satisfying the equidistance properties of conics applied to sets of focal points. To distinguish various types of the generalized conics and emphasize the fact of having multiple focal points, it is proposed to use the terms *multifocal ellipse* and *multifocal hyperbola* for the generalizations of an ellipse and a hyperbola respectively.

The original motivation to study the topic appeared in the mathematical community. Nowadays, the generalized conics are applied in approximation theory [60], optimization problems [198,199,204], geometric tomography [201], and architecture [147]. This chapter discusses the geometrical properties of multifocal ellipses and hyperbolas, and presents the findings from the shape representation perspective.

3.1 Multifocal Ellipse

Definition 17 (Multifocal ellipse)**.** *A multifocal ellipse,* $\mathsf{ME}(w_1F_1, ..., w_NF_N; c)$, *is a generalization of the ellipse (the weights* $w_1, w_2, ..., w_N$ *are positive real numbers). It is a locus of points with a constant weighted distance sum to its* N *focal points:*

$$\mathsf{ME}(w_1F_1, ..., w_NF_N; c) = \{P \in \mathbb{R}^2 : \sum_{i=1}^{N} w_i \mathsf{d}_2(P, F_i) = c\} \tag{3.1}$$

Figure 3.1 shows the multifocal ellipses from the three focal points, F_1,

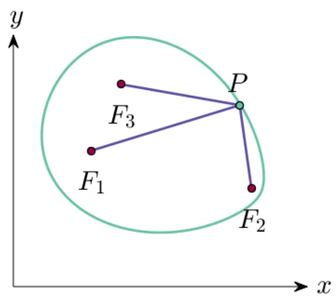

(a) $w_1 = w_2 = w_3 = 1$

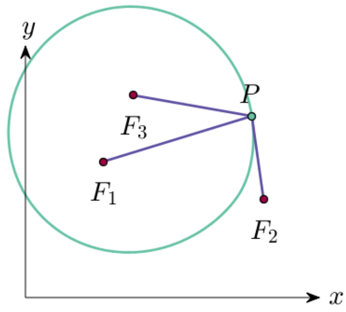

(b) $w_1 = 0.8$, $w_2 = 0.2$, and $w_3 = 1$

Figure 3.1: The multifocal ellipses, having the form $\mathsf{ME}(w_1F_1, w_2F_2, w_3F_3; c)$, that pass through the point P in the 2D Cartesian coordinate system

F_2, and F_3. Here, an arbitrary point $P \in \mathbb{R}^2$ plays the anchor role in the exemplification of the respective level set. Observe the change of the multifocal ellipse passing through P, when the focal points have identical (Figure 3.1a) and various (Figure 3.1b) weights.

Property 6 (Convexity and compactness of multifocal ellipse)**.** *A multifocal ellipse* $\mathsf{ME}(w_1F_1, ..., w_NF_N; c)$ *is convex and compact [139].*

Property 7 (Global minimum for non-collinear focal points)**.** *(3.1) reaches the global minimum at one point when the focal points are non-collinear [139] (the point M in Figure 3.2a).*

Property 8 (Global minimum for odd number of collinear focal points)**.** *(3.1) reaches the global minimum at $F_{\frac{N+1}{2}}$ if N is an odd number of ordered collinear focal points [139, 172] (the point F_3 in Figure 3.2b).*

Property 9 (Global minimum for even number of collinear focal points)**.** *(3.1) reaches the global minimum at all points of $\overline{F_{\frac{N}{2}}F_{\frac{N}{2}+1}}$ if N is an even number of ordered collinear focal points [172] (the line segment $\overline{F_3F_4}$ in Figure 3.2c).*

When dividing (3.1) by N, every point is mapped to arithmetic mean of the distances to the given set of focal points [127]. Together with Properties 6 to 9 it makes the multifocal ellipses useful for optimization tasks, such as Fermat-Torricelli [198, 199] and Weber [204] problems. In the literature, this task is also referred to as an optimal facility location problem [24] and is featured in Section 8.3.

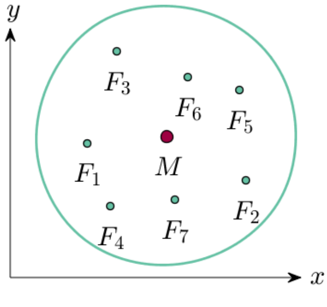

(a) non-collinear foci: at M

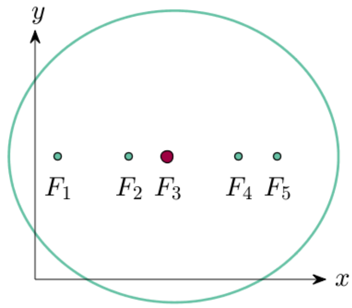

(b) odd number of collinear foci: at F_3

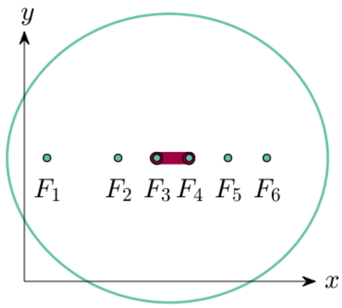

(c) even number of collinear foci: at $\overline{F_3F_4}$

Figure 3.2: The global minimum (minima) for the various sets of focal points

Property 10 (Multifocal ellipse tends to a circle at infinity)**.** *The multifocal ellipse approaches a circle when it infinitely grows in size.*

Property 10 stems from the observation that every focal point inside a finite area of $\mathbb{R}^2$ has the same distance to the points infinitely far away in space. Thus, these points are perceived as one. With regard to (3.1), the multifocal ellipse that is defined from a single focal point approaches a circle.

3.2 Multifocal Hyperbola

Definition 18 (Multifocal hyperbola)**.** *A multifocal hyperbola, denoted as* $\mathsf{MH}(w_1F_1, ..., w_NF_N|\nu_1G_1, ..., \nu_MG_M; c)$*, is a generalization of a hyperbola. It is defined on two sets of focal points,* $F_1, ..., F_N$ *and* $G_1, ..., G_M$*, with positive weights,* $w_1, ..., w_N$ *and* $\nu_1, ..., \nu_M$ *and expresses a locus of points such that the following absolute difference of the distance sums remains constant:*

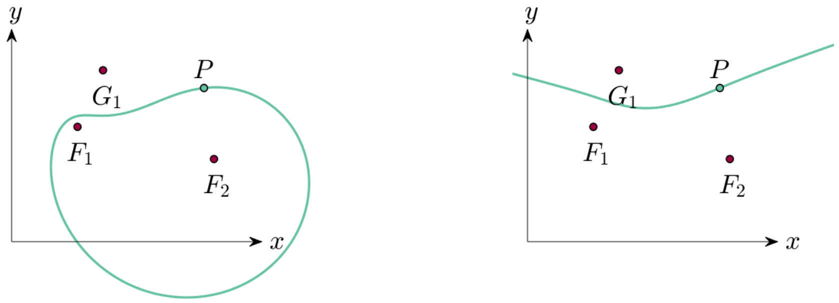

(a) $w_1 = w_2 = \nu_1 = 1$ (b) $w_1 = 0.8$, $w_2 = 0.2$, and $\nu_1 = 1$

Figure 3.3: The multifocal hyperbolas, having the form $\mathsf{MH}(w_1 F_1, w_2 F_2 | \nu_1 G_1; c)$, that pass through the point P in the 2D Cartesian coordinate system

$$\begin{aligned} \mathsf{MH}(w_1 F_1, ..., w_N F_N | \nu_1 G_1, ..., \nu_M G_M; c) = \\ \{P \in \mathbb{R}^2 : |\sum_{i=1}^{N} w_i \mathsf{d}_2(P, F_i) - \sum_{j=1}^{M} \nu_j \mathsf{d}_2(P, G_j)| = c\} \end{aligned} \tag{3.2}$$

For simplicity, the points $F_1, ..., F_N$ are referred to as positively weighted, and the points $G_1, ..., G_M$ – as negatively weighted.

Figure 3.3 demonstrates the examples of multifocal hyperbolas. The first set of focal points contains F_1 and F_2, whereas the second set – G_1. The level sets are passing through the arbitrary point $P \in \mathbb{R}^2$. Notice the difference between Figures 3.3a and 3.3b caused by the weights at the focal points. As can be concluded from (3.1) and (3.2), a multifocal hyperbola is a multifocal ellipse that accepts weights with the opposite signs, namely plus and minus. Nevertheless, this statement is questionable, and Properties 6 to 9 are not fulfilled for the multifocal hyperbola.

Let $\mathcal{F} = \{w_1 F_1, ..., w_N F_N\}$ and $\mathcal{G} = \{\nu_1 G_1, ..., \nu_M G_M\}$ denote the sets of focal points with weights. By omitting the absolute value in (3.2), the multifocal hyperbola expresses the space tessellation. The points with positive values are closer to $\mathcal{G}$; the points with negative values – closer to $\mathcal{F}$; the points with zero values are equidistant to both sets, $\mathcal{F}$ and $\mathcal{G}$.

As can be noted from Definition 17 and 18, the multifocal ellipse defined by the set $\mathcal{J} = \mathcal{F} \cup \mathcal{G}$ has several associated multifocal hyperbolas depending on the elements in sets $\mathcal{F}$ and $\mathcal{G}$.

Property 11 (Number of multifocal hyperbolas for N focal points)**.** *For the set of N focal points, there exist $(2^{N-1}-1)$ multifocal hyperbolas.*

Proof. Each focal point belongs to one of the two groups. So the problem of finding the number of multifocal hyperbolas reduces to the combinatorial task of splitting the set into two non-intersecting subsets. Together, such subsets form the original set. Each of them contains at least one and at most $N-1$ elements. The order of the elements does not matter. The number of k-combinations of an N-element set, for $1 \leq k \leq N-1$, is:

$$\sum_{k=1}^{N-1} \binom{N}{k} = \sum_{k=0}^{N} \binom{N}{k} - \binom{N}{N} - \binom{N}{0} \tag{3.3}$$

According to the properties of binomial coefficients, $\binom{N}{N} = \binom{N}{0} = 1$ and $\sum\limits_{k=0}^{N} \binom{N}{k} = 2^N$ [35]. Next, (3.3) shows the total number of subsets of the N-element set, excluding the situations when one subset is empty or contains all elements. The initial problem searches for the pairs of subsets forming the original set. Selecting k elements is the same as not selecting $N-k$ elements. The symmetry property [35] states that $\binom{N}{k} = \binom{N}{N-k}$. In relation to the initial problem, (3.3) is divided by two. In other words, the number of multifocal hyperbolas for the set of N focal points equals:

$$\frac{\sum\limits_{k=1}^{N-1} \binom{N}{k}}{2} = 2^{N-1} - 1 \tag{3.4}$$

$\square$

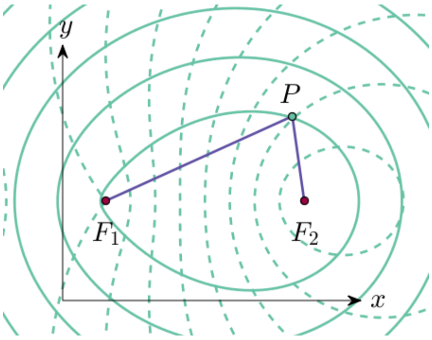

(a) confocal multifocal conics

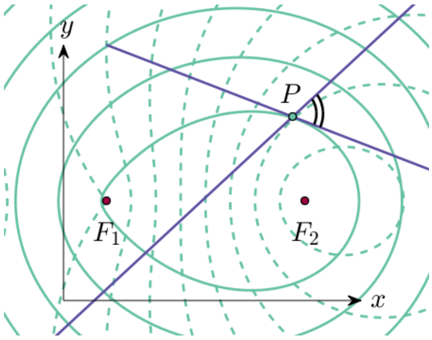

(b) angle between the tangents at P

Figure 3.4: The confocal multifocal ellipses (solid) and hyperbolas (dashed) from the focal points F_1 and F_2 with the weights $w_1 = 0.7$ and $w_2 = 1$ correspondingly. The point P is taken arbitrarily

3.3 Confocal Generalized Conics

Similar to Section 2.3, it is possible to define confocal multifocal ellipses and hyperbolas.

Definition 19 (Confocal multifocal ellipses (or hyperbolas))**.** *If multifocal ellipses (or hyperbolas) share the common focal points and their corresponding weights, then they are called confocal multifocal ellipses (or hyperbolas).*

The original notations of multifocal ellipse (or hyperbola) can be simplified by using only one parameter, c, that defines the distance value: $\mathsf{ME}(c)/\mathsf{MH}(c)$ correspondingly.

Property 12 (Uniqueness of confocal multifocal ellipse and hyperbola passing through a point)**.** *Given any point $P \in \mathbb{R}^2$, there is exactly one level set from a family of confocal multifocal ellipses (or hyperbolas) that passes through it.*

As opposed to conics, Property 5 is not necessarily met in the case of families of confocal multifocal ellipses and hyperbolas. For example, in Figure 3.4b, the angle formed by the tangents to the multifocal ellipse and hyperbola at the point P is not right.

3.4 Generalized Conics with Sharp Corners

From the shape representation perspective, it is important to have a formal description of curves that can be potentially generated. This section focuses on the situation when the level sets contain sharp corners.

Definition 20 (Corner)**.** *A point of a curve, where the left-hand tangent differs from the right-hand tangent, is called corner.*

To simplify the discussion about the properties, it is proposed to normalize the weights. Each of the N weights is divided by the maximum value among them, $max(w_1, w_2, \ldots, w_N)$:

$$\overline{w}_i = \frac{w_i}{\max(w_1, w_2, \ldots, w_N)}, \; i \in [1 \ldots N] \tag{3.5}$$

Hence, the weight values range in the half-closed interval $(0, 1]$.

3.4.1 Multifocal Ellipse with Sharp Corner

Property 13 (Location of a corner in a multifocal ellipse)**.** *If a multifocal ellipse has a corner, it is located only at a focal point. Such a level set is expressed either by a closed curve smooth everywhere except for one corner or by a closed sequence of smooth arcs connected at the corners.*

Proof. As stated in Definition 17, each point $P = (x, y)$ of the multifocal ellipse is mapped to the weighted distance sum to the N-element set of focal points. Let $F_i = (x_i, y_i)$ be the *i-th* focal point, $i \in [1 \ldots N]$. Hence, (3.1) is expressed with regard to (2.1) as:

$$\mathsf{ME}(\overline{w}_1 F_1, ..., \overline{w}_N F_N; c) = \{P \in \mathbb{R}^2 : \sum_{i=1}^{N} \overline{w}_i \sqrt{(x - x_i)^2 + (y - y_i)^2} = c\} \tag{3.6}$$

(3.6) defines a continuous function that is not differentiable at P coinciding with one of the focal points (same reasoning for the non-weighted case is in [131]). Thus, when present, the corner is at the focal point.

$\square$

Consider the example. Figure 3.5a illustrates three level sets generated from the focal points F_1, F_2, and F_3 with the respective weights $\overline{w}_1, \overline{w}_2$, and

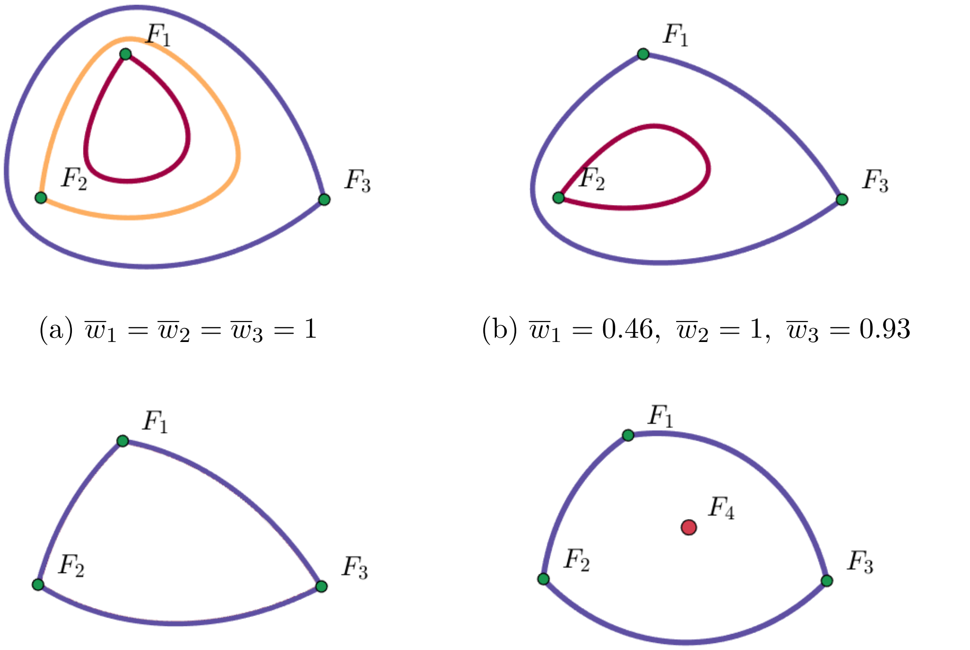

(a) $\overline{w}_1 = \overline{w}_2 = \overline{w}_3 = 1$ (b) $\overline{w}_1 = 0.46,\ \overline{w}_2 = 1,\ \overline{w}_3 = 0.93$

(c) $\overline{w}_1 = 0.608,\ \overline{w}_2 = 0.83,\ \overline{w}_3 = 1$ (d) $\overline{w}_1 = 0.46,\ \overline{w}_2 = 1,\ \overline{w}_3 = 0.75,\ \overline{w}_4 = 1$

Figure 3.5: The multifocal ellipses with the corners at the focal points

$\overline{w}_3$. Each of these level sets is a closed curve with the corner at one of the focal points. When changing the values of weights (Figure 3.5b), the focal points F_1 and F_3 become connected by a closed sequence of arcs and form the level set with two corners at F_1 and F_3. In Figure 3.5c, the focal points F_1, F_2, and F_3 express the corners of the level set containing a closed set of arcs. Similarly, in Figure 3.5d, the focal points F_1, F_2, and F_3 correspond to the corners of the same level set. The focal point F_4 corresponds to the global minimum, thus, its level set contains only the point F_4 and no corner.

Definition 21 (Convex hull)**.** *Given a set of points, the convex hull is its smallest convex subset that encloses all the elements.*

Property 14 (Number of corners in a multifocal ellipse)**.** *A multifocal ellipse from N focal points has up to N corners passing through those focal points.*

Proof. As Property 13 states, the corner is located only at the focal point. Thus, the number of corners cannot exceed the number of focal points. In the case of a single focal point, there exist no level set with a corner. According to Property 6, the multifocal ellipse is convex. Hence, when the focal points form the convex hull, it is possible to generate up to N corners in the same level set. The focal points outside the convex hull are either a global minimum or a part of a different level set. It results in less than N corners in the same level set. □

For instance, let the multifocal ellipse contain three focal points forming the convex hull. Varying the weights generates the level sets containing one (Figure 3.5a), two (Figure 3.5b), and three (Figure 3.5c) corners. In general, the maximum number of corners connected by a single level set equals the number of focal points forming a convex hull (Figure 3.5d). Here, the focal point F_4 is inside the convex hull and is the global minimum.

Property 15 (Uniqueness of weights in a multifocal ellipse passing through all the focal points). *Consider a set of N focal points forming a convex hull. There exists a unique set of normalized weights that corresponds to the multifocal ellipse passing through all these focal points.*

Proof. Property 15 can be proven by induction.

1. $N = 1$: Consider a multifocal ellipse containing a single focal point. According to the normalization strategy, its weight $\overline{w}$ is always 1. Thus, Property 15 holds true.

2. $N = 2$: Consider a pair of focal points with the normalized weights $\overline{w}_1$ and $\overline{w}_2$, where $\overline{w}_1 = 1$. The level set connecting the focal points has the distance value $\mathscr{D}$. The distance between the focal points is l. Then, according to (3.1):

$$\begin{cases} \overline{w}_1 \cdot 0 + \overline{w}_2 \cdot l = \mathscr{D} \\ \overline{w}_1 \cdot l + \overline{w}_2 \cdot 0 = \mathscr{D} \end{cases} \Longleftrightarrow \begin{cases} \overline{w}_2 \cdot l = \mathscr{D} \\ \overline{w}_2 \cdot 0 = \mathscr{D} - l \end{cases} \tag{3.7}$$

The above system of linear equations can be expressed in a matrix form:

$$\begin{pmatrix} l \\ 0 \end{pmatrix} \begin{pmatrix} \overline{w}_2 \end{pmatrix} = \begin{pmatrix} \mathscr{D} \\ \mathscr{D} - l \end{pmatrix} \tag{3.8}$$

The system of linear equations has a unique solution if the matrix rank equals the number of unknown variables. So does the rank of the

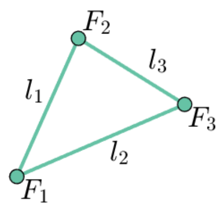

Figure 3.6: The triangle formed by the focal points $F_1,\ F_2$, and F_3

augmented matrix [129]. The rank of the matrix in (3.8) is 1 since the last row contains zero. It suffices to prove that the rank of the augmented matrix also equals 1. By definition, the rank equals the number of rows of the largest submatrix with a non-zero determinant [129]:

$$\left|\begin{array}{c|c} l & \mathscr{D} \\ 0 & \mathscr{D} - l \end{array}\right| \tag{3.9}$$

As can be seen, it is an upper-triangular matrix. Its determinant equals the product of the main diagonal elements [129]. Hence, the system of linear equations does not have any solution if $(\mathscr{D} - l) \cdot l \neq 0$. Since l is greater than 0, the equality to zero is achieved when $(\mathscr{D} - l) = 0$, or $\mathscr{D} = l$. It is a unique solution corresponding to the ellipse that is degenerated into a line segment.

3. $N = 3$: Consider the triplet of focal points with the normalized weights $\overline{w}_1$, $\overline{w}_2$, and $\overline{w}_3$, where $\overline{w}_1 = 1$. Let $l_1,\ l_2$, and l_3 express the pairwise distances between the focal points (Figure 3.6), and $\mathscr{D}$ to be the distance value of the level set connecting them. The corresponding system of linear equations is:

$$\begin{cases} \overline{w}_1 \cdot 0 + \overline{w}_2 \cdot l_1 + \overline{w}_3 \cdot l_2 = \mathscr{D} \\ \overline{w}_1 \cdot l_1 + \overline{w}_2 \cdot 0 + \overline{w}_3 \cdot l_3 = \mathscr{D} \\ \overline{w}_1 \cdot l_2 + \overline{w}_2 \cdot l_3 + \overline{w}_3 \cdot 0 = \mathscr{D} \end{cases} \iff \begin{cases} \overline{w}_2 \cdot l_1 + \overline{w}_3 \cdot l_2 = \mathscr{D} \\ \overline{w}_2 \cdot 0 + \overline{w}_3 \cdot l_3 = \mathscr{D} - l_1 \\ \overline{w}_2 \cdot l_3 + \overline{w}_3 \cdot 0 = \mathscr{D} - l_2 \end{cases} \tag{3.10}$$

(3.10) in the matrix form is expressed as:

$$\begin{pmatrix} l_1 & l_2 \\ 0 & l_3 \\ l_3 & 0 \end{pmatrix} \begin{pmatrix} \overline{w}_2 \\ \overline{w}_3 \end{pmatrix} = \begin{pmatrix} \mathscr{D} \\ \mathscr{D} - l_1 \\ \mathscr{D} - l_2 \end{pmatrix} \tag{3.11}$$

First, the rank of the matrix is computed as follows:

$$\begin{array}{ll} \begin{pmatrix} l_1 & l_2 \\ 0 & l_3 \\ l_3 & 0 \end{pmatrix} & \begin{array}{l} \mid \cdot \frac{1}{l_1} \\ \mid \cdot \frac{1}{l_3} \\ \mid \cdot \frac{1}{l_3} \end{array} \end{array} \tag{3.12a}$$

$$\Rightarrow \begin{array}{ll} \begin{pmatrix} 1 & \frac{l_2}{l_1} \\ 0 & 1 \\ 1 & 0 \end{pmatrix} & \begin{array}{l} -1 \\ \\ + \end{array} \end{array} \tag{3.12b}$$

$$\Rightarrow \begin{array}{ll} \begin{pmatrix} 1 & \frac{l_2}{l_1} \\ 0 & 1 \\ 0 & -\frac{l_2}{l_1} \end{pmatrix} & \begin{array}{l} \\ \\ \mid \cdot -\frac{l_1}{l_2} \end{array} \end{array} \tag{3.12c}$$

$$\Rightarrow \begin{pmatrix} 1 & \frac{l_2}{l_1} \\ 0 & 1 \\ 0 & 1 \end{pmatrix} \tag{3.12d}$$

In (3.12d), the last line can be removed. It leads to the rank being equal to 2. Second, by applying the same operations, the augmented matrix becomes:

$$\left(\begin{array}{cc|c} l_1 & l_2 & \mathscr{D} \\ 0 & l_3 & \mathscr{D} - l_1 \\ l_3 & 0 & \mathscr{D} - l_2 \end{array}\right) \tag{3.13a}$$

$$\Rightarrow \begin{array}{ll} \left(\begin{array}{cc|c} 1 & \frac{l_2}{l_1} & \frac{\mathscr{D}}{l_1} \\ 0 & 1 & \frac{\mathscr{D}-l_1}{l_3} \\ 1 & 0 & \frac{\mathscr{D}-l_2}{l_3} \end{array}\right) & \begin{array}{l} -1 \\ \\ + \end{array} \end{array} \tag{3.13b}$$

$$\Rightarrow \begin{array}{ll} \left(\begin{array}{cc|c} 1 & \frac{l_2}{l_1} & \frac{\mathscr{D}}{l_1} \\ 0 & 1 & \frac{\mathscr{D}-l_1}{l_3} \\ 0 & -\frac{l_2}{l_1} & \frac{\mathscr{D}-l_2}{l_3} - \frac{\mathscr{D}}{l_1} \end{array}\right) & \begin{array}{l} \\ \\ \mid \cdot \frac{l_1}{l_2} \end{array} \end{array} \tag{3.13c}$$

$$\Rightarrow \begin{array}{ll} \left(\begin{array}{cc|c} 1 & \frac{l_2}{l_1} & \frac{\mathscr{D}}{l_1} \\ 0 & 1 & \frac{\mathscr{D}-l_1}{l_3} \\ 0 & -1 & \left(\frac{\mathscr{D}-l_2}{l_3} - \frac{\mathscr{D}}{l_1}\right) \cdot \frac{l_1}{l_2} \end{array}\right) & \begin{array}{l} \\ \\ + \end{array} \end{array} \tag{3.13d}$$

$$\Rightarrow \left(\begin{array}{cc|c} 1 & \frac{l_2}{l_1} & \frac{\mathscr{D}}{l_1} \\ 0 & 1 & \frac{\mathscr{D}-l_1}{l_3} \\ 0 & 0 & \left(\frac{\mathscr{D}-l_2}{l_3} - \frac{\mathscr{D}}{l_1}\right) \cdot \frac{l_1}{l_2} + \frac{\mathscr{D}-l_1}{l_3} \end{array}\right) \tag{3.13e}$$

The determinant equals the product of the diagonal elements [129]. Thus, the unique solution is obtained when:

$$(\frac{\mathscr{D} - l_2}{l_3} - \frac{\mathscr{D}}{l_1}) \cdot \frac{l_1}{l_2} + \frac{\mathscr{D} - l_1}{l_3} = 0 \Longleftrightarrow \mathscr{D} = \frac{2l_1 l_2}{l_1 + l_2 - l_3} \tag{3.14}$$

Otherwise, there is no solution.

4. $N = k + 1$: Assume Property 15 is true for $N = k$. So, the augmented matrix is:

$$\left(\begin{array}{ccccc|c} 1 & l_{12} & l_{13} & \dots & l_{1k} & \mathscr{D}_1 \\ 0 & 1 & l_{23} & \dots & l_{2k} & \mathscr{D}_2 \\ & & & \dots & & \\ 0 & 0 & 0 & \dots & 1 & \mathscr{D}_{k-1} \\ 0 & 0 & 0 & \dots & 0 & \mathscr{D}_k \end{array}\right) \tag{3.15}$$

Here, $\mathscr{D}_i$ is the distance value, and l_{mn} is the variable coefficient after applying the Gaussian elimination [129], $1 \leq i, n \leq k$, $1 \leq m \leq k - 2$. There is the unique level set passing through k focal points, only if $\mathscr{D}_k = 0$, otherwise – no solution.

Adding the extra column and row in (3.15) corresponding to the $(k+1)st$ focal point results in:

$$\left(\begin{array}{cccccc|c} 1 & l_{12} & l_{13} & \dots & l_{1k} & l_{1k+1} & \mathscr{D}_1 \\ 0 & 1 & l_{23} & \dots & l_{2k} & l_{2k+1} & \mathscr{D}_2 \\ & & & \dots & & & \\ 0 & 0 & 0 & \dots & 1 & l_{k-1k+1} & \mathscr{D}_{k-1} \\ 0 & 0 & 0 & \dots & 0 & l_{kk+1} & \mathscr{D}_k \\ l_{k+11} & l_{k+12} & l_{k+13} & \dots & l_{k+1k} & 0 & \mathscr{D}_{k+1} \end{array}\right) \begin{array}{l} \\ \\ \\ \\ | \cdot \frac{1}{l_{kk+1}} \\ \\ \end{array} \tag{3.16a}$$

$$\Rightarrow \left(\begin{array}{cccccc|c} 1 & l_{12} & l_{13} & \dots & l_{1k} & l_{1k+1} & \mathscr{D}_1 \\ 0 & 1 & l_{23} & \dots & l_{2k} & l_{2k+1} & \mathscr{D}_2 \\ & & & \dots & & & \\ 0 & 0 & 0 & \dots & 1 & l_{k-1k+1} & \mathscr{D}_{k-1} \\ 0 & 0 & 0 & \dots & 0 & 1 & \frac{\mathscr{D}_k}{l_{kk+1}} \\ l_{k+11} & l_{k+12} & l_{k+13} & \dots & l_{k+1k} & 0 & \mathscr{D}_{k+1} \end{array}\right) \tag{3.16b}$$

As observed in (3.16b), the variable coefficients in the last row can be eliminated by consecutive multiplication-subtraction of the above k

rows:

$$\left(\begin{array}{cccccc|c} 1 & l_{12} & l_{13} & \dots & l_{1k} & l_{1k+1} & \mathscr{D}_1 \\ 0 & 1 & l_{23} & \dots & l_{2k} & l_{2k+1} & \mathscr{D}_2 \\ & & & \dots & & & \\ 0 & 0 & 0 & \dots & 1 & l_{k-1k+1} & \mathscr{D}_{k-1} \\ 0 & 0 & 0 & \dots & 0 & 1 & \frac{\mathscr{D}_k}{l_{kk+1}} \\ 0 & 0 & 0 & \dots & 0 & 0 & \mathscr{D}'_{k+1} \end{array}\right) \tag{3.17}$$

If $\mathscr{D}'_{k+1} = 0$, there is only one combination of the normalized weights $\{1, \overline{w}_2, \dots, \overline{w}_{k+1}\}$, such that the multifocal ellipse connects all $(k+1)$ focal points. Otherwise, such a level set does not exist.

□

3.4.2 Multifocal Hyperbola with Sharp Corner

As opposed to multifocal ellipses, which generate convex level sets, multifocal hyperbolas enable getting concave corners. Let $\mathcal{F} = \{w_1F_1, w_2F_2\}$ and $\mathcal{G} = \{\nu_1G_1\}$ be the sets of focal points producing the confocal multifocal hyperbolas (Figure 3.7). One of the level sets, $\mathsf{MH}(c_{G_1})$, contains a concave corner at G_1. Another level set, $\mathsf{MH}(c_{F_1})$, passes through F_1 and has the convex corner at that focal point. Eventually, the level set corresponding to F_2, $\mathsf{MH}(c_{F_2})$, is the focal point itself.

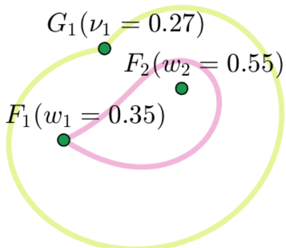

Figure 3.7: The confocal multifocal hyperbolas with the corners at F_1 and G_1

Property 16 (Multifocal hyperbola containing a focal point and a curve)**.** *A multifocal hyperbola can contain a focal point and a curve that are not connected.*

This statement is exemplified in Figure 3.8. Consider the two sets of focal points: $\mathcal{F} = \{w_1F_1, w_2F_2, w_3F_3\}$ and $\mathcal{G} = \{\nu_1G_1\}$. Each member of the family

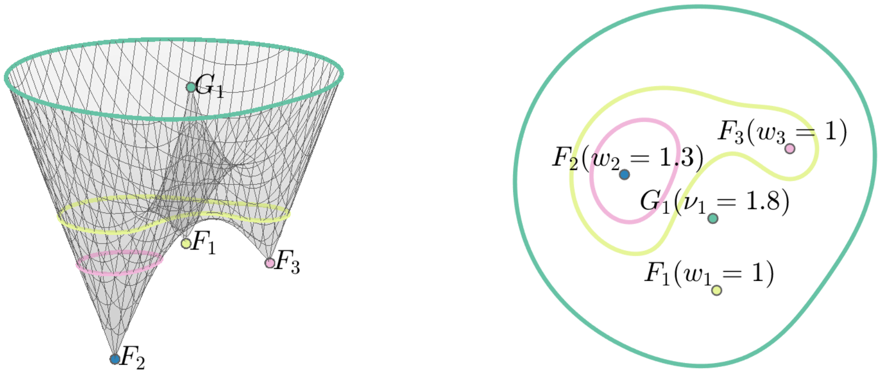

(a) confocal multifocal hyperbolas in 3D (b) level sets (top view)

Figure 3.8: The confocal multifocal hyperbolas passing through the focal points

of confocal multifocal hyperbolas is denoted as $\mathsf{MH}(w_1F_1, w_2F_2, w_3F_3|\nu_1G_1; c)$. In the presence of a negatively weighted G_1, multiple level sets contain two disconnected elements: a focal point and a curve. Let the level set passing through F_1 be denoted as $\mathsf{MH}(c_{F_1})$, through F_2 – $\mathsf{MH}(c_{F_2})$, through F_3 – $\mathsf{MH}(c_{F_3})$, and, eventually, through G_1 – $\mathsf{MH}(c_{G_1})$. The 3D representation of the level sets has two axes that define the spatial location of the points and one axis – their distance value (Figure 3.8a). Figure 3.8b shows the top view on the level sets passing through the focal points. In this scenario, the positively weighted focal points (F_1, F_2, and F_3) are the local/global minima, whereas G_1 is the local maximum. As can be observed, the level set passing through the global minimum F_2 contains only the focal point itself. The distance value of the local minimum F_3 is also present in the region surrounding F_2. Hence, the level set $\mathsf{MH}(c_{F_3})$ has two disconnected components: the point F_3 and the curve around F_2. The level set passing through F_1 contains also the curve surrounding F_2 and F_3. Finally, the level set $\mathsf{MH}(c_{G_1})$ contains G_1 and the curve surrounding all the positively weighted focal points.

Property 17 (Multifocal hyperbola does not pass through all focal points)**.** *There is no multifocal hyperbola connecting all positively and negatively weighted focal points.*

Property 17 stems from the fact that a multifocal hyperbola maps each point in space to either of the two multifocal ellipses. As a result, there can be no level set connecting positively and negatively weighted points simultaneously. In this case, one of the level sets would cross the zero-curve – the level set containing the points equidistant to both multifocal ellipses. Eventually, the point(s) at the intersection would be associated with two distance values, which is not possible because of Property 12.

3.5 Changing Angle at a Corner

The complexity of generalized conics increases with a number of focal points. For example, the degree of a polynomial defining the multifocal ellipse with N focal points equals 2^N if N is odd, and $2^N - \binom{N}{N/2}$ if N is even [131]. The existing works derive the parameters of generalized conics in the special cases, such as egglipse [164]. This section discusses the multifocal ellipses and hyperbolas that are generated from a pair of weighted focal points, namely an egg-shape and a hyperbolic shape (Figure 3.9). In particular, it establishes the formal correspondence between the angles and weights at corners.

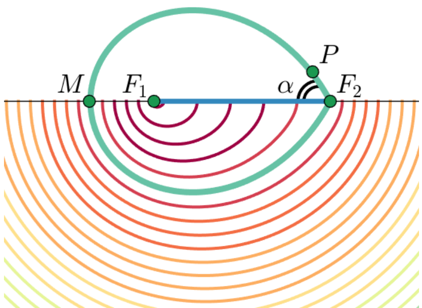

(a) egg-shape having the sharp corner at F_2, $\alpha = 62°$, $\mu = 0.47$

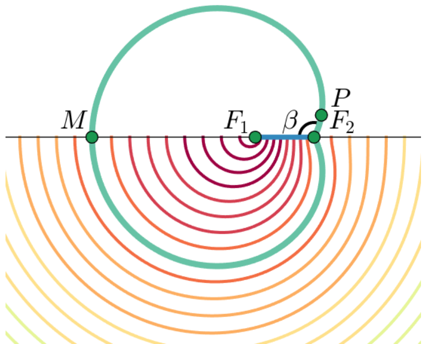

(b) hyperbolic shape having the sharp corner at F_2, $\beta = 118°$, $\mu = 0.47$

Figure 3.9: The egg-shape and the hyperbolic shape with the focal points at F_1 and F_2. The lower half shows the level sets, and the upper half shows the curve parameters

3.5.1 Egg-Shape

According to (3.1), the multifocal ellipse with the pair of focal points F_1 and F_2 and the respective weights w_1 and w_2 can be defined as:

$$\mathsf{ME}(w_1F_1, w_2F_2; c) = \{P \in \mathbb{R}^2 : w_1\mathsf{d}_2(P, F_1) + w_2\mathsf{d}_2(P, F_2) = c\} \qquad (3.18)$$

After normalization (3.5), there remains a single weight $0 < \mu = \frac{min(w_1,w_2)}{max(w_1,w_2)} \leq 1$. Assume that the smaller weight corresponds to F_2, then:

$$\mathsf{ME}(F_1, \mu F_2; c) = \{P \in \mathbb{R}^2 : \mathsf{d}_2(P, F_1) + \mu\mathsf{d}_2(P, F_2) = c\} \qquad (3.19)$$

Besides the special case, when the multifocal ellipses are ellipses ($\mu = 1$), the level sets resemble an egg-shape with various sharpness.

Figure 3.9a exemplifies the level sets generated from the pair of focal points F_1 and F_2, where the latter has the weight $\mu = 0.47$. The level set with the corner passes through the focal point F_2. The angle at the corner equals $2\alpha = 124°$.

Theorem 1 (Global minimum for an egg-shape)**.** *(3.19) reaches the global minimum at the focal point with the largest associated weight.*

Proof. Assume the egg-shape, $\mathsf{ME}(F_1, \mu F_2; c)$, where $0 < \mu < 1$. To prove the theorem, estimate the distance value of an arbitrary point P depending on its location (Figure 3.10):

1. P is located to the left of F_1: $\mathsf{d}_2(P, F_1) + \mu\mathsf{d}_2(P, F_2)$

2. P is located at F_1: $\mu\mathsf{d}_2(F_1, F_2)$

3. P is located between F_1 and F_2: $\mathsf{d}_2(P, F_1) + \mu\mathsf{d}_2(P, F_2)$

4. P is located at F_2: $\mathsf{d}_2(F_1, F_2)$

5. P is located to the right of F_2: $\mathsf{d}_2(P, F_1) + \mu\mathsf{d}_2(P, F_2)$

Proof by contradiction. Let the global minimum be located not at F_1, but at some point P to the left of F_1 (case 1). The distance value at P must be less than at F_1:

$$\mathsf{d}_2(P, F_1) + \mu\mathsf{d}_2(P, F_2) < \mu\mathsf{d}_2(F_1, F_2) \qquad (3.20)$$

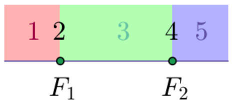

Figure 3.10: The regions, where an arbitrary point P is located relatively to F_1 and F_2

Since P is located to the left of F_1, the angle $\widehat{F_2F_1P}$ ranges from 90° to 180°. By the triangle property [146], the longest side is opposite to the largest angle, thus, $\mu\mathsf{d}_2(P, F_2) > \mu\mathsf{d}_2(F_1, F_2)$. When applied to (3.20), $\mathsf{d}_2(P, F_1)$ becomes negative which is a contradiction. Similarly, it is possible to show that the global minimum cannot be located to the right of F_2 (case 5).

Let P be in the region bounded by the half-planes passing through F_1 and F_2 (case 3). If P belongs to the line segment $\overline{F_1F_2}$, then $\mathsf{d}_2(P, F_1) + \mu\mathsf{d}_2(P, F_2) > \mu\mathsf{d}_2(F_1, F_2)$ since $\mu < 1$. Otherwise, P and the focal points form a triangle. According to the triangle inequality [38], $\mathsf{d}_2(P, F_1) + \mathsf{d}_2(P, F_2) > \mathsf{d}_2(F_1, F_2)$. Hence, $\mathsf{d}_2(P, F_1) + \mu\mathsf{d}_2(P, F_2) > \mu\mathsf{d}_2(F_1, F_2)$.

Finally, P cannot be located at F_2 (case 4) since $\mathsf{d}_2(F_1, F_2) > \mu\mathsf{d}_2(F_1, F_2)$.

As can be observed, the minimum value among all the regions is achieved when the point P coincides with the focal point F_1 (case 2).

□

Theorem 2 (Angle at a corner of an egg-shape). *Consider the egg-shape $\mathsf{ME}(F_1, \mu F_2; c)$ with the sharp corner. The normalized weight (μ) of the focal point F_2 equals approximately the cosine of half of the angle at the corner (α).*

Proof. Let $\mathsf{ME}(F_1, \mu F_2; c)$ be the egg-shape that has the sharp corner at F_2 (Figure 3.9a). Here, F_1 and F_2 are the focal points, P is infinitely close to F_2 and is a part of the corner. Assume the following notations: $\mathsf{d}_2(F_1, P) = n$, $\mathsf{d}_2(F_2, P) = m$, $\mathsf{d}_2(F_1, F_2) = 2f$, and $\widehat{F_1F_2P} = \alpha$. According to Definition 17, all points of the egg-shape are mapped to the same distance value. It equals the length of the line segment $\overline{F_1F_2}$:

$$\mathsf{d}_2(F_1, F_2) + \mu\mathsf{d}_2(F_2, F_2) = \mathsf{d}_2(F_1, F_2) = 2f \tag{3.21}$$

Consider now substituting P in (3.21):

$$\mathsf{d}_2(F_1, P) + \mu\mathsf{d}_2(F_2, P) = 2f \tag{3.22}$$
$$n + \mu m = 2f \tag{3.23}$$
$$\implies n = 2f - \mu m \tag{3.24}$$

By considering the triangle $\triangle F_1PF_2$ and the law of cosines [149], it is possible to derive the alternative estimate of n:

$$m^2 + 4f^2 - 4mf\cos\alpha = n^2 \tag{3.25}$$

Substitution of n estimate from (3.24) in (3.25) results in:

$$m^2 + 4f^2 - 4mf\cos\alpha = 4f^2 - 4\mu mf + m^2\mu^2 \tag{3.26}$$

$$\implies m = \frac{4f(\mu - \cos\alpha)}{\mu^2 - 1} \tag{3.27}$$

As discussed, the point P is infinitely close to F_2 in continuous space. So, in discrete space, the length of m converges to zero. It leads to further simplification of (3.27):

$$m = \frac{4f(\mu - \cos\alpha)}{\mu^2 - 1} = 0 \tag{3.28}$$

$$\implies \mu = \cos\alpha \tag{3.29}$$

(3.29) establishes the direct dependency between the angle at the corner of the egg-shape and the weight of the corresponding focal point. □

Theorem 2 enables rewriting (3.19) by considering the angle 2α at the corner:

$$\mathsf{d}_2(F_1, P) + \cos\alpha \cdot \mathsf{d}_2(F_2, P) = \mathsf{d}_2(F_1, F_2) \tag{3.30}$$

On one side, (3.30) has an important implication for shape representation: compared to an ellipse, an egg-shape has one additional parameter which explicitly defines the angle at its corner. On the other side, it is possible to derive the parameters of the egg-shape with the corner if the curve satisfies (3.30). Refer to Figure 3.9a. The symmetry axis passes through F_2 and bisects the corner creating two congruent angles α. The point M is the intersection point of the symmetry axis and the egg-shape. This information is sufficient to derive the distance between the focal points by substituting M in (3.30):

$$\mathsf{d}_2(F_1, F_2) = \frac{\mathsf{d}_2(M, F_2) \cdot (1 + \cos\alpha)}{2} \tag{3.31}$$

Finally, F_1 can be found as the point on the symmetry axis that is inside the egg-shape at the distance $\mathsf{d}_2(F_1, F_2)$ from F_2.

3.5.2 Hyperbolic Shape

Analogically to the egg-shape, it is possible to formalize the correspondence between the angle and the weight at a corner of a hyperbolic shape. According to (3.2), the weighted multifocal hyperbola with two focal points, F_1 and F_2, and their respective weights, w_1 and w_2, can be defined as follows:

$$\mathsf{MH}(w_1F_1|w_2F_2;c) = \{P \in \mathbb{R}^2 : |w_1\mathsf{d}_2(P,F_1) - w_2\mathsf{d}_2(P,F_2)| = c\} \tag{3.32}$$

Using the normalization strategy (3.5) enables keeping only the single weight parameter $0 < \mu = \frac{min(w_1,w_2)}{max(w_1,w_2)} \leq 1$. In particular, when $\mu = 1$, the level sets are hyperbolas. Assume the smaller weight corresponds to the point F_2 (Figure 3.9b), then (3.32) becomes:

$$\mathsf{MH}(F_1|\mu F_2;c) = \{P \in \mathbb{R}^2 : |\mathsf{d}_2(P,F_1) - \mu\mathsf{d}_2(P,F_2)| = c\} \tag{3.33}$$

Theorem 3 (Angle at a corner of a hyperbolic shape)**.** *Consider the hyperbolic shape* $\mathsf{MH}(F_1|\mu F_2;c)$ *with the corner. The normalized weight (μ) of the focal point F_2 equals approximately minus the cosine of half of the angle at the corner (β).*

Proof. Let $\mathsf{MH}(F_1|\mu F_2;c)$ be the hyperbolic shape with the sharp corner at F_2 (Figure 3.9b). The point P is infinitely close to F_2 and belongs to the corner. Consider the following notations: $\mathsf{d}_2(F_1,P) = n$, $\mathsf{d}_2(F_2,P) = m$, $\mathsf{d}_2(F_1,F_2) = 2f$, and $\widehat{F_1F_2P} = \beta$. According to (3.33), the distance value at F_2 equals:

$$|\mathsf{d}_2(F_1,F_2) - \mu\mathsf{d}_2(F_2,F_2)| = \mathsf{d}_2(F_1,F_2) = 2f \tag{3.34}$$

Analogically to the proof for an egg-shape, the estimate of n after substituting the point P in (3.34) is:

$$n = 2f + \mu m \tag{3.35}$$

Similarly, consider the law of cosines [149] for the triangle $\triangle F_1PF_2$ and substitute n by the estimate from (3.35). It leads to the following relation:

$$m = \frac{-4f(\mu + \cos\beta)}{\mu^2 - 1} \tag{3.36}$$

Since m is infinitely small, it is possible to assign it to zero in discrete space: $\mu = -\cos\beta$. As a result, the angle at the corner of the hyperbolic shape has the direct dependency on the weight of the corresponding focal point. $\square$

One implication of Theorem 3 is the possibility to rewrite (3.33) more intuitively. If the angle at the concave corner equals 2β, then the level set passing through the corresponding focal point F_2 satisfies:

$$\mathsf{d}_2(F_1, P) + \cos\beta \cdot \mathsf{d}_2(F_2, P) = \mathsf{d}_2(F_1, F_2) \tag{3.37}$$

Another implication is connected to shape representation domain. Compared to an ellipse, a hyperbolic shape generated from the pair of focal points requires only one additional parameter – the angle at the corner. Hence, given a curve that satisfies (3.37), it is possible to derive its parameters. Consider the level set illustrated in Figure 3.9b. The symmetry axis intersects the hyperbolic shape at F_2 and M and bisects the corner creating a pair of congruent angles β. Then, the distance between the focal points according to (3.37) equals:

$$\mathsf{d}_2(F_1, F_2) = \frac{\mathsf{d}_2(M, F_2) \cdot (1 + \cos\beta)}{2} \tag{3.38}$$

Consequently, the remaining focal point F_1 is at the distance $\mathsf{d}_2(F_1, F_2)$ when moving along the symmetry axis from F_2 to M. Apparently, there is a similarity between (3.31) and (3.38). Although, the convexity of the egg-shape implies a positive $\cos\alpha$, whereas the concavity in the hyperbolic shape requires a negative $\cos\beta$.

3.6 Summary

A number of focal points highly influences the complexity of generalized conics. It implies the idea of focusing on particular scenarios prior to creating a general picture. This chapter limits the research scope to multifocal ellipses and hyperbolas with corners and contributes to the state of the art by analysing their properties from shape representation perspective. For instance, the established correspondence between the angle at the corner of an egg-shape (or a hyperbolic shape) and the weight of the focal point enables using that primitives instead of an ellipse for representing shapes with convex or concave sharp corners. The correspondence between the weights of more than two focal points and the angles at the corners is the question for future research. The uniqueness of the normalized weights passing through all the focal points of the multifocal ellipse is a potential key to tackle that problem.

CHAPTER 4

Distance Fields based on the Properties of Generalized Conics

This chapter is based on the following publications:

Aysylu Gabdulkhakova, Walter G. Kropatsch:
Confocal Ellipse-based Distance and Confocal Elliptical Field for polygonal shapes. In Proceedings of the International Conference on Pattern Recognition, pages 3025–3030, 2018 [66]

Aysylu Gabdulkhakova, Maximilian Langer, Bernhard W. Langer, Walter G. Kropatsch:
Line Voronoi Diagrams Using Elliptical Distances. In Proceedings of the Joint IAPR International Workshop on Structural, Syntactic, and Statistical Pattern Recognition, pages 258–267, 2018 [69]

Aysylu Gabdulkhakova, Walter G. Kropatsch:
Generalized conics: properties and applications. In Proceedings of the International Conference on Pattern Recognition, pages 10728–10735, 2020 [67]

A distance field is an implicit space representation. It specifies for each point its proximity to a set of objects with regard to a distance function [27]. The existing approaches measure the distance between a pair of points. The object or its boundary is decomposed into a set of points, and the proximity is the distance to the closest element from this set.

The present work provides the alternative views to this problem. First, the Confocal-Ellipse-based Distance (CED) measures the distance between a pair of confocal ellipses. Assume, one of the ellipses degenerates into a line segment bounded by the focal points. The second ellipse is expressed by the set of points that it passes through. These assumptions enable computing the distance between the point and the line segment by defining the latter only by its endpoints. A part of this chapter analyzes the geometrical properties of the distance field generated from CED – the Confocal Elliptic Field (CEF).

Second, by referring to the generalized conics, the proximity to the set of objects can be measured as the distance sum to all objects in this set. This idea is reflected in the Confocal Multifocal Elliptic Field (CMEF). The difference between two CMEFs produces the Confocal Multifocal Hyperbolic Field (CMHF) expressing the proximity to the pair of object sets.

4.1 Distance from a Point to a Line Segment

This section presents the new metric for computing the distance between a point and a line segment based on the properties of confocal ellipses. The comparison with the state-of-the-art approach, the Hausdorff Distance (HD), regards representation of level sets.

4.1.1 Hausdorff Distance (HD)

A classical way to measure the distance between a point and a line segment is to use the Hausdorff Distance (HD).

Definition 22 (Hausdorff Distance)**.** *The Hausdorff Distance (HD) between an arbitrary point $P \in \mathbb{R}^2$ and a line segment l equals the shortest distance between P and a point $L \in l$ with regard to a selected metric (for example, Euclidean):*

$$\mathsf{d}_{HD}(P, l) = \inf\{\mathsf{d}_2(P, L) \mid L \in l\} \tag{4.1}$$

Figure 4.1 illustrates the HD level sets. Let the line segment l contain N points, $l = \{L_1, \ldots, L_N\}$. The orange and blue curves are the level sets with the distance values r_1 and r_2 respectively. The intuition of the level set is a fusion of the circles with the given radii (r_1 or r_2) and the centers at $L_i,\ i \in [1 \ldots N]$. Figure 4.1 exemplifies two circles with the centers at L_1 and

L_N and radii r_1 and r_2. The dashed curves show the circle arcs that are not part of the HD level sets.

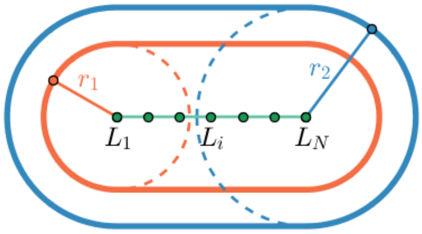

Figure 4.1: The HD level sets (orange and blue solid curves)

4.1.2 Confocal-Ellipse-based Distance (CED)

According to Property 4 of confocal ellipses, it is ensured that each point on a 2D plane has a single distance value associated with it. This fact enables introducing a metric.

Definition 23 (Confocal-Ellipse-based Distance)**.** *Let the distance between two confocal ellipses, $\mathsf{E}(a_1)$ and $\mathsf{E}(a_2)$, be called the Confocal-Ellipse-based Distance (CED), $\mathsf{d}_{CED} : \mathbb{R}^2 \times \mathbb{R}^2 \to \mathbb{R}$. It is an absolute difference between the lengths of major axes, $2a_1$ and $2a_2$, of these ellipses:*

$$\mathsf{d}_{CED}(\mathsf{E}(a_1), \mathsf{E}(a_2)) = 2|a_1 - a_2| \tag{4.2}$$

Figure 4.2 shows the corresponding CED level sets (solid orange and blue curves) that are confocal ellipses. The dashed line segments demonstrate the distances from an arbitrary point of a level set to the focal points F_1 and F_2. In relation to (4.2), the length sum of orange and blue dashed line segments equals $2a_1$ and $2a_2$ respectively.

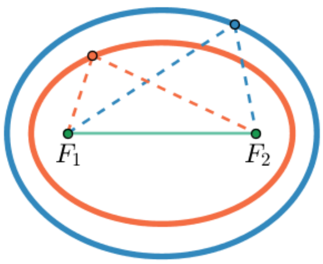

Figure 4.2: The CED level sets (orange and blue solid curves)

Theorem 4 (CED is a metric)**.** *CED is a metric.*

Proof. Consider $\mathsf{E}(a_1)$ and $\mathsf{E}(a_2)$ to be confocal ellipses. By Definition 7, the proposed distance must satisfy the metric conditions:

1. non-negativity,
   $\mathsf{d}_{CED}(\mathsf{E}(a_1), \mathsf{E}(a_2)) \geq 0$

   By definition, the absolute value is non-negative. Thus, $2|a_1 - a_2| \geq 0$.

2. identity of indiscernibles,
   $\mathsf{d}_{CED}(\mathsf{E}(a_1), \mathsf{E}(a_2)) = 0 \Leftrightarrow \mathsf{E}(a_1) = \mathsf{E}(a_2)$

   (a) Let $\mathsf{d}_{CED}(\mathsf{E}(a_1), \mathsf{E}(a_2)) = 0$.
   Then: $2|a_1 - a_2| = 0 \implies a_1 = a_2 \implies \mathsf{E}(a_1) = \mathsf{E}(a_2)$.

   (b) Let $\mathsf{E}(a_1) = \mathsf{E}(a_2)$.
   Then: $a_1 = a_2 \implies 2|a_1 - a_2| = 0 \implies \mathsf{d}_{CED}(\mathsf{E}(a_1), \mathsf{E}(a_2)) = 0$.

3. symmetry,
   $\mathsf{d}_{CED}(\mathsf{E}(a_1), \mathsf{E}(a_2)) = \mathsf{d}_{CED}(\mathsf{E}(a_2), \mathsf{E}(a_1))$

   By definition,
   $\mathsf{d}_{CED}(\mathsf{E}(a_1), \mathsf{E}(a_2)) = 2|a_1 - a_2| = 2|a_2 - a_1| = \mathsf{d}_{CED}(\mathsf{E}(a_2), \mathsf{E}(a_1))$.

4. triangle inequality,
   $\mathsf{d}_{CED}(\mathsf{E}(a_1), \mathsf{E}(a_2)) \leq \mathsf{d}_{CED}(\mathsf{E}(a_1), \mathsf{E}(a_3)) + \mathsf{d}_{CED}(\mathsf{E}(a_2), \mathsf{E}(a_3))$

   $2|a_1 - a_2| \leq 2|a_1 - a_3| + 2|a_2 - a_3|$

   Substitution of the absolute values by respecting the value correspondence leads to valid inequalities. Hence, this property is met.

□

According to (2.6), an ellipse degenerates into a line segment when the major axis length equals the focal distance. In (4.2), let one of the confocal ellipses, for example, $\mathsf{E}(a_2)$, be the line segment $\overline{F_1F_2}$ connecting its focal points F_1 and F_2. Hence, $a_2 = f$. Then, for each point on $\mathsf{E}(a_1)$, the distance to any point on $\mathsf{E}(a_2)$ with regard to CED equals:

$$\mathsf{d}_{CED}(\mathsf{E}(a_1), \mathsf{E}(f)) = 2|a_1 - f| \tag{4.3}$$

(4.3) results in zero values of $\mathsf{d}_{CED}(\mathsf{E}(a_1), \mathsf{E}(f))$ for all points belonging to $\overline{F_1F_2}$. So, CED is a valid metric for measuring the distance from the line segment $\overline{F_1F_2}$ to any point in space. In this case, the point defines the confocal ellipse (with semi-major axis length of a_1) that goes through it.

Definition 24 (Distance from a point to a line segment in terms of CED)**.** *The distance from point $P \in \mathbb{R}^2$ to line segment $l = \overline{F_1F_2}$ in terms of CED is:*

$$\mathsf{d}_{CED}(P, l) = \mathsf{d}_{CED}(\mathsf{E}(a_0), \mathsf{E}(a_P)) \tag{4.4}$$

In (4.4), $\mathsf{E}(a_P)$ is a unique ellipse passing through P with the focal points F_1 and F_2. The length of its semi-major axis is a_P. $\mathsf{E}(a_0)$ is the ellipse degenerated into the line segment with the focal points F_1 and F_2, thus, $a_0 = \frac{\mathsf{d}_2(F_1,F_2)}{2}$. In other words, a_0 is half of the length of the line segment connecting the focal points F_1 and F_2.

Alternatively, $\mathsf{d}_{CED}(P, l)$ can be defined by the sum and difference of the Euclidean distances with regard to (2.6) as follows:

$$\mathsf{d}_{CED}(P, l) = \mathsf{d}_2(P, F_1) + \mathsf{d}_2(P, F_2) - \mathsf{d}_2(F_1, F_2) \tag{4.5}$$

Subtraction of a_0 normalizes the distance function by mitigating its dependence on the line segment length.

4.1.3 Comparison between HD and CED

As can be seen in Figures 4.1 and 4.2, for the line segment, CED and HD produce different level sets: confocal ellipses and a convex envelope of circles, respectively. To compute a CED distance field it suffices to have two parameters – locations of the focal points. In contrast, HD takes into account each point of the line segment. If there is HD distance field containing confocal ellipses, then computing the representation could be optimized by using CED. Let the HD distance values be propagated from the ellipse boundary towards the interior. The resultant level sets are compared to the family of confocal ellipses generated from the focal points of that ellipse.

In Figure 4.3a, the bold green ellipse, $\mathsf{E}(F_1, F_2; a)$, has the foci at F_1 and F_2. In the corresponding family of confocal ellipses (solid green), the lengths of major and minor axes are changing while keeping the distance between the focal points constant. According to (2.7) and (2.8), it leads to various eccentricity values of confocal ellipses. The HD level sets propagated from $\mathsf{E}(F_1, F_2; a)$ are elliptic (dashed red in Figure 4.3a). These level sets have a constant offset with respect to each other, which leads to the constant

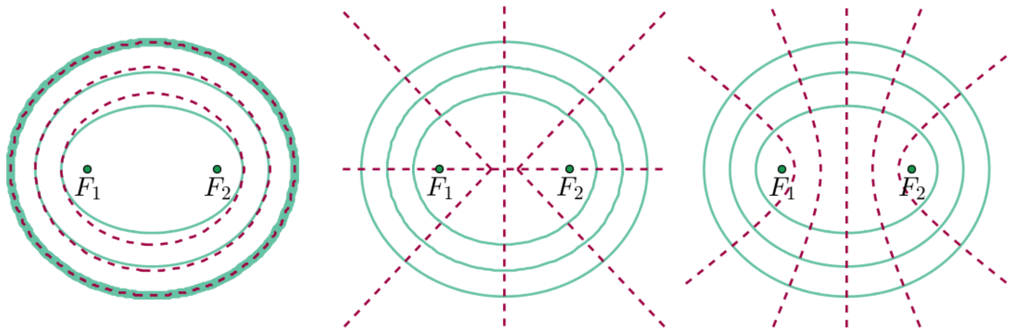

(a) DT_2 and confocal ellipses

(b) normals to DT_2 level sets

(c) normals to confocal ellipses

Figure 4.3: DT_2 of the ellipse and the corresponding confocal ellipses

eccentricity and a unique pair of focal points for each level set. The smallest distance value increment follows the direction of the normal to the level set at that point [73]. Following the normals of the consecutive confocal ellipses forms the hyperbola branches (dashed red in Figure 4.3c). The normals to the HD level sets form the rays (dashed red in Figure 4.3b). So, the HD representation of the ellipse cannot be simplified by using CED .

Both HD and CED are extendable to higher dimensions. In 3D, the representation of the distance values is obtained by rotation about the line segment $\overline{F_1F_2}$. For HD, the resultant 3D volume comprises two half-spheres and a cylinder. For CED, it is an ellipsoid of revolution (Figure 4.4), namely a prolate spheroid, with the median and minor axes having an equal length.

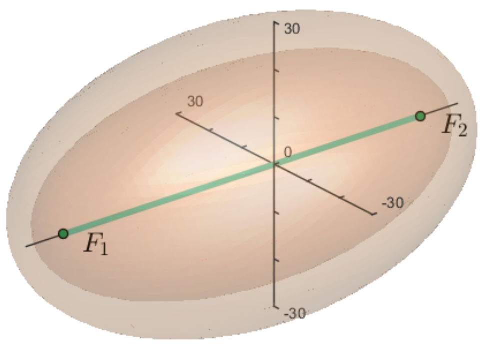

Figure 4.4: The example of CED level sets in 3D

The latter is proven by considering the cross sections passing through the line segment $\overline{F_1F_2}$. Due to the constant distance sum to two focal points, in each plane, the generated curve is an ellipse with the same parameters a and b.

4.2 Confocal Elliptic Field (CEF)

A distance field associates each point in space with its distance to a closest element from a set of objects [27]. Depending on a metric the level sets vary. When applying the Euclidean metric, the distance field is referred to as the Euclidean Distance Field (DF_2). In the simplest case, the set of objects contains a point, and the level sets are concentric circles with the center at that point. Thanks to (2.6) and (2.12), a combination of DF_2s produces the distance fields containing confocal conics.

Definition 25 (Confocal ellipses from two points)**.** *Let $\mathcal{F} = \{F_1, F_2\}$ be the set of two points. The sum of DF_2s generated from F_1 and F_2 creates a distance field containing confocal ellipses (Figure 4.5).*

Figure 4.5: The distance field containing confocal ellipses

Definition 26 (Confocal hyperbolas from two points)**.** *Let $\mathcal{F} = \{F_1, F_2\}$ be the set of two points. The difference of DF_2s generated from F_1 and F_2 produces the distance field containing confocal hyperbolas (Figure 4.6).*

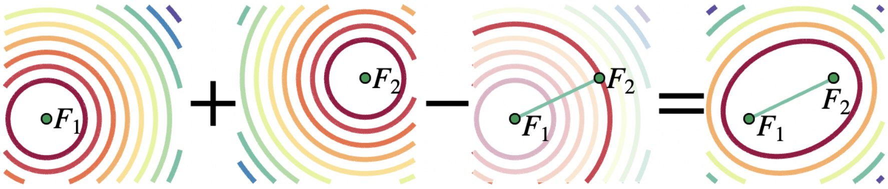

Figure 4.7: The distance field of the line segment with d_{CED} as a metric

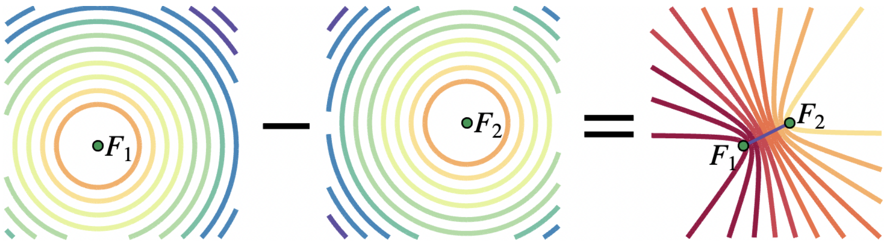

Figure 4.6: The distance field containing confocal hyperbolas

Compared to Definition 25, d_{CED} from (4.5) additionally subtracts the line segment length which, in fact, is present in the distance field.

Property 18 (Distance value that equals the line segment length)**.** *The distance value of F_2 in DF$_2$ of F_1 equals the length of the line segment $\overline{F_1F_2}$. And vice versa.*

Definition 27 (Distance field of a line segment under CED)**.** *The distance field of $\overline{F_1F_2}$ under d_{CED} equals subtraction of the line segment length from the sum of DF$_2$s generated from F_1 and F_2 (Figure 4.7). The level sets are confocal ellipses.*

In the special case, when the line segment degenerates into a point (for instance, the endpoints of $\overline{F_1F_2}$ are identical), the distance field of confocal ellipses degenerates into the doubled DF$_2$ of this point.

Subtraction of $\mathsf{d}_2(F_1, F_2)$ has a normalization effect – the distance values at the points belonging to $\overline{F_1F_2}$ are zero. Therefore, it is possible to combine multiple distance fields corresponding to various line segments. Applying the minimum operation to a collection of such distance fields presents the way to find the distance from a point to a set of line segments. It implies the notion of *Confocal Elliptic Field (CEF)*.

Definition 28 (Confocal Elliptic Field)**.** *Consider a set $\mathcal{F}$ containing N line segments and points defined as line segments with coinciding endpoints. Each point in the Confocal Elliptic Field (CEF) is associated with the distance value to the closest element in $\mathcal{F}$ with respect to CED (refer to (4.5)):*

$$CEF = \{P \in \mathbb{R}^2 : \inf\{\mathsf{d}_{CED}(P, l_i) \mid l_i \in \mathcal{F},\ i \in [1, ..., N]\}\} \tag{4.6}$$

In other words, in CEF, there is a mapping between each point $P \in \mathbb{R}^2$ and the smallest value from the set of distance fields. CEF tessellates the space according to proximity of points to the set of line segments and points.

Definition 29 (Receptive field)**.** *Consider a set $\mathcal{F}$ containing N line segments and points defined as line segments with coinciding endpoints. CEF is a distance field generated from $\mathcal{F}$. A set of points that have the distance to a line segment $l_i \in \mathcal{F}$ smaller or equal than the distance to any other $l_j \in \mathcal{F}$, $i,\ j \in [1, \ldots, N], j \neq i$ defines the receptive field R_i:*

$$\underset{i \in [1,...,N]}{R_i} = \{P \in \mathbb{R}^2 : CEF(P) - \mathsf{d}_{CED}(P, l_i) = 0 \mid l_i \in \mathcal{F}\} \tag{4.7}$$

4.2.1 Separating Curve

A set of points in CEF has an identical value in several receptive fields. Such points are equidistant from at least two elements in the set $\mathcal{F}$.

Definition 30 (Separating curve)**.** *A separating curve, denoted as S_{ij}, visually divides the receptive fields R_i and R_j associated with various objects. It is a zero level set when taking the difference between these receptive fields:*

$$\underset{\substack{i,j \in [1,...,N];\\ i \neq j}}{S_{ij}} = \{P \in \mathbb{R}^2 : P \in (R_i \cap R_j = 0)\} \tag{4.8}$$

The geometric nature of the separating curve depends on the mutual arrangement and the type of objects in the set $\mathcal{F}$. Here, the object can be a line segment or a point. Concerning the mutual arrangement, the objects can intersect or overlap each other, lie on parallel lines, be at a distance from each other, and connect into a polygon. In this regard, the separating curve in CEF is either a bisector, a hyperbola branch, or a higher-order curve. It suffices to demonstrate the types of separating curves on an example of two objects. When the set $\mathcal{F}$ contains more than two elements, the separating curves are computed for each pair independently and then combined.

Bisector

There are three configurations when the separating curve is a bisector. First, consider the set $\mathcal{F}=\{F_1, F_2\}$ containing the pair of points. Each point creates the distance field of concentric circles (Figure 4.8). Let $P \in \mathbb{R}^2$be an arbitrary point on the separating curve, and $Q \in \mathbb{R}^2$ be the point on the separating curve that belongs to $\overline{F_1F_2}$. From Definition 30, $\overline{F_1P}=\overline{F_2P}= r$, as well as $\overline{F_1Q}=\overline{F_2Q}$. The triangle $\triangle F_1PF_2$ has two equal sides leading to $\overline{PQ}$ being a bisector [145]. Since this is valid for any $P \neq Q$, the resultant separating curve is the perpendicular bisector to $\overline{F_1F_2}$ (Figure 4.8).

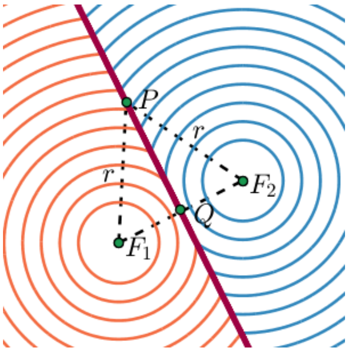

Figure 4.8: CEF of the pair of points. The separating curve is a bisector

Second, the separating curve is the bisector when the line segments share a common endpoint and have the same length (Figure 4.9a). Consider the set $\mathcal{F}=\{(F_1, F_2),(F_2, F_3)\}$ and an arbitrary point $P \in\mathbb{R}^2$ belonging to the separating curve. From (4.5):

$$\begin{cases} \mathsf{d}_{CED}(P, l_1) = \mathsf{d}_2(P, F_1) + \mathsf{d}_2(P, F_2) - \mathsf{d}_2(F_1, F_2) \\ \mathsf{d}_{CED}(P, l_2) = \mathsf{d}_2(P, F_3) + \mathsf{d}_2(P, F_2) - \mathsf{d}_2(F_2, F_3) \end{cases} \tag{4.9}$$

Since for the separating curve $\mathsf{d}_{CED}(P, l_1)$=$\mathsf{d}_{CED}(P, l_2)$ and the lengths of the line segments are the same, $\mathsf{d}_2(F_1, F_2) = \mathsf{d}_2(F_2, F_3)$, then $\mathsf{d}_2(P, F_1) = \mathsf{d}_2(P, F_3)$. Hence, such points P form the isosceles triangle $\triangle F_1PF_3$, and the resultant separating curve is the bisector that passes through the common point – F_2.

Finally, in certain scenarios, the bisector delineates the line segments of the same length without a common endpoint. They can belong to the same line (Figure 4.9b) or to the distinct lines, such that the shortest paths between

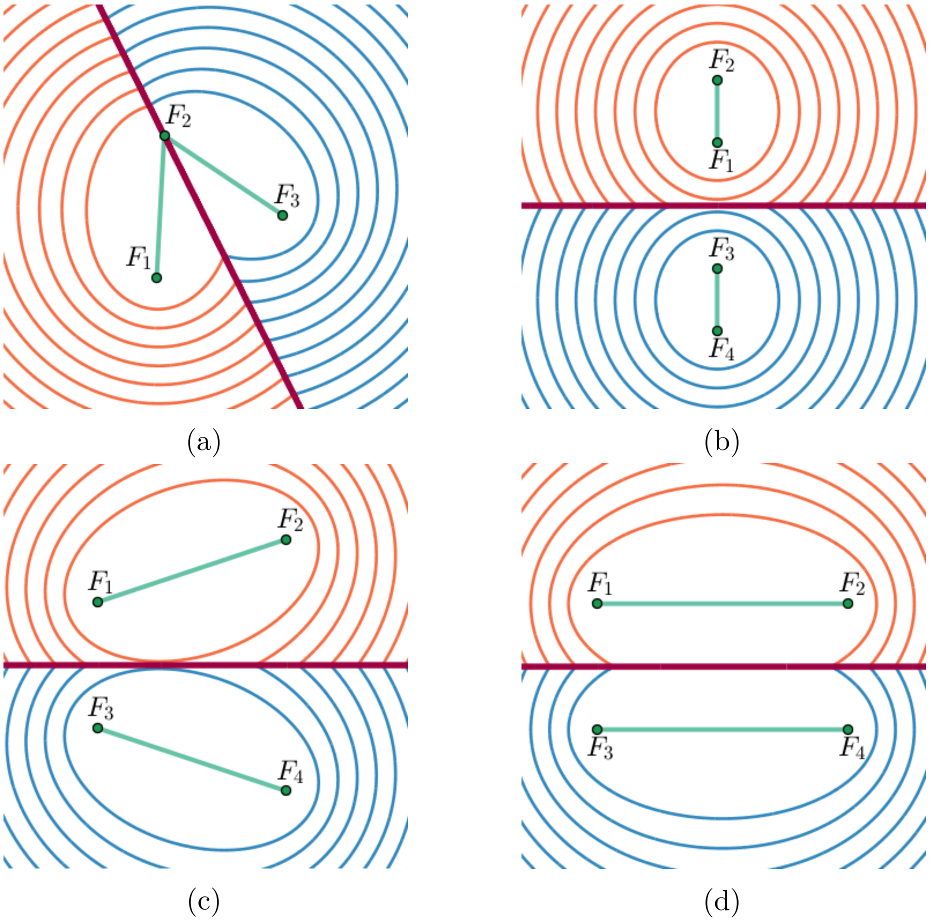

Figure 4.9: CEF of the pair of line segments. The separating curve is a bisector

the endpoints ($\overline{F_1F_3}$ and $\overline{F_2F_4}$ in Figure 4.9c and 4.9d) are parallel to each other and are perpendicular to the midline.

Hyperbola Branch

If two line segments with different lengths share a common endpoint, the separating curve is a hyperbola branch that passes through this common point (Figure 4.10). Consider the set $\mathcal{F} = \{(F_1, F_2), (F_2, F_3)\}$ and an arbitrary

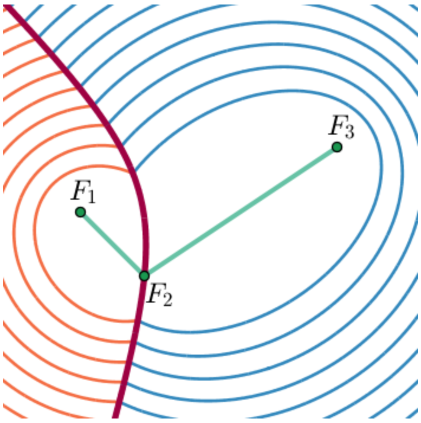

(a)

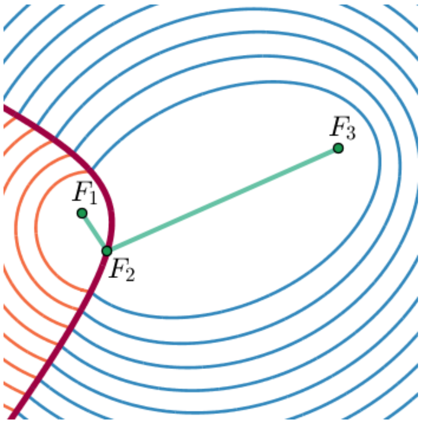

(b)

Figure 4.10: CEF of the pair of line segments. The separating curve is a hyperbola branch

point $P \in \mathbb{R}^2$ that belongs to the separating curve. According to (4.5):

$$\begin{cases} \mathsf{d}_{CED}(P, l_1) = \mathsf{d}_2(P, F_1) + \mathsf{d}_2(P, F_2) - \mathsf{d}_2(F_1, F_2) \\ \mathsf{d}_{CED}(P, l_2) = \mathsf{d}_2(P, F_2) + \mathsf{d}_2(P, F_3) - \mathsf{d}_2(F_2, F_3) \end{cases} \tag{4.10}$$

Equalizing $\mathsf{d}_{CED}(P, l_1)$ and $\mathsf{d}_{CED}(P, l_2)$ leads to:

$$\mathsf{d}_2(P, F_1) - \mathsf{d}_2(P, F_3) = \mathsf{d}_2(F_1, F_2) - \mathsf{d}_2(F_2, F_3) \tag{4.11}$$

(4.11) defines the hyperbola branch with the focal points F_1 and F_3 passing through the common point F_2. The position of F_2 influences the curvature of the hyperbola (Figure 4.10).

Multifocal Hyperbola Branch

In the remaining cases (Figure 4.11), the separating curve is a multifocal hyperbola branch (higher-order curve). In Figure 4.11a, the form of separating curve depends on the mutual arrangement of line segments (for instance, parallel to each other, non-intersecting, and intersecting) and on their length. The line segment with the greater length has the greater receptive field in the resultant CEF. In Figure 4.11b, the form of the separating curve depends on the position of the point relative to the line segment.

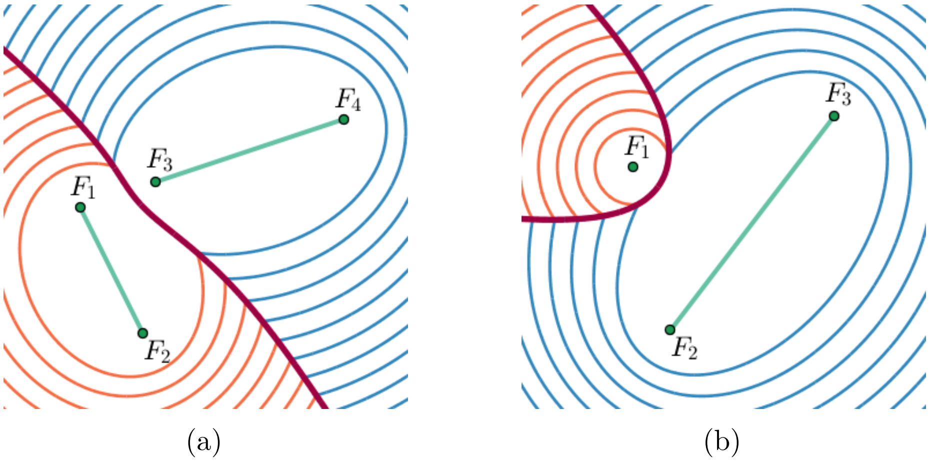

Figure 4.11: CEF of (a) the pair of line segments and (b) the point and the line segment. The separating curve is a multifocal hyperbola branch

4.2.2 Properties of CEF

Depending on the type of objects and their mutual arrangement, CEF is characterized by specific geometrical properties.

Property 19 (CEF of a point)**.** *CEF generated from the point $F \in \mathbb{R}^2$ contains concentric circles with the center at F.*

Proof. From (4.5) and (4.6), CEF of a single point equals:

$$\mathrm{CEF} = \{P \in \mathbb{R}^2 : \mathsf{d}_2(P, F) + \mathsf{d}_2(P, F) - \mathsf{d}_2(F, F)\} \tag{4.12}$$

(4.12) defines doubled DF_2 of a point. Thus, CEF contains concentric circles. □

Property 20 (CEF of a line segment)**.** *CEF of the line segment $\overline{F_1F_2}$ contains confocal ellipses with the focal points at F_1 and $F_2 \in \mathbb{R}^2$.*

Proof. According to Definition 27, d_{CED} generates the distance field containing confocal ellipses. So does CEF of this distance field. □

Property 21 (CEF values at the points of a line segment)**.** *The distance values along the line segment $\overline{F_1F_2}$ equal zero:*

$$CEF((1-\lambda)F_1 + \lambda F_2) = 0, \ \forall \lambda \in [0, 1] \tag{4.13}$$

Proof. For each point belonging to the line segment $\overline{F_1F_2}$, the distance sum to the endpoints equals the length of $\overline{F_1F_2}$. Regarding (4.5), CEF at these points is zero. □

Property 22 (CEF of the elements contained in a line segment)**.** *CEF of N line segments and points contained in the line segment $\overline{F_1F_2}$ is CEF generated only from $\overline{F_1F_2}$.*

Proof. Consider the pair of line segments $\overline{F_1F_2}$ and $\overline{F_3F_4}$, such that $\overline{F_3F_4} \subset \overline{F_1F_2}$ and the points are ordered as F_1, F_3, F_4, F_2. The length of $\overline{F_1F_2}$ is the sum of lengths of the line segments $\overline{F_1F_3}$, $\overline{F_3F_4}$, and $\overline{F_4F_2}$:

$$\mathsf{d}_2(F_1, F_2) = \mathsf{d}_2(F_1, F_3) + \mathsf{d}_2(F_3, F_4) + \mathsf{d}_2(F_4, F_2) \tag{4.14}$$

For the proof, it suffices to show that CEF of $\overline{F_1F_2}$ and $\overline{F_3F_4}$ is the distance field generated by $\overline{F_1F_2}$. By contradiction, from (4.5) and (4.6), for any point $P \in \mathbb{R}^2$, the following must be true:

$$\mathsf{d}_2(P, F_1) + \mathsf{d}_2(P, F_2) - \mathsf{d}_2(F_1, F_2) > \mathsf{d}_2(P, F_3) + \mathsf{d}_2(P, F_4) - \mathsf{d}_2(F_3, F_4) \tag{4.15}$$

According to (4.14), it is possible to simplify (4.15):

$$\mathsf{d}_2(P, F_1) + \mathsf{d}_2(P, F_2) - \mathsf{d}_2(F_1, F_3) - \mathsf{d}_2(F_4, F_2) > \mathsf{d}_2(P, F_3) + \mathsf{d}_2(P, F_4) \tag{4.16}$$

First, let the point P be a part of $\overline{F_1F_2}$. According to Property 21, in the distance field of $\overline{F_1F_2}$, all the points belonging to this line segment have zero distance values. In the distance field of $\overline{F_3F_4}$, the distance values along $\overline{F_3F_4}$ are zero, and the distance values along $\overline{F_1F_3}$ and $\overline{F_4F_2}$ are greater than zero. Thus, there is a contradiction in (4.15).

Second, let the point P be to the left of F_1 on the line containing $\overline{F_1F_2}$. Therefore, $\mathsf{d}_2(P, F_3) - \mathsf{d}_2(P, F_1) = \mathsf{d}_2(F_1, F_3)$ and $\mathsf{d}_2(P, F_2) - \mathsf{d}_2(P, F_4) = \mathsf{d}_2(F_4, F_2)$, resulting in (4.16) becoming

$$-\mathsf{d}_2(F_1, F_3) + \mathsf{d}_2(F_4, F_2) > \mathsf{d}_2(F_1, F_3) + \mathsf{d}_2(F_4, F_2) \tag{4.17}$$

(4.17) and, consequently, (4.15) are false. Contradiction. If the point P is to the right of F_2 and is on the line containing $\overline{F_1F_2}$, the reasoning is similar.

Third, let the point P be not on the line segment $\overline{F_1F_2}$. Permutation in (4.16) leads to:

$$\mathsf{d}_2(P, F_1) - \mathsf{d}_2(P, F_3) + \mathsf{d}_2(P, F_2) - \mathsf{d}_2(P, F_4) > \mathsf{d}_2(F_1, F_3) + \mathsf{d}_2(F_4, F_2) \tag{4.18}$$

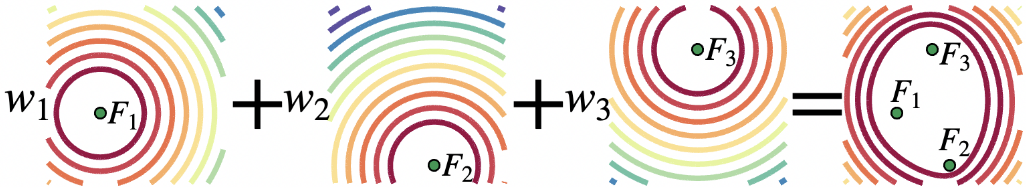

Figure 4.12: CMEF computed for the triplet of points with the corresponding weights $w_1 = 0.3$, $w_2 = 0.5$, and $w_3 = 0.7$

According to the triangle inequality [38],

$$\mathsf{d}_2(F_1, F_3) \geq |\ \mathsf{d}_2(P, F_1) - \mathsf{d}_2(P, F_3)| \tag{4.19}$$

$$\mathsf{d}_2(F_4, F_2) \geq |\ \mathsf{d}_2(P, F_2) - \mathsf{d}_2(P, F_4)| \tag{4.20}$$

Hence, (4.18) and, consequently, (4.15) does not hold. Contradiction.

Similarly, it can be shown that CEF of the line segment $\overline{F_1F_2}$ and the point $F_5 \subset \overline{F_1F_2}$ is the distance field of $\overline{F_1F_2}$. □

4.3 Confocal Multifocal Elliptic and Hyperbolic Fields (CMEF and CMHF)

With the reference to Definitions 17 to 19, the distance fields containing confocal multifocal ellipses and hyperbolas can be computed as a combination of multiple DF_2s.

Definition 31 (Confocal Multifocal Elliptic Field)**.** *Let $\mathcal{F} = \{F_1, F_2, \ldots, F_N\}$ be the set of N points with the positive weights $w_1, w_2, \ldots, w_N$. The sum of weighted DF_2s generated from $F_1, F_2, \ldots, F_N$ produces the distance field of confocal multifocal ellipses (Figure 4.12), called Confocal Multifocal Elliptic Field (CMEF).*

The example is illustrated in Figure 4.12. The DF_2s are generated from the triplet of points F_1, F_2, and F_3. Then, each point in these fields is multiplied by the corresponding weight, w_1, w_2, or w_3. Finally, CMEF is computed by assigning to each point the sum of its values in the weighted distance fields.

Definition 32 (Confocal Multifocal Hyperbolic Field). *Consider two sets of focal points $\mathcal{F} = \{F_1, F_2, \ldots, F_N\}$ and $\mathcal{G} = \{G_1, G_2, \ldots, G_M\}$. These points have the positive weights $w_1, w_2, \ldots, w_N$ and $\nu_1, \nu_2, \ldots, \nu_M$ respectively. The subtraction from the sum of weighted DF_2s generated from $\mathcal{F}$ the sum of weighted DF_2s generated from $\mathcal{G}$ produces the distance field of confocal multifocal hyperbolas (Figure 4.13), called Confocal Multifocal Hyperbolic Field (CMHF).*

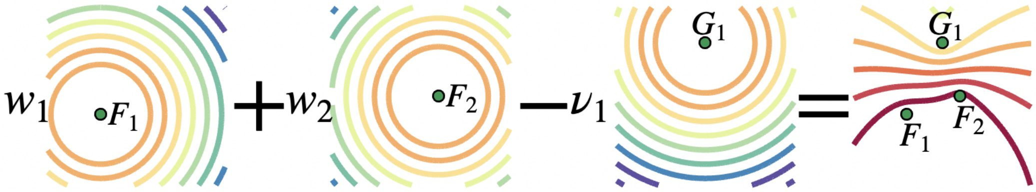

Figure 4.13: CMHF from the two sets of points $\mathcal{F} = \{F_1, F_2\}$ and $\mathcal{G} = \{G_1\}$ with the corresponding weights $w_1 = 0.3$, $w_2 = 0.5$, and $\nu_1 = 0.7$

An example in Figure 4.13 takes the point sets $\mathcal{F} = \{F_1, F_2\}$ and $\mathcal{G} = \{G_1\}$. First, DF_2s are computed for each points F_1, F_2, and G_1 and multiplied by the corresponding weight $w_1 = 0.3$, $w_2 = 0.5$, and $\nu_1 = 0.7$. Then, for each point in space, the distance values from DF_2s associated with the set $\mathcal{F}$ are added, whereas with the set $\mathcal{G}$ – subtracted.

4.4 Summary

This chapter illustrates how the identified geometrical properties of conics and generalized conics are applied to shape representation. In relation to the distance fields, the essence of the multifocal ellipses is to define the proximity to the objects, whereas the multifocal hyperbolas establish the tessellation of the space. A distinct feature of CEF is the impact mitigation for the elements contained inside a line segment (Property 22). Despite the number of elements, there will be no corresponding separating curve indicating their presence. An interpretation of the proposed distance fields by a combination of DF_2s enables an efficient representation. The discussed CEF has potential applications in classification and skeletonization, whereas CMEF and CMHF are suitable for optimization problems (like optimal facility location) and shape representation.

CHAPTER 5

Generating CEF, CMEF, and CMHF with Distance Transform

This chapter is based on the following publications:

Aysylu Gabdulkhakova, Walter G. Kropatsch:
Confocal Ellipse-based Distance and Confocal Elliptical Field for polygonal shapes. In Proceedings of the International Conference on Pattern Recognition, pages 3025–3030, 2018 [66]

Aysylu Gabdulkhakova, Maximilian Langer, Bernhard W. Langer, Walter G. Kropatsch:
Line Voronoi Diagrams Using Elliptical Distances. In Proceedings of the Joint IAPR International Workshop on Structural, Syntactic, and Statistical Pattern Recognition, pages 258–267, 2018 [69]

Aysylu Gabdulkhakova, Walter G. Kropatsch:
Generalized conics: properties and applications. In Proceedings of the International Conference on Pattern Recognition, pages 10728–10735, 2020 [67]

Digital geometry deals with N-dimensional digital spaces and is referred to as the *geometry of the computer screen* [92]. It adapts fundamental concepts of Euclidean geometry to the discrete case while considering a sampling of the Euclidean space. The transformation of a continuous function into a discrete form that can be processed by a computer is called *digitization* [94].

In 2D space, the result consists of *pixels* (Figure 5.1a). It creates a finite data structure defining a regular orthogonal grid. The shape digitization is performed at the cost of accuracy. For example, a line segment becomes a finite set of tiles [34], which is still perceived as a connected line segment by humans (Figure 5.1b).

The key principle of digital geometry is to take a notion in Euclidean geometry and see if it remains valid in its digital interpretation [92]. According to this principle, the present chapter revisits the properties and definitions of the Confocal Elliptic Field (CEF), Confocal Multifocal Elliptic Field (CMEF), and Confocal Multifocal Hyperbolic Field (CMHF) from the image processing perspective and introduces efficient algorithms for their computation based on the Distance Transform (DT).

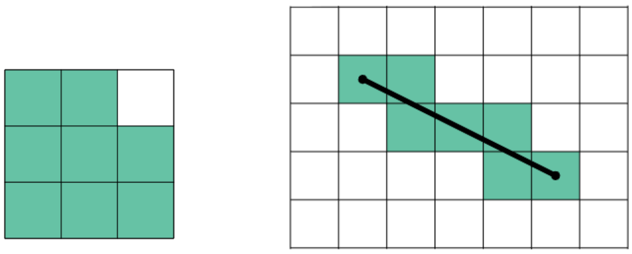

(a) pixel (white)

(b) digitized line segment (green)

Figure 5.1: The objects in the digital space

5.1 Preliminaries

While switching to the digital space, it is necessary to provide alternative definitions of the notions defined for the Euclidean space (Chapter 2). Here, the space is transformed to a digital image, whereas a point - to a pixel.

Definition 33 (2D digital image)**.** *A 2D digital image, I^2, is a function defined on a finite regular orthogonal subset of $\mathbb{Z}^2_{\geq 0}$ as follows:*

$$I^2 : \mathbb{Z}^2_{\geq 0} \to \mathbb{R}^N, \tag{5.1}$$

where $\mathbb{Z}^2_{\geq 0}$ corresponds to the coordinate set, and $\mathbb{R}^N$ - to the value set.

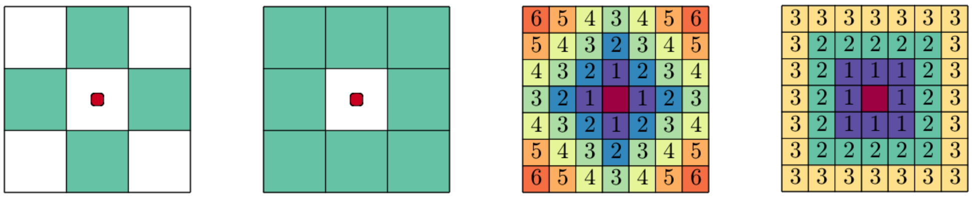

(a) 4-connectivity (b) 8-connectivity (c) City-Block (d) Chessboard

Figure 5.2: Distance value propagation depending on the connectivity type

Definition 34 (Pixel)**.** *The smallest unit of a 2D digital image is called pixel. It is characterized by a pair of non-negative integer coordinates and a value. The value can be expressed by, for instance, a single integer (for example, a binary image) or by a vector of integers (for example, an RGB image).*

A 2D digital image is a discrete set of pixels. Hereafter, the pixels are assumed to form a rectangular sampling grid. In the computer vision domain, a binary image contains two types of pixels: (1) feature (foreground) elements - pixels having a value 1, (2) non-feature (background) elements - pixels having a value 0 [179].

In image processing, the distance between two pixels reflects spatial information (for example, the distance from the non-feature element to the closest feature element) [29] or characteristic information (for instance, the probability that the non-feature element belongs to the set of feature elements) [113]. This thesis focuses on spatial information.

Such a spatial distance relies on the type of pixel connectivity and the metric. The connectivity type influences the distance value propagation towards the other pixels in an image. In a 2D image, 4-connectivity considers the adjacent pixels to be in the horizontal and vertical directions (Figure 5.2a). In the case of 8-connectivity, the pixel additionally has neighbors in the diagonal direction (Figure 5.2b). The examples of 4- and 8-connectivity-based distance value propagations are used in the City-Block (Figure 5.2c) and Chessboard (Figure 5.2d) metrics, respectively [29].

5.2 Distance Transform (DT)

Chapter 4 introduced the distance fields based on the properties of conics and generalized conics. In order to compute such fields in the discrete space efficiently, it is proposed to apply the classical image processing approach called Distance Transform (DT) [29].

Definition 35 (Distance Transform)**.** *Consider a 2D binary image I^2_{binary} and the set of feature elements $\mathcal{F}$. The Distance Transform (DT) is an operator that assigns to each pixel in I^2_{binary} the distance value to the nearest feature element with regard to the selected metric ($\mathsf{d_x}$):*

$$\mathcal{D}_{\mathcal{F}} = \{P \in I^2_{binary} : \min\{\mathsf{d_x}(P, F) | F \in \mathcal{F}\}\} \tag{5.2}$$

Note, for feature elements $\mathcal{D}_{\mathcal{F}}$ equals zero. As follows from the definition, the selected metric highly influences the properties of the resultant distance field. In the computer vision community, the Euclidean distance plays a crucial role since providing invariance under rotation, translation, and bending in 2D but not under scaling [148].

DT is a global operation whichx is computationally expensive [29]. A direct implementation of the Euclidean Distance Transform (DT_2) has a complexity of $O(N^4)$ [186]. Thus, the early approaches aimed at efficient solutions at the cost of approximating the Euclidean distance [157, 158]. Maurer et al. [115] introduced the algorithm to compute the exact DT_2 in linear time, whereas Ciesielski et al. [42] further improved this method. Various authors approached DT_2 in 3D space [30, 136].

DT is successfully applied in a wide variety of applications, such as image segmentation, object recognition, image matching, skeletonization, and shape analysis [42]. Concerning shape analysis, the distances are propagated from the interior of shape to its borders. Hence, to capture the shape structure, it is preferred to use the inverse DT by complementing the binary image [161]. Meyer et al. [121] took the discontinuities in the inverse DT_2 values to detect the boundaries of distinct overlapping objects. When applied to the problem of overlapping elliptic shapes, Talbot et al. [195] introduced Elliptical Distance Transform (LDT). Here, the Euclidean distance is substituted by the standard 2D harmonic oscillator equation. The optimization of the LDT series with various eccentricity and orientation parameters enables detecting the minimal set of maximal ellipses that cover the shape. The distance values are computed for the pairs of points. The next section introduces the DT-based method to generate CEF, CMEF, and CMHF.

5.3 CEF in Digital Space

DT makes it possible to adapt the continuous notions into digital space. In this regard, consider the interpretations of Definitions 25 to 30.

Definition 36 (Confocal ellipses from two pixels with DT_2)**.** *Let $\mathcal{F} = \{F_1, F_2\}$ be the pair of pixels in a 2D binary image I^2_{binary}. Confocal ellipses in the digital space are the sum of DT_2s generated from F_1 and F_2:*

$$\mathcal{DE}_{F_1F_2} = \{P \in I^2_{binary} : \mathcal{D}_{F_1}(P) + \mathcal{D}_{F_2}(P)\} \tag{5.3}$$

Strand [190] presented the idea of taking the sum of distance fields. It aimed at finding a minimal path between two pixels. Though, the resultant distance field was not analyzed and used from the geometrical perspective of confocal ellipses.

Definition 37 (Confocal hyperbolas from two pixels with DT_2)**.** *Consider the set of two pixels $\mathcal{F} = \{F_1, F_2\}$ in a 2D binary image I^2_{binary}. Confocal hyperbolas in digital space are obtained as the difference of the DT_2s generated from F_1 and F_2:*

$$\mathcal{DH}_{F_1F_2} = \{P \in I^2_{binary} : \mathcal{D}_{F_1}(P) - \mathcal{D}_{F_2}(P)\} \tag{5.4}$$

Property 23 (Distance value that equals the line segment length in DT_2)**.** *Let $\mathcal{D}_{F_1}(P)$ and $\mathcal{D}_{F_2}(P)$ be DT_2s of the pixels from the set $\mathcal{F}= \{F_1, F_2\}$. The length of $\overline{F_1F_2}$ equals the distance value of F_1 in $\mathcal{D}_{F_2}$, or the distance value of F_2 in $\mathcal{D}_{F_1}$:*

$$\mathcal{D}_{F_1}(F_2) = \mathcal{D}_{F_2}(F_1) = \mathsf{d}_2(F_1, F_2) \tag{5.5}$$

Definition 38 (Distance field of a line segment under CED with DT_2)**.** *Consider the line segment defined by two endpoints $\mathcal{F}= \{(F_1, F_2)\}$. The distance field of confocal ellipses with respect to CED using DT_2 is then expressed as $\overline{\mathcal{DE}}_{F_1F_2}$:*

$$\begin{aligned}
\overline{\mathcal{DE}}_{F_1F_2} = \{P \in I^2_{binary} \;:\; & \mathcal{DE}_{F_1F_2}(P) - \mathcal{DE}_{F_1F_2}(F_1) = && (5.6)\\
&= \mathcal{DE}_{F_1F_2}(P) - \mathcal{DE}_{F_1F_2}(F_2) = && (5.7)\\
&= \mathcal{D}_{F_1}(P) + \mathcal{D}_{F_2}(P) - \mathcal{D}_{F_1}(F_2) = && (5.8)\\
&= \mathcal{D}_{F_1}(P) + \mathcal{D}_{F_2}(P) - \mathcal{D}_{F_2}(F_1)\} && (5.9)
\end{aligned}$$

The substantial difference between $\mathcal{DE}_{F_1F_2}$ and $\overline{\mathcal{DE}}_{F_1F_2}$ is the subtraction of the $\overline{F_1F_2}$ length. In $\overline{\mathcal{DE}}_{F_1F_2}$, the distance value of its pixels is normalized and is independent from the distance between F_1 and F_2. So it is possible to combine multiple distance fields by, for example, applying the minimum operation to each pixel.

Definition 39 (Confocal Elliptic Field in terms of DT_2)**.** *Given the set of line segments and points defined as line segments with coinciding endpoints., $\mathcal{F}= \{(F_1, F_2), (F_3, F_4), ..., (F_{N-1}, F_N)\}$, the Confocal Elliptic Field in terms of DT_2 (CEF_{DT_2}) is obtained by the pixel-wise minimum operation that is applied to the distance fields $\overline{\mathcal{DE}}_{F_1F_2}$,..., $\overline{\mathcal{DE}}_{F_{N-1}F_N}$:*

$$CEF_{DT_2}(P) = \{P \in I^2_{binary} : \min\{\overline{\mathcal{DE}}_{F_{i-1}F_i}(P)|\ i = [2, 3, \ldots, N]\}\} \quad (5.10)$$

Property 24 ($\mathrm{CEF}_{\mathrm{DT}_2}$ values at the pixels of a line segment)**.** *Let $\overline{\mathcal{DE}}_{F_1F_2}$ be the distance field from the set $\mathcal{F}= \{(F_1, F_2)\}$. The distance values of the pixels belonging to the digital line segment $\overline{F_1F_2}$ are less than or equal to threshold τ:*

$$\overline{\mathcal{DE}}_{F_1F_2}((1-\lambda)F_1 + \lambda F_2) \leq \tau < \frac{\sqrt{2}}{2}\ pixel\_edge\_length,\ \forall\lambda \in [0, 1] \quad (5.11)$$

Proof. As opposed to the continuous case, the space discretization leads to an accuracy problem (Figure 5.3a). The pixel C belonging to the digital line segment $\overline{AB}$ (green) has an offset from the line segment connecting A and B (black). In other words, according to Definition 38, there is a difference between $\mathsf{d}_2(C, A)$+$\mathsf{d}_2(C, B)$ and $\mathsf{d}_2(A, B)$. This problem can be formulated using an ellipse (Figure 5.3b). Let A and B be the focal points, so $\mathsf{d}_2(A, B)$ equals $2f$. Then C is a point on the ellipse. $\overline{CC'}$ with the length δ denotes the offset of C from $\overline{AB}$. The point C' splits $\overline{AB}$ into two parts having the lengths $(2f - m)$ and m. The right triangles $\triangle AC'C$ and $\triangle BC'C$ enable expressing $\mathsf{d}_2(C, A)$ and $\mathsf{d}_2(C, B)$ by $\sqrt{(2f - m)^2 + \delta^2}$ and $\sqrt{m^2 + \delta^2}$ respectively. So the aim is to find a maximal value of the following function:

$$\tau(\delta, f, m) = \sqrt{(2f - m)^2 + \delta^2} + \sqrt{m^2 + \delta^2} - 2f \quad (5.12)$$

To do so, it suffices to estimate the values of δ, m, and f. Assume that f is fixed. What are the values of m and δ that maximize the sum of $\mathsf{d}_2(C, A)$ and $\mathsf{d}_2(C, B)$? For the triangle $\triangle ABC$, $\overline{CC'}$ expresses an altitude. Increasing δ leads to a larger area of $\triangle ABC$, thus, a larger product of $\mathsf{d}_2(C, A)$ and

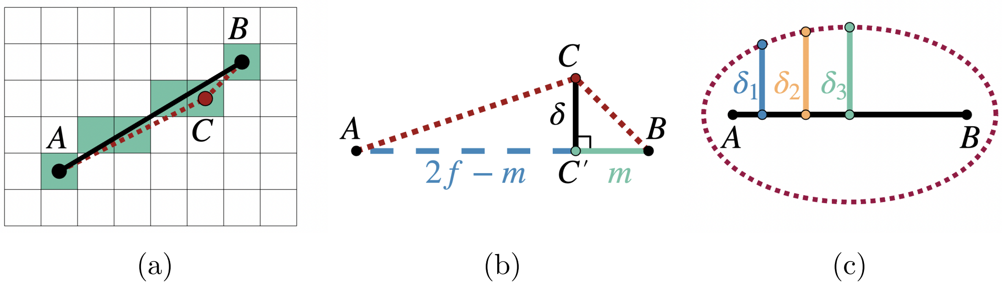

Figure 5.3: Discrepancy between digital and continuous line segments

$\mathsf{d}_2(C, B)$, and, consequently, a larger sum of $\mathsf{d}_2(C, A)$ and $\mathsf{d}_2(C, B)$ [70]. For a digital line segment, the maximal value of δ is $\frac{\sqrt{2}}{2}$ *pixel_edge_length*. It equals the maximal error within the pixel that corresponds to the distance between a center and a corner [100].

As for m, the position of C' also influences the sum of $\mathsf{d}_2(C, A)$ and $\mathsf{d}_2(C, B)$. The length of a semi-minor axis of the ellipse corresponds to a radius of its largest inscribed circle [154]. It means, in Figure 5.3c, $\delta_3 > \delta_2 > \delta_1$. Thus, the sum of $\mathsf{d}_2(C, A)$ and $\mathsf{d}_2(C, B)$ increases with the decrease of m.

Under the above assumptions, (5.12) reaches the largest value, when $m = 0$ and $\delta = \frac{\sqrt{2}}{2}$ *pixel_edge_length*. After substitution, (5.12) becomes:

$$\tau(f) = \sqrt{4f^2 + (\frac{\sqrt{2}}{2} pixel\_edge\_length)^2} + \frac{\sqrt{2}}{2} pixel\_edge\_length - 2f \tag{5.13}$$

(5.13) defines a hypothetical situation creating a triangle with a right angle $\widehat{ABC}$. The minimal error related to such a triangle is the maximal error for τ. Consider changing f. The minimal value of $2f$ is the distance between centers of two horizontally (or vertically) adjacent pixels, or *pixel_edge_length*. Substituting into (5.13), makes τ equal to:

$$\tau = (\sqrt{\frac{3}{2}} + \frac{\sqrt{2}}{2} - 1) pixel\_edge\_length \tag{5.14}$$

The maximal value of f is infinity:

$$\lim_{f\to\infty}\tau(f) = \lim_{f\to\infty}(\sqrt{4f^2+\frac{1}{2}} - (2f - \frac{\sqrt{2}}{2}))pixel\_edge\_length = \tag{5.15}$$

$$= \lim_{f\to\infty}\frac{(\sqrt{4f^2+\frac{1}{2}})^2 - (2f-\frac{\sqrt{2}}{2})^2}{\sqrt{4f^2+\frac{1}{2}} + (2f-\frac{\sqrt{2}}{2})}pixel\_edge\_length = \tag{5.16}$$

$$= \lim_{f\to\infty}\frac{4f^2+\frac{1}{2} - (4f^2 - 4\frac{\sqrt{2}}{2}f + \frac{1}{2})}{\sqrt{4f^2+\frac{1}{2}} + (2f-\frac{\sqrt{2}}{2})}pixel\_edge\_length = \tag{5.17}$$

$$= \lim_{f\to\infty}\frac{4\frac{\sqrt{2}}{2}f}{\sqrt{4f^2+\frac{1}{2}} + (2f-\frac{\sqrt{2}}{2})}pixel\_edge\_length = \tag{5.18}$$

$$= \lim_{f\to\infty}\frac{4\frac{\sqrt{2}}{2}f}{f(\sqrt{4+\frac{1}{2f^2}} + 2 - \frac{\sqrt{2}}{2f}))}pixel\_edge\_length = \tag{5.19}$$

$$= \frac{\sqrt{2}}{2}pixel\_edge\_length \tag{5.20}$$

As observed in (5.14) and (5.20), with an increase of f, the error decreases. Hence, using the threshold $\tau < \frac{\sqrt{2}}{2}pixel\_edge\_length$ enables handling the numerical error. □

Definition 40 (Receptive field in terms of DT_2)**.** *Consider CEF_{DT_2} generated from the set $\mathcal{F}$ containing N line segments and points defined as line segments with coinciding endpoints. The receptive field $\mathcal{DR}_i \in I^2_{binary}$ of the i-th line segment, l_i, is the set of pixels, where the absolute difference between CEF_{DT_2} and $\overline{\mathcal{DE}}_{l_i}$ is less than or equal to threshold τ:*

$$\underset{i\in[1,\ldots,N]}{\mathcal{DR}_i} = \{P \in I^2_{binary} : |CEF_{DT_2}(P) - \overline{\mathcal{DE}}_{l_i}(P)| \leq \tau \mid l_i \in \mathcal{F}\} \tag{5.21}$$

(5.21) creates an image where pixels with a distance value less than or equal to τ correspond to the receptive field $\mathcal{DR}_i$. The remaining pixels are assigned to a value that ensures the difference between various receptive fields by more than τ. The threshold τ affects a size of the receptive field: it becomes larger by increasing the τ. Setting τ to zero might cause discontinuities in a separating curve, since the receptive fields might not have pixels in common.

In the digital space, the definition of a separating curve (Definition 30) remains the same under the condition that the threshold τ is accounted. The separating curve between a pair of receptive fields contains only the pixels belonging to the overlap of these receptive fields.

Definition 41 (Separating curve in terms of DT_2)**.** *Consider the pair of receptive fields $\mathcal{DR}_i$ and $\mathcal{DR}_j$, $\mathcal{DR}_i \neq \mathcal{DR}_j$. The separating curve, $\mathcal{DS}_{ij}$, is the set of pixels where the absolute difference between these receptive fields is less than or equal to threshold τ:*

$$\mathcal{DS}_{\substack{ij \\ i,j\in[1,\ldots,N]; \\ i\neq j}} = \{P \in I^2_{binary} : (|\mathcal{DR}_i(P) - \mathcal{DR}_j(P)| \leq \tau)\} \tag{5.22}$$

5.4 CMEF and CMHF in Digital Space

Analogically to CEF, the continuous notions of CMEF and CMHF are revisited. This section redefines the above concepts with the use of DT.

Definition 42 (Confocal Multifocal Elliptic Field in terms of DT_2)**.** *Consider the set of points, $\mathcal{F}= \{F_1, F_2, ..., F_N\}$, and the corresponding DT_2s containing concentric circles, $\mathcal{D}_{F_1}$, $\mathcal{D}_{F_2}$,$\ldots$, $\mathcal{D}_{F_N}$. Each distance field is multiplied by the corresponding positive weight $w_1, w_2, \ldots, w_N$. The Confocal Multifocal Elliptic Field in terms of DT_2 ($CMEF_{DT_2}$) is computed as a pixel-wise sum among all the weighted distance fields:*

$$CMEF_{DT_2} = \{P \in I^2_{binary} : \sum_{i=1}^{N} w_i \mathcal{D}_{F_i}(P) \mid i = [1, \ldots, N]\} \tag{5.23}$$

Definition 43 (Confocal Multifocal Hyperbolic Field in terms of DT_2)**.** *Consider the two sets, $\mathcal{F}= \{F_1, F_2, ..., F_N\}$ and $\mathcal{G}= \{G_1, G_2, ..., G_M\}$. $\mathcal{D}_{F_1}$, $\mathcal{D}_{F_2}$,$\ldots$, $\mathcal{D}_{F_N}$, computed from the elements in $\mathcal{F}$, are linked to the positive weights $w_1, w_2, \ldots, w_N$, whereas $\mathcal{D}_{G_1}$, $\mathcal{D}_{G_2}$,$\ldots$, $\mathcal{D}_{G_M}$ from $\mathcal{G}$ elements are associated with the positive weights $\nu_1, \nu_2, \ldots, \nu_M$. The Confocal Multifocal Hyperbolic Field in terms of DT_2 ($CMHF_{DT_2}$) equals the pixel-wise difference between the sums of weighted distance fields:*

$$CMHF_{DT_2} = \{P \in I^2_{binary} : \sum_{i=1}^{N} w_i \mathcal{D}_{F_i}(P) - \sum_{j=1}^{M} \nu_j \mathcal{D}_{G_j}(P) \mid i = [1, \ldots, N], \\ j = [1, \ldots, M]\} \tag{5.24}$$

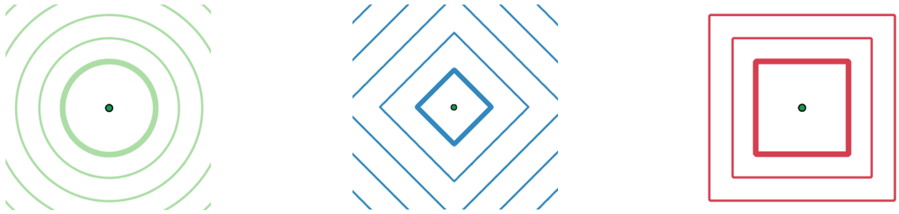

(a) Euclidean (DT_2) (b) City-Block (DT_1) (c) Chessboard (DT_∞)

Figure 5.4: The distance fields of the single point using the various metrics

5.5 $\mathrm{CEF}_{\mathrm{DT}}$ under the Various Metrics

According to Definition 38, $\mathrm{CEF}_{\mathrm{DT}_2}$ relies on the Euclidean distance. In principle, it is possible to use other metrics. This section illustrates and compares the results of applying the grid-based metrics such as the City-Block and Chessboard distances.

The City-Block distance (also referred to as Manhattan, or L_1-metric) in 2D considers the 4-connectivity distance value propagation. In other words, it measures the route length between two points along the regular grid at the right angles [98].

Definition 44 (City-Block distance)**.** *Given the pixels $P = (x_P, y_P)$ and $Q = (x_Q, y_Q)$, the City-Block distance equals the sum of absolute differences of their corresponding coordinates:*

$$\mathsf{d}_1(P, Q) = |x_P - x_Q| + |y_P - y_Q| \tag{5.25}$$

The Chessboard distance (alternatively Chebyshev distance, or L_∞-metric) in 2D considers the 8-connectivity distance value propagation and is the rotated and scaled equivalent of the planar City-Block distance [156].

Definition 45 (Chessboard distance)**.** *The Chessboard distance between the pixels $P = (x_P, y_P)$ and $Q = (x_Q, y_Q)$ equals the maximum of absolute differences of their corresponding coordinates:*

$$\mathsf{d}_\infty(P, Q) = \max(|x_P - x_Q|, |y_P - y_Q|) \tag{5.26}$$

The relation between the metrics is illustrated as follows. Let the two points, $P = (x_P, y_P)$ and $Q = (x_Q, y_Q)$, form the hypotenuse of the right triangle. The Euclidean distance equals the length of the hypotenuse, the

Chessboard distance matches the length of the longest cathetus, and the City-Block distance is the sum of the catheti lengths.

For a single pixel, the DT_2 level sets are concentric circles (Figure 5.4a). In contrast, the City-Block Distance Transform (DT_1) and the Chessboard Distance Transform (DT_∞) form rhombic and square level sets (Figure 5.4b and 5.4c respectively).

Now, compare the distance fields for the line segment (Figure 5.5 and 5.6). DT_2, DT_1, and DT_∞ compute for any pixel P the distance to the closest pixel belonging to $\overline{F_1F_2}$ with regard to the selected metric (Figure 5.5). $\mathrm{CEF}_{\mathrm{DT}}$ is based on (4.5). Substitution of the Euclidean metric by the City-Block or Chessboard produces the distance fields which level sets differ from confocal ellipses (Figure 5.6). From the computer vision perspective, the Euclidean distance provides the invariance to translation and rotation [148]. In contrast, the Chessboard and City-Block distances depend on the rotation of the coordinate system but are invariant to translation [30,98]. Consequently, this is reflected in $\mathrm{CEF}_{\mathrm{DT}}$. Observe the Euclidean (Figure 5.5a, 5.5d, 5.6a and 5.6d), City-Block (Figure 5.5b, 5.5e, 5.6b and 5.6e) and Chessboard (Figure 5.5c, 5.5f, 5.6c and 5.6f) distance fields.

DT and $\mathrm{CEF}_{\mathrm{DT}}$ fields of a line segment, generated using the Chessboard and City-Block metrics, differ from each other. The following properties characterize the two exceptions. Here, $\mathrm{CEF}_{\mathrm{DT}}$ optimizes the computational efficiency while considering only the pair of endpoints regardless of the line segment discretization.

Property 25 (Similarity between DT_1 and $\mathrm{CEF}_{\mathrm{DT}_1}$)**.** *$DT_1$ and CEF_{DT_1} generate identical level sets if the line segment is parallel to one of the axes (Figure 5.5b and 5.6b). The difference is in the distance values: CEF_{DT_1} is twice as large as DT_1.*

Proof. Assume λ and r denote the distance values of the corresponding level sets of DT_1 and $\mathrm{CEF}_{\mathrm{DT}_1}$ (Figure 5.7). It suffices to show that $\lambda = 2r$ for four characteristic pixels: P_1, P_2, P_3, and P_4. Let an arbitrary pixel P correspond to the λ level set of the $\mathrm{CEF}_{\mathrm{DT}_1}$. Assume that F_1 and F_2 are the focal points. Substitute the Euclidean distance in (4.5):

$$\lambda = \mathsf{d}_{CED}(P, \overline{F_1F_2}) = \mathsf{d}_1(P, F_1) + \mathsf{d}_1(P, F_2) - \mathsf{d}_1(F_1, F_2) \tag{5.27}$$

The right side of (5.27) can be rewritten as follows:

$$(|x_P - x_{F_1}| + |y_P - y_{F_1}|) + (|x_P - x_{F_2}| + |y_P - y_{F_2}|) - (|x_{F_1} - x_{F_2}| + |y_{F_1} - y_{F_2}|) \tag{5.28}$$

(a) Euclidean (DT_2) (b) City-Block (DT_1) (c) Chessboard (DT_∞)

(d) Euclidean (DT_2) (e) City-Block (DT_1) (f) Chessboard (DT_∞)

Figure 5.5: DT of a line segment using the various metrics

(a) Euclidean (CEF_{DT_2}) (b) City-Block (CEF_{DT_1}) (c) Chessboard (CEF_{DT_∞})

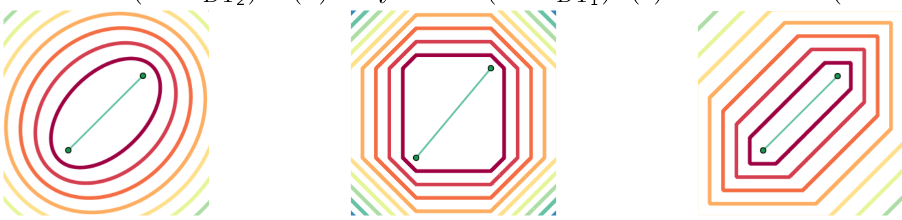

(d) Euclidean (CEF_{DT_2}) (e) City-Block (CEF_{DT_1}) (f) Chessboard (CEF_{DT_∞})

Figure 5.6: CEF_{DT} of a line segment using the various metrics

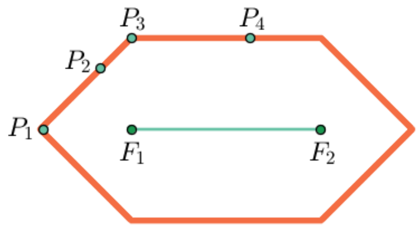

Figure 5.7: Characteristic pixels P_1, P_2, P_3, and P_4 of a single λ level set

In the case of $P = P_1$, the y-coordinates are identical for P_1, F_1, and F_2, whereas the x-coordinates are related as $x_{P_1} \leq x_{F_1} \leq x_{F_2}$. Thus, (5.28) becomes:

$$x_{F_1} - x_{P_1} + y_{P_1} - y_{F_1} + x_{F_2} - x_{P_1} + y_{P_1} - y_{F_2} - x_{F_2} + x_{F_1} + y_{F_1} - y_{F_2} = 2(x_{F_1} - x_{P_1}) \tag{5.29}$$

At the same time DT_1-value of P_1 equals $(x_{F_1} - x_{P_1})$ and, thus:

$$\lambda = 2\mathsf{d}_1(P_1, F_1) = 2r \tag{5.30}$$

Similarly, it can be shown that (5.30) is valid for P_2, P_3, and P_4. $\square$

Property 25 does not hold true when the line segment is not parallel to any of the axes (Figure 5.5e and 5.6e). It can be proven by comparing $\mathrm{CEF}_{\mathrm{DT}_1}$ and DT_1 values for all possible relations between x- and y-coordinates of an arbitrary point P and the line segment $\overline{F_1F_2}$.

Property 26 (Similarity between DT_∞ and $\mathrm{CEF}_{\mathrm{DT}_\infty}$)**.** *$DT_\infty$ and CEF_{DT_∞} generate identical level sets when a line segment is rotated by $45°, 135°, 225°$, or $315°$ about one of the axes (Figure 5.5f and 5.6f). The difference is in the distance values: CEF_{DT_∞} is twice as large as DT_∞.*

Proof. According to Definition 45, the DT_∞ level sets of a single point are concentric squares (Figure 5.4c). In Figure 5.8, consider the level sets with the centers at F_1, F_2, and F_P passing through P and the level set containing F_1 with the center at F_2. Here, the point F_P denotes the closest point to P in terms of the Chessboard distance. In DT_∞, the distance value of P equals half of the side length of the smallest square which center is on $\overline{F_1F_2}$. Such a square has a center at F_P and the length of its side equals $2l$. Consequently, the DT_∞ value of P is l.

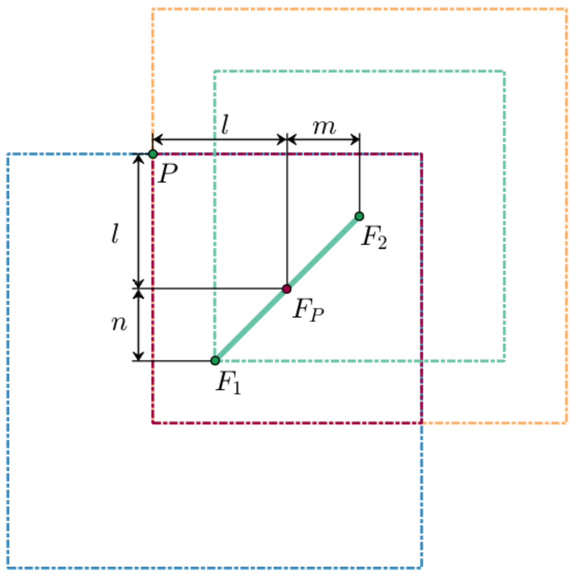

Figure 5.8: Computing the $\mathrm{CEF}_{\mathrm{DT}_\infty}$ and DT_∞ values of the line segment rotated by 45°

Assume λ denotes the $\mathrm{CEF}_{\mathrm{DT}_\infty}$ value of P. According to (4.5) it equals:

$$\lambda = \mathsf{d}_{CED}(P, \overline{F_1F_2}) = \mathsf{d}_\infty(P, F_1) + \mathsf{d}_\infty(P, F_2) - \mathsf{d}_\infty(F_1, F_2) \tag{5.31}$$

Express $\mathsf{d}_\infty(P, F_1)$ and $\mathsf{d}_\infty(P, F_2)$ using l (Figure 5.8):

$$\begin{cases} \mathsf{d}_\infty(P, F_1) = l + n \\ \mathsf{d}_\infty(P, F_2) = l + m \end{cases} \tag{5.32}$$

Since the line segment $\overline{F_1F_2}$ is rotated by 45°, the sides of the right triangles with a hypotenuse along $\overline{F_1F_2}$ are equal:

$$\mathsf{d}_\infty(F_1, F_2) = m + n \tag{5.33}$$

After substituting the estimates from (5.32) and (5.33) to (5.31):

$$\lambda = l + n + l + m - (m + n) = 2l \tag{5.34}$$

From (5.34), the value of P in $\mathrm{CEF}_{\mathrm{DT}_\infty}$ is twice as large as its DT_∞ value.

□

5.6 Discussion

In this section, $\mathrm{CEF}_{\mathrm{DT}}$, $\mathrm{CMEF}_{\mathrm{DT}}$, and $\mathrm{CMHF}_{\mathrm{DT}}$ are evaluated according to the proposed evaluation criteria. The results are summarized in Table 5.1.

<table>
<tr><th></th><th>$\mathrm{CEF}_{\mathrm{DT}}$</th><th>$\mathrm{CMEF}_{\mathrm{DT}}$</th><th>$\mathrm{CMHF}_{\mathrm{DT}}$</th></tr>
<tr><td rowspan="2">Scope</td><td>any 2D set of points and line segments</td><td colspan="2">focal points can be points, line segments, or shapes</td></tr>
<tr><td colspan="3">extension to higher dimensions</td></tr>
<tr><td>Uniqueness</td><td colspan="3">unique for the set of focal points (with weights)</td></tr>
<tr><td>Invariance</td><td colspan="3">• Euclidean: invariant to rotation, translation, and scaling
• City-Block: invariant to translation, and scaling
• Chessboard: invariant to translation, and scaling</td></tr>
<tr><td rowspan="2">Stability</td><td rowspan="2">stable in the cases satisfying Property 22</td><td colspan="2">every point affects the representation</td></tr>
<tr><td>global minimum is less affected by distant outliers</td><td></td></tr>
<tr><td rowspan="6">Accuracy</td><td colspan="3">• Euclidean:</td></tr>
<tr><td>$\frac{3\sqrt{2}}{2}$ pixel_edge_length</td><td colspan="2">$\frac{N\sqrt{2}}{2}$ pixel_edge_length</td></tr>
<tr><td colspan="3">• City-Block:</td></tr>
<tr><td>3 pixel_edge_length</td><td colspan="2">N pixel_edge_length</td></tr>
<tr><td colspan="3">• Chessboard:</td></tr>
<tr><td>$\frac{3}{2}$pixel_edge_length</td><td colspan="2">$\frac{N}{2}$ pixel_edge_length</td></tr>
<tr><td rowspan="4">Efficiency</td><td colspan="3">• Sequential (Euclidean):</td></tr>
<tr><td colspan="2">$O(N \times W \times H)$ [100]</td><td>$O(W \times H)$</td></tr>
<tr><td colspan="3">• Parallel (Euclidean):</td></tr>
<tr><td colspan="2">$O(N)$ [100]</td><td>$O(1)$</td></tr>
<tr><td>Abstraction</td><td colspan="3">enables hierarchical representation</td></tr>
</table>

Table 5.1: Evaluation of the representations $\mathrm{CEF}_{\mathrm{DT}}$, $\mathrm{CMEF}_{\mathrm{DT}}$, and $\mathrm{CMHF}_{\mathrm{DT}}$

Scope

By Definition 24, CED measures the distance between a point and a line segment. So, it is applicable to sets of line segments which, in fact, can degenerate into points. $\mathrm{CEF}_{\mathrm{DT}_2}$ relies on CED as a metric and is a combination of DT_2s. In turn, DT_2 is defined everywhere in space. Hence, $\mathrm{CEF}_{\mathrm{DT}_2}$ represents space tessellation of any 2D set of points and line segments. With the reference to Section 4.1.3, CED enables extension of the representation to higher dimensions by considering more coordinates. Figure 5.9 shows the 3D representation of $\mathrm{CEF}_{\mathrm{DT}_2}$ from two line segments, $\overline{F_1F_2}$ and $\overline{F_2F_3}$. The corresponding isosurfaces are a fusion of prolate spheroids (orange), each obtained by a rotation of the ellipse about its major axis. Since the line segments have a common endpoint, the spheroids are separated by the hyperbolic surface (blue).

$\mathrm{CMEF}_{\mathrm{DT}_2}$ and $\mathrm{CMHF}_{\mathrm{DT}_2}$ are sums and differences of weighted distance fields, expressing the distances to the set of focal points. In principle, the focal point is not limited to a point or a line segment and could be even a shape. Consequently, the distance fields could be of various types. For instance, consider the set of line segments where the distance field of each element is expressed by $\mathrm{CEF}_{\mathrm{DT}_2}$. The corresponding $\mathrm{CMEF}_{\mathrm{DT}_2}$ becomes the pixel-wise sum of multiple $\mathrm{CEF}_{\mathrm{DT}_2}$s. Eventually, these representations are not limited to a specific class of shapes and can be extended to higher dimensions. The statements remain valid for other metrics (for example, City-Block or Chessboard) as well.

Uniqueness

According to Theorem 4, CED is a metric. With the reference to Definition 7, each pixel is associated with a unique non-negative number. For the given shape there exist a unique $\mathrm{CEF}_{\mathrm{DT}_2}$. At the same time, each pixel in $\mathrm{CMEF}_{\mathrm{DT}_2}$ is associated with a weighted sum of unique distance fields. Hence, this representation is also unique. Eventually, $\mathrm{CMHF}_{\mathrm{DT}_2}$ unambiguously expresses the distance value distribution for the pair of $\mathrm{CMEF}_{\mathrm{DT}_2}$-fields. The same holds when substituting the Euclidean distance with City-Block or Chessboard.

Invariance

Depending on the distance metric, the invariance to transformations differs. $\mathrm{CEF}_{\mathrm{DT}_2}$, $\mathrm{CMEF}_{\mathrm{DT}_2}$, and $\mathrm{CMHF}_{\mathrm{DT}_2}$ are a combination of multiple DT_2s, which,

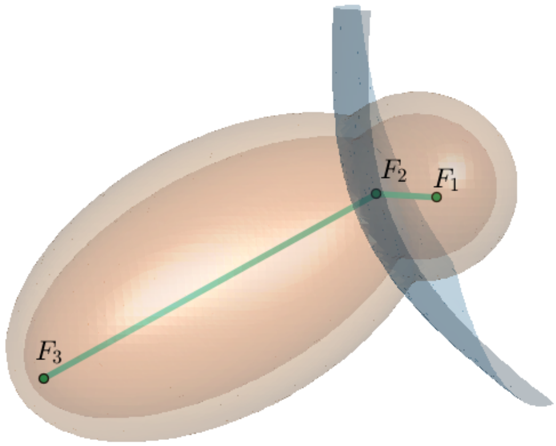

Figure 5.9: The isosurfaces of $\mathrm{CEF}_{\mathrm{DT}_2}$ generated from two line segments

in turn, are equivariant under rotation and translation [148]. Substitution of the Euclidean distance by City-Block or Chessboard limits the invariance possibilities to translation [30, 98]. A normalization strategy enables achieving scale invariance for the discussed metrics [140].

Stability

Essentially, $\mathrm{CEF}_{\mathrm{DT}}$ is a form of DT that uses CED instead of the Euclidean metric. DT is sensitive even to a single noise-point [132]. So is the $\mathrm{CEF}_{\mathrm{DT}}$. Although, there is an exception. This effect is mitigated by Property 22. The distance field only reflects the values of the line segment that completely encloses other feature elements.

In $\mathrm{CMEF}_{\mathrm{DT}}$, every point is mapped to the sum of the distances to the focal points. Thus, the distance field is stable, if the new focal point is equidistant to all points in space. This is impossible. $\mathrm{CMHF}_{\mathrm{DT}}$ is a difference between a pair of $\mathrm{CMEF}_{\mathrm{DT}}$. Hence, every element in the set of focal points impacts these representations.

In $\mathrm{CMEF}_{\mathrm{DT}}$, every element influences the level sets. Although, if there is a collection of spatially close elements, the distant outlier does not affect strongly the location of the global minimum. Imagine this configuration from far away: the collection of shapes degenerates into a super-point while the outlier stays as it is. The distance to the super-point equals the sum of the distances to its elements. Eventually, it can be encoded as an egg-shape, where the largest weight is associated with the super-point. According to Theorem 1, for the egg-shape the focal point with the larger weight is mapped to the minimum distance value. In this case, in the area of the super-point.

Accuracy

Space discretization leads to an accuracy problem: all points within the pixel have the same distance value related to its center. For the Euclidean distance, the maximal error is at the pixel corners and equals $\frac{\sqrt{2}}{2}$ *pixel_edge_length* (or a half of the pixel diagonal) [100]. For the City-Block and Chessboard distances such error is *pixel_edge_length* and $\frac{1}{2}$ *pixel_edge_length* correspondingly.

CED implies using the distance field three times (Definition 38). Thus, the maximal error in $\mathrm{CEF}_{\mathrm{DT}_2}$ equals $\frac{3\sqrt{2}}{2}$ *pixel_edge_length*, in $\mathrm{CEF}_{\mathrm{DT}_1}$ 3 *pixel_edge_length*, and in $\mathrm{CEF}_{\mathrm{DT}_\infty}$ $\frac{3}{2}$ *pixel_edge_length*.

$\mathrm{CMEF}_{\mathrm{DT}}$ and $\mathrm{CMHF}_{\mathrm{DT}}$ consider the sum (and subtraction) of N distance fields. It results in the total error of $\frac{N\sqrt{2}}{2}$ *pixel_edge_length* for the Euclidean, N *pixel_edge_length* for the City-Block, and $\frac{N}{2}$ *pixel_edge_length* for the Chessboard distance.

Efficiency

The pseudocode of $\mathrm{CEF}_{\mathrm{DT}_2}$ implementation is shown in Algorithm 5.1. The input contains the binary image, I^2_{binary} of size $W \times H$, and the set of M pairs of N points, $\mathcal{F}$. The first step (Lines 1-3) computes DT_2s of the points. Since DT_2 is linear with regard to the number of pixels [115], the complexity of the step is $O(N \times W \times H)$. The next loop (Lines 4-7) aims at computing the distance fields of confocal ellipses. Taking the pixel-wise sums for pairs of DT_2s has the complexity of $O(M \times W \times H)$. The final step (Lines 8-15) computes $\mathrm{CEF}_{\mathrm{DT}_2}$ as the pixel-wise minimum operation among M distance fields with the complexity of $O(M \times W \times H)$. If all the steps are performed sequentially, then the total worst-case complexity of the algorithm is $O(N \times W \times H)$.

Each step has a potential for parallel execution. The computation of DT_2s and the confocal ellipses can be distributed with respect to the points and line segments, whereas the pixel-wise minimum operation – with respect to each pixel. This leads to the total parallel complexity of $O(W \times H)$. Langer [100] proposed the alternative algorithm for DT_2 (Lines 1-3). It takes a precomputed DT_2 of a point at the center. This DT_2 is twice as large as the input binary image. Instead of computing DT_2 for each point, it needs only

---

Algorithm 5.1: Confocal Elliptic Field using DT (CEF_{DT_2})

Data: Input binary image I^2_{binary} of size $W \times H$; set $\mathcal{F}$ containing M pairs of N points

Result: Confocal Elliptic Field in terms of DT_2 ($\mathrm{CEF}_{\mathrm{DT}_2}$)

for $n \leftarrow 1$ **to** N **do**
    $\mathcal{D}_{F_n} \longleftarrow compute\_\mathrm{DT}_2(F_n)$;
end
foreach $f_m \in \mathcal{F}, m \in [1, \ldots, M]$ **do**
    $(F_i, F_j) \longleftarrow get\_feature\_elements(f_m)$;
    $\overline{\mathcal{DE}}_m \longleftarrow \mathcal{D}_{F_i} + \mathcal{D}_{F_j} - \mathcal{D}_{F_i}(F_j)$;
end
foreach $[w, h] \in W \times H$ **do**
    $\mathrm{CEF}_{\mathrm{DT}_2}[w, h] \longleftarrow \infty$;
end
foreach $[w, h] \in W \times H$ **do**
    for $m \leftarrow 1$ **to** M **do**
        $\mathrm{CEF}_{\mathrm{DT}_2}[w, h] \longleftarrow min(\overline{\mathcal{DE}}_m[w, h], \mathrm{CEF}_{\mathrm{DT}_2}[w, h])$;
    end
end

---

to sample the corresponding part of the precomputed distance field. Hence, the actual parallel complexity depends only on the number of points, $O(N)$.

Algorithm 5.2 describes the computation of separating curves. It follows Algorithm 5.1, hence, the set of distance fields of confocal ellipses ($\overline{\mathcal{DE}}_1$, $\ldots$,$\overline{\mathcal{DE}}_M$) and $\mathrm{CEF}_{\mathrm{DT}_2}$ are provided as an input. The proposed steps find the separating curve according to Definition 41. The similar approach is described in [88]. First (Line 1-3), the receptive fields are computed as the difference between $\mathrm{CEF}_{\mathrm{DT}_2}$ and the distance fields of confocal ellipses. If the difference in distance values is less than or equal to the threshold τ, then the pixel belongs to the receptive field. The complexity of this step equals $O(M \times W \times H)$, where M is the number of the receptive fields, $W \times H$ is the total number of pixels in an image. The next step (Line 4-10), computes the separating curves by finding the common pixels of multiple receptive fields. The complexity of this step, as well as total complexity of the algorithm, is $O(M^2 \times W \times H)$. Algorithm 5.2 can be implemented in a distributed manner, thus, simplifying the total complexity to $O(M^2)$.

Langer [100] proposed the efficient solution that maps pixels of receptive fields with labels. Each label uniquely represents the element in the set $\mathcal{F}$. The neighboring pixels with different labels are part of the separating curve. In this case, the parallel computational complexity equals $O(M)$, although the skeleton is not one-pixel thick.

Algorithm 5.2: Separating Curves

Data: Confocal Elliptic Field in terms of DT_2 ($\mathrm{CEF}_{\mathrm{DT}_2}$); M distance maps of confocal ellipses $\overline{\mathcal{DE}}_1, \ldots, \overline{\mathcal{DE}}_M$; threshold τ

Result: Separating curves $\mathcal{DS}$

for $m \leftarrow 1$ **to** M **do**
    $\mathcal{DR}_m \longleftarrow \mid \mathrm{CEF}_{\mathrm{DT}_2} - \overline{\mathcal{DE}}_m \mid \leq \tau$;
end
for $l \leftarrow 1$ **to** M **do**
    for $k \leftarrow 1$ **to** M **do**
        if $l \neq k$ **then**
            $\mathcal{DS}_{lk} \longleftarrow \mid \mathcal{DR}_l - \mathcal{DR}_k \mid \leq \tau$;
        end
    end
end

Algorithm 5.3 shows the computation of $\mathrm{CMEF}_{\mathrm{DT}_2}$. As an input it takes the set of N points. The whole process considers the pixel-wise sums among all the distance fields $\mathcal{D}_{F_1}, \ldots, \mathcal{D}_{F_N}$ multiplied by the respective weight. Hence, the total sequential complexity equals $O(N \times W \times H)$, where $W \times H$ is the number of pixels in an image. Computation of $\mathrm{CMEF}_{\mathrm{DT}_2}$ can be implemented in a distributed manner on the pixel level using the precomputed distance fields. This leads to the actual parallel complexity of $O(N)$.

Eventually, the pseudocode for $\mathrm{CMHF}_{\mathrm{DT}_2}$ is given in Algorithm 5.4. It has the linear computational complexity on the number of image pixels.

Abstraction

Similar to the work of Rosin et al. [159], scale-space $\mathrm{CEF}_{\mathrm{DT}_2}$ is achievable by considering various levels of object's discretization.

Algorithm 5.3: Confocal Multifocal Elliptic Field in terms of DT_2 ($\mathrm{CMEF}_{\mathrm{DT}_2}$)

Data: Set $\mathcal{F}$ containing N points; weights $w_1, w_2, \ldots, w_N$
Result: Confocal Multifocal Elliptic Field in terms of DT_2 ($\mathrm{CMEF}_{\mathrm{DT}_2}$)

for $n \leftarrow 1$ **to** N **do**
  $\mathcal{D}_{F_n} \longleftarrow$ *compute*_$\mathrm{DT}_2(F_n)$;
end
$\mathrm{CMEF}_{\mathrm{DT}_2} \longleftarrow 0$;
for $n \leftarrow 1$ **to** N **do**
  $\mathrm{CMEF}_{\mathrm{DT}_2} \longleftarrow \mathrm{CMEF}_{\mathrm{DT}_2} + w_n \mathcal{D}_{F_n}$;
end

Algorithm 5.4: Confocal Multifocal Hyperbolic Field in terms of DT_2 ($\mathrm{CMHF}_{\mathrm{DT}_2}$)

Data: A pair of distance fields containing multifocal ellipses $\mathrm{CMEF}_{\mathrm{DT}_2}{}'$ and $\mathrm{CMEF}_{\mathrm{DT}_2}{}''$
Result: Confocal Multifocal Hyperbolic Field in terms of DT_2 ($\mathrm{CMHF}_{\mathrm{DT}_2}$)

$\mathrm{CMHF}_{\mathrm{DT}_2} \longleftarrow \mathrm{CMEF}_{\mathrm{DT}_2}{}'$ - $\mathrm{CMEF}_{\mathrm{DT}_2}{}''$;

5.7 Summary

This chapter contributed to the state of the art by adapting Confocal Elliptic Field (CEF), the separating curves, Confocal Multifocal Elliptic Field (CMEF) and Confocal Multifocal Hyperbolic Field (CMHF) to digital space with the use of Distance Transform (DT). The fact that CEF, CMEF, and CMHF are composed of DF_2s, enables expressing them with DT in digital space. This technique requires a threshold to cope with numerical instabilities. Despite sensitivity of $\mathrm{CMEF}_{\mathrm{DT}}$ level sets to every feature element, the position of the global minimum in this field is less affected by the distant outliers. Substitution of the Euclidean metric by City-Block and Chessboard results in losing the rotation equivariance. In exceptional cases $\mathrm{CEF}_{\mathrm{DT}_1}$ and $\mathrm{CEF}_{\mathrm{DT}_\infty}$ are identical to the classical distance fields. Consequently, in the corresponding scenarios, DT_1 and DT_∞ can be computed efficiently by applying the $\mathrm{CEF}_{\mathrm{DT}}$ algorithm.

CHAPTER 6

Elliptic Line Voronoi Diagram

This chapter is based on the following publications:

Aysylu Gabdulkhakova, Maximilian Langer, Bernhard W. Langer, Walter G. Kropatsch: *Line Voronoi Diagrams Using Elliptical Distances.* In Proceedings of the Joint IAPR International Workshop on Structural, Syntactic, and Statistical Pattern Recognition, pages 258–267, 2018 [69]

Chapters 4 and 5 discussed the distance field computation using CED as a metric in continuous and digital spaces, respectively. While reflecting proximity to objects in a target set, space tessellation in a distance field is, in principle, a mapping of the Voronoi regions onto a digital grid [133].

The Voronoi Diagram (VD), or the Dirichlet Tessellation, is a fundamental concept used in various disciplines [13]. The mathematicians Dirichlet [55] and Voronoy [202] introduced the original concept formally, whereas Shamos and Hoey [175] presented it in the field of computational geometry. This geometrical construct is applied in a vast variety of applications [192], such as motion planning [26, 65], skeletonization [133, 134], point-location [59], clustering [171], segmentation [91], and finite element analysis [176].

VD is a data structure that provides a space tessellation into *cells* based on proximity to the given set of objects, called *sites*. Each point in space is associated with a closest site among the set. The points corresponding to the same site form the cell. The notion of proximity is interpreted from two perspectives. On one side, it is a metric that defines a distance between objects. The properties and application areas of different metrics in 2D are thoroughly discussed in the literature [12]: City-Block [80], Euclidean [57], L_p [102], convex distance functions [39], convex polygon-offset distance function [20], crystal growth [169], skew distance [3], and power distance [10]. Klein et al. [93] introduced the analysis of metric classes and their impact on VD properties.

On the other side, the proximity depends on types of objects and their representation, especially in the digital space. In 2D, the simplest scenario corresponds to the pair of points. As followed from Definition 2, the point does not have any dimensional attributes. Thus, the proximity defines the distance between the points. In the case of an object being a line segment, its representation considers the set of points that belong to it. The proximity in terms of HD (Definition 22) computes the minimum distance from the given point to one of the points belonging to the line segment [117]. An arbitrary shape in 2D can be the set of its points from the interior or the contour. Similarly to the line segment, the proximity is defined using HD.

This chapter introduces the Elliptic Line Voronoi Diagram (ELVD), where the proximity is defined using CED, and overviews the classical approaches: the Point Voronoi Diagram (PVD) and the Line Voronoi Diagram (LVD). In essence, ELVD is extracted from CEF, similarly to the DT-based approaches for VD. Here, the main goal is to analyze the geometric properties of ELVD, particularly, on an example of a triangle. The experimental examination of ELVD, LVD and PVD aims at showing the applicability of the above approaches by comparison of their results under various conditions.

6.1 Voronoi Diagram (VD)

Before discussing the theory behind the Voronoi Diagram (VD) in 2D, consider the formal definitions of the notions that are used throughout the related sections.

Definition 46 (Site)**.** *Consider the finite set $\mathcal{S}$ of N objects (for example, points or line segments). Any point $P \in \mathbb{R}^2$ is associated with the closest object from $\mathcal{S}$, such that the entire space is divided into disjoint regions. The elements in $\mathcal{S}$ are called sites.*

Definition 47 (Voronoi region)**.** *Consider the site set* $\mathcal{S} = \{s_1, s_2, \ldots, s_N\}$*. A Voronoi region,* $\mathcal{VR}_{s_i}$*, is the set of points that are at least as close to the site* s_i *as to any other site* s_j *with regard to metric* d_x*:*

$$\underset{\substack{i\in[1,\ldots,N];\\ s_i\in\mathcal{S}}}{\mathcal{VR}_{s_i}} = \{P \in \mathbb{R}^2 : \mathsf{d}_\mathsf{x}(P, s_i) \leq \mathsf{d}_\mathsf{x}(P, s_j) \mid s_j \in \mathcal{S}, i \neq j \in [1, \ldots, N]\} \quad (6.1)$$

Definition 48 (Voronoi edge)**.** *Consider the finite site set* $\mathcal{S}$*. The set of points, which are equally distant from two sites with regard to metric* d_x*, form the Voronoi edge.*

Definition 49 (Voronoi vertex)**.** *The Voronoi vertex is an intersection point of at least three Voronoi edges.*

Definition 50 (Voronoi Diagram)**.** *The Voronoi Diagram (VD) defined on the finite set of sites* $\mathcal{S}$ *is a union of corresponding Voronoi edges and vertices:*

$$\mathcal{VD}_\mathcal{S} = \bigcup_{\substack{i\neq j,\\ s_i,s_j\in\mathcal{S}}} \mathcal{VR}_{s_i} \cap \mathcal{VR}_{s_j}, \quad (6.2)$$

where $\mathcal{VR}_{s_i}$ *and* $\mathcal{VR}_{s_j}$ *denote the Voronoi regions of the sites* s_i *and* s_j *correspondingly.*

The VD example is illustrated in Figure 6.1. It contains the set of six sites shown as the red points. The corresponding Voronoi regions (one of them is shown as a filled rhombus) are bounded by the Voronoi edges (shown as green line segments). The Voronoi vertices are marked as orange squares.

Definitions 46 to 50 are the same for various VD types discussed below. The only difference is in the particular metric instead of d_x.

6.1.1 Point Voronoi Diagram (PVD)

Depending on the type of objects in the site set, the variety of VDs is identified. This thesis focuses on two of them, which are directly related to the proposed methodology: the Point Voronoi Diagram (PVD) and the Line Voronoi Diagram (LVD).

Definition 51 (Point Voronoi Diagram)**.** *Consider a finite site set of* N *points. VD computed from such a set using Euclidean metric,* d_2*, is called Point Voronoi Diagram (PVD). PVD tessellates the space into* N *convex Voronoi regions.*

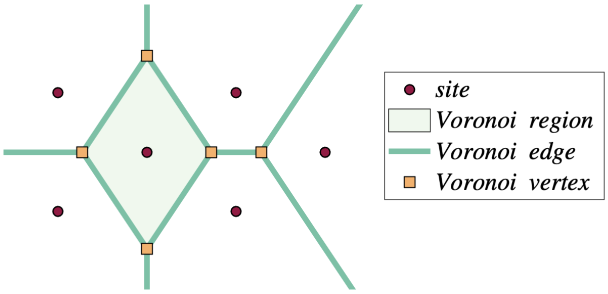

Figure 6.1: The VD example

Figure 6.2a illustrates the example of PVD. The site set contains six red points, whereas the Voronoi edges are shown as the green line segments.

Property 27 (Voronoi edges in PVD)**.** *Voronoi edges are perpendicular bisectors between each pair of points in the site set. Voronoi edges can be half-infinite [49].*

6.1.2 Line Voronoi Diagram (LVD)

In computational geometry, the majority of geometrical scenarios accept the polygonal representation of the objects [14]. A shape contour is approximated by a polygon, which, in turn, is a set of line segments.

Definition 52 (Line Voronoi Diagram)**.** *Consider a finite site set containing points and line segments. VD constructed from such a set using HD,* d_{HD}*, is called Line Voronoi Diagram (LVD). LVD tessellates the space into* N *Voronoi regions.*

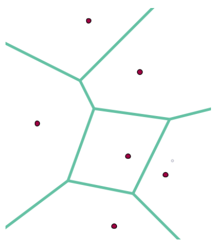

(a) PVD

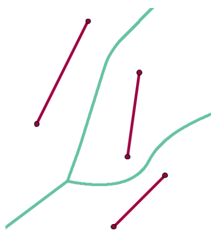

(b) LVD

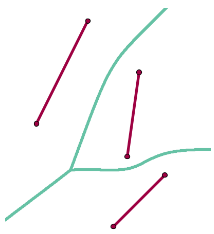

(c) ELVD

Figure 6.2: Various types of VD

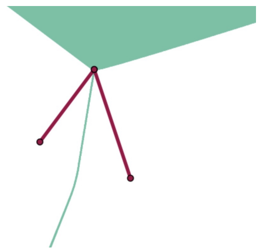

Figure 6.3: The example of LVD containing an area

The example of LVD is provided in Figure 6.2b. The site set contains three non-intersecting line segments shown in red. The Voronoi edges are the green curves.

Property 28 (LVD Voronoi edge between two line segments sharing an endpoint)**.** *In LVD, a Voronoi edge between two line segments sharing an endpoint contains an area [13].*

Property 28 highlights the ambiguity of the representation: an area of points corresponds to multiple sites (Figure 6.3). One solution is to remove the common endpoint [13].

Definition 53 (Reflex angle)**.** *An angle between* $180°$ *to* $360°$ *is called reflex.*

Property 29 (Number of Voronoi vertices and edges in VD of a closed polygon)**.** *VD of a closed polygon with* N *edges and* M *reflex vertices contains at most* $N + M - 2$ *Voronoi vertices and* $2(N + M) - 3$ *Voronoi edges [103].*

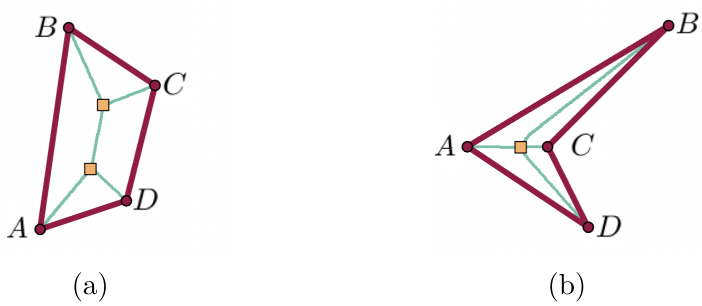

Figure 6.4: Examples of LVD for closed polygons (red). The green curves show the Voronoi edges and the orange squares mark the Voronoi vertices

Figure 6.4 illustrates two closed polygons with four edges ($N = 4$). The Voronoi edges are shown as green curves and the Voronoi vertices are orange squares. In Figure 6.4a, there are no reflex angles ($M = 0$), two Voronoi vertices and five Voronoi edges. There is no contradiction to Property 29, since the maximum number of Voronoi edges is $2(N + M) - 3 = 5$ and of Voronoi vertices is $N + M - 2 = 2$. In Figure 6.4b, there is one reflex angle $\widehat{BCD}$ ($M = 1$), one Voronoi vertex and four Voronoi edges. There is again no contradiction to Property 29, since the maximum number of Voronoi edges is $2(N + M) - 3 = 7$ and of Voronoi vertices is $N + M - 2 = 3$.

6.1.3 Elliptic Line Voronoi Diagram (ELVD)

In this thesis, it is proposed to use CED (Section 4.1.2) as a proximity measure. It enables having an alternative representation of a line segment by the pair of its endpoints. This implies a space tessellation which in special cases degenerates to PVD or LVD.

Definition 54 (Elliptic Line Voronoi Diagram)**.** *Let a site set contain line segments and points considered degenerated line segments. Each line segment is defined by the pair of its endpoints. VD constructed from such a set using CED, d_{CED}, is called Elliptic Line Voronoi Diagram (ELVD). ELVD tessellates the space into N Voronoi regions.*

An example of ELVD is shown in Figure 6.2c. The site set has three non-intersecting line segments of various lengths.

To gain understanding about the geometric properties of ELVD, take a closer look at a simplest closed polygon - a triangle. Langer [69] found the reference to an intersection point of Voronoi edges in ELVD of a triangle as the Equal Detour Point (EDP), or the inner Soddy circle center [51].

Definition 55 (Equal Detour Point)**.** *Imagine a triangle and a detour when moving from one of its vertices to another through an inner point P. The point P is referred to as the Equal Detour Point (EDP), if for each pair of triangle vertices the difference between the detour and the length of the corresponding side is the same.*

Property 30 (ELVD and the Equal Detour Point)**.** *In ELVD of the triangle, the Voronoi edges passing through its vertices intersect at exactly one point in its interior. In the literature, this point is referred to as the Equal Detour Point (EDP) [200] (Figure 6.5).*

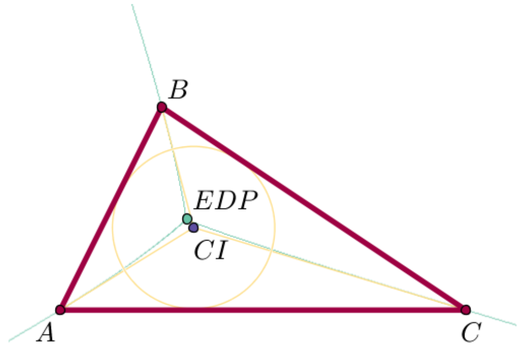

Figure 6.5: Equal Detour Point (EDP) and Center of the Incircle (CI)

Remark 1. EDP is not on the Euler line but the Soddy line [137].

Remark 2. EDP is always inside the triangle. It stems from the fact that the Voronoi edges are hyperbola branches, which intersect their transverse axes at the points between the triangle vertices.

Property 31 (EDP in ELVD of the degenerated triangle)**.** *In ELVD of the degenerated triangle, where two points A and B coincide, EDP is located at the point A (or B).*

Proof. The proof considers Property 30 and (4.5). Let A coincide with B, and EDP be located at P. Then, at the point P, the CED values for $\overline{AB}$ and $\overline{AC}$ are identical:

$$\mathsf{d}_2(A,P) + \mathsf{d}_2(B,P) - \mathsf{d}_2(A,B) = \mathsf{d}_2(C,P) + \mathsf{d}_2(A,P) - \mathsf{d}_2(A,C) \quad (6.3)$$

Simplification of (6.3) by removing identical terms and substituting $\mathsf{d}_2(A,C)$ with $\mathsf{d}_2(B,C)$ (because of their equality) leads to:

$$\mathsf{d}_2(B,P) + \mathsf{d}_2(B,C) = \mathsf{d}_2(C,P) \quad (6.4)$$

(6.4) holds true only when P coincides with A and B. □

Definition 56 (Soddy circle)**.** *Imagine ELVD of a triangle (Figure 6.6). The Voronoi edges pass through its vertices A, B, and C and intersect the edges $\overline{AB}$, $\overline{BC}$, and $\overline{CA}$ at the points K, L, and M correspondingly. Assume $r_A = \mathsf{d}_2(A,M) = \mathsf{d}_2(A,K)$, $r_B = \mathsf{d}_2(B,L) = \mathsf{d}_2(B,K)$, and $r_C = \mathsf{d}_2(C,L) =$*

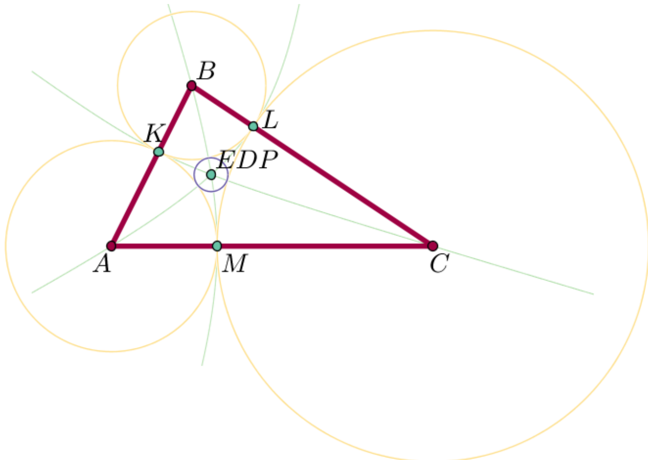

Figure 6.6: ELVD of the triangle and the inner Soddy circle

$\mathsf{d}_2(C, M)$. *Let* A, B, *and* C *be the centers of tangent circles with the radii* r_A, r_B, *and* r_C*:* $\mathsf{C}(A; r_A)$, $\mathsf{C}(B; r_B)$, *and* $\mathsf{C}(C; r_C)$ *respectively. The circle with the center at EDP that is tangent to* $\mathsf{C}(A; r_A)$, $\mathsf{C}(B; r_B)$, *and* $\mathsf{C}(C; r_C)$ *is called the inner Soddy circle [185].*

Property 32 (ELVD distance value at EDP)**.** *In ELVD of triangle, the distance value at EDP, equals the diameter of the inner Soddy circle.*

Proof. According to Property 30, the Voronoi edges intersect at EDP. As followed from Definition 56, the inner Soddy circle has its center at EDP and is tangent to the circles $\mathsf{C}(A; r_A)$, $\mathsf{C}(B; r_B)$, and $\mathsf{C}(C; r_C)$ (Figure 6.6). The distance between the centers of tangent circles equals the sum of their radii [46]. So, it is possible to rewrite (4.5) with regard to the radii and one of the triangle edges, for instance, $\overline{CA}$:

$$\mathsf{d}_{CED}(\text{EDP}, \overline{CA}) = \mathsf{d}_2(\text{EDP}, A) + \mathsf{d}_2(\text{EDP}, C) - \mathsf{d}_2(C, A) \tag{6.5}$$

$$\mathsf{d}_{CED}(\text{EDP}, \overline{CA}) = (r_A + r_S) + (r_C + r_S) - (r_A + r_C) = 2r_S \tag{6.6}$$

As can be observed from the above equations, the distance value at the center of the inner Soddy circle equals its diameter. □

Similarly, Dergiades [51] showed that the extra distance travelled through EDP equals the diameter of the Soddy circle.

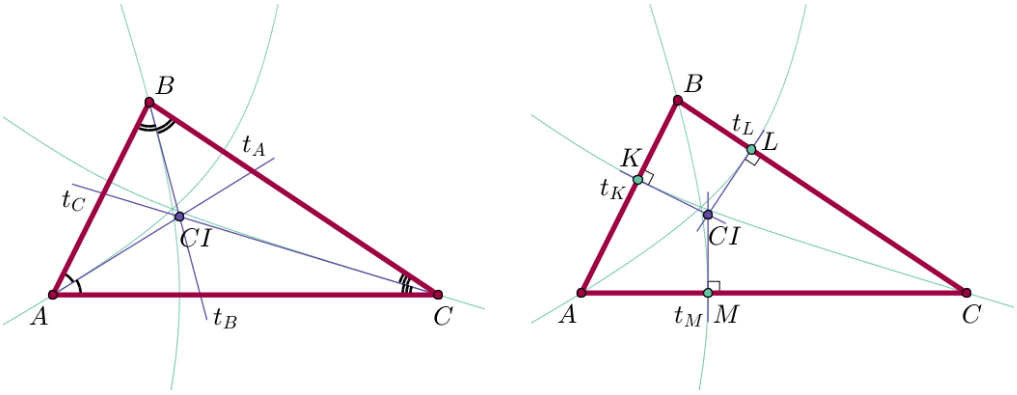

(a) tangents $t_A,\ t_B,\ t_C$ intersect at CI (b) tangents $t_K,\ t_L,\ t_M$ intersect at CI

Figure 6.7: ELVD of the triangle $\triangle ABC$ and the Center of the Incircle (CI)

Property 33 (ELVD and the Center of the Incircle)**.** *In ELVD of the triangle, the six tangents to the Voronoi edges at the points $A,\ B,\ C,\ K,\ L$, and M intersect at exactly one point in the triangle interior, called Center of the Incircle (CI) (Figure 6.5).*

Proof. First, consider the proof for the tangents to Voronoi edges, $t_A,\ t_B$, and t_C, taken at the points $A,\ B$, and C. According to the hyperbola property [108], tangent to its branch at some point $P \in \mathbb{R}^2$ is an angle bisector between the lines connecting P and its focal points. In relation to $\triangle ABC$, consider the hyperbola branch that passes through the point A and has B and C as the focal points. The tangent t_A to this hyperbola branch at the point A bisects the angle $\widehat{BAC}$ (Figure 6.7a). Similarly, t_B and t_C bisect the angles $\widehat{ABC}$ and $\widehat{BCA}$. For the triangle, the angle bisectors intersect at CI [46]. It implies that $t_A,\ t_B$, and t_C intersect at CI.

Second, follow the proof for the tangents to the Voronoi edges, $t_K,\ t_L$, and t_M, taken at points $K,\ L$, and M. Consider the hyperbola with the focal points A and C. One of its branches passes through B and intersects the triangle edge $\overline{CA}$ at the point M. According to Property 3, the tangent t_M at M is perpendicular to $\overline{CA}$ (Figure 6.7b). Similar reasoning can be applied to the remaining points K and L:

$$t_K \perp \overline{AB},\ t_L \perp \overline{BC},\ t_M \perp \overline{CA} \tag{6.7}$$

The point M belongs to the Voronoi edge which is defined by the hyperbola branch passing through B, hence, with regard to (4.11):

$$\mathsf{d}_2(A, M) - \mathsf{d}_2(M, C) = \mathsf{d}_2(A, B) - \mathsf{d}_2(B, C) \tag{6.8}$$

The length of the triangle edge $\overline{CA}$ can be defined by the sum:

$$\mathsf{d}_2(A, M) + \mathsf{d}_2(M, C) = \mathsf{d}_2(C, A) \tag{6.9}$$

From (6.8) and (6.9) it is possible to derive:

$$\mathsf{d}_2(A, M) = \frac{\mathsf{d}_2(C, A) - \mathsf{d}_2(B, C) + \mathsf{d}_2(A, B)}{2} \tag{6.10}$$

Applying similar reasoning to the point K leads to:

$$\begin{cases} \mathsf{d}_2(A, K) + \mathsf{d}_2(K, B) = \mathsf{d}_2(A, B) \\ \mathsf{d}_2(A, K) - \mathsf{d}_2(K, B) = \mathsf{d}_2(C, A) - \mathsf{d}_2(B, C) \end{cases} \tag{6.11}$$

$$\implies \mathsf{d}_2(A, K) = \frac{\mathsf{d}_2(C, A) - \mathsf{d}_2(B, C) + \mathsf{d}_2(A, B)}{2} \tag{6.12}$$

As can be observed, $\mathsf{d}_2(A, M) = \mathsf{d}_2(A, K)$. Analogically, it is possible to derive the equalities for the remaining line segments. As a result:

$$\mathsf{d}_2(K, B) = \mathsf{d}_2(B, L), \; \mathsf{d}_2(L, C) = \mathsf{d}_2(C, M) \tag{6.13}$$

Imagine a circle that touches $\overline{AK}$ and $\overline{AM}$ at the points K and M correspondingly and has a center at O. According to the property of tangents to circle [212], they are perpendicular to the radius at the point of contact. Hence, t_K intersects t_M at O, and $\mathsf{d}_2(O, K)$=$\mathsf{d}_2(O, M)$. Under the same property, $\overline{OA}$ bisects the angle $\widehat{BAC}$. For a circle touching $\overline{BK}$ and $\overline{BL}$ with the center at O': $O'B$ bisects the angle $\widehat{ABC}$, t_K intersects t_L at O', and $\mathsf{d}_2(O', K)$=$\mathsf{d}_2(O', L)$. For a circle touching $\overline{CL}$ and $\overline{CM}$ with the center at O'': $O''C$ bisects the angle $\widehat{BCA}$, t_M intersects t_L at O'', and $\mathsf{d}_2(O'', M)$=$\mathsf{d}_2(O'', L)$.

Let O and O' be two distinct points. If $\mathsf{d}_2(O', K)$<$\mathsf{d}_2(O, K)$, then O'' is located such that $\mathsf{d}_2(O'', L)$<$\mathsf{d}_2(O'', M)$. If $\mathsf{d}_2(O', K)$>$\mathsf{d}_2(O, K)$, then $\mathsf{d}_2(O'', L)$>$\mathsf{d}_2(O'', M)$. Both statements contradict the equality of $\mathsf{d}_2(O'', M)$ and $\mathsf{d}_2(O'', L)$. Thus, points O and O' coincide. In the same manner, it is possible to show that O' coincides with O''. So, all three tangents, t_K, t_M, and t_L intersect at the same point $O \equiv O' \equiv O''$. Eventually, this point is also an intersection of the bisectors OA, $O'B$, and $O''C$. The bisectors in a triangle intersect at CI [46]. It implies that t_K, t_M, and t_L intersect at CI. □

6.2 Comparison between PVD, LVD, and ELVD

Several factors affect the space tessellation. On one side, it is the distance metric. On the other side, it is the type of objects in the site set (for instance, points and line segments), their relative position, and the difference in size.

6.2.1 Distance Metric

By definition, PVD and LVD rely on Euclidean distance and HD, whereas ELVD uses CED. A well-known problem of VD is to find a trade-off between tessellation precision and computational costs [133, 161]. A size of a site set, or a discretization level of input shape, has a direct influence on costs and efficiency of an approach. Especially, for GPU-methods. In contrast, ELVD does not depend on a sampling of line segments that form a polygonal shape, since it takes only a pair of endpoints.

6.2.2 Types of Objects in the Site Set

Voronoi edges in PVD are bisectors, in LVD – parabolic arcs, line segments, and rays [135], in ELVD – a multifocal hyperbola branch that, in special cases, is a bisector or a hyperbola branch (Section 4.2.1). Here, VD and ELVD are compared using various relations of two objects (except for coincidence). A pair of points can be arbitrarily placed on a plane. A point can be on a line segment or not. Line segments can overlap, intersect, or not intersect.

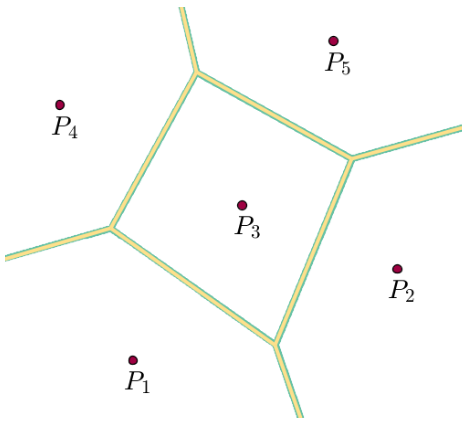

Figure 6.8: Identical PVD (yellow) and ELVD (green) from the set of points

Point and Point

When a site set contains only points, ELVD produces the same results as PVD (Figure 6.8). Voronoi edges are bisectors.

Point and Line Segment

ELVD separates a point and a line segment with a multifocal hyperbola branch, or a higher-order curve (Figure 6.9). Depending on the distance between P_3 and $\overline{P_1P_2}$ and a line segment length, a Voronoi edge changes visibly (Figures 6.9a and 6.9b). If a point belongs to a line segment, then LVD contains a normal to the line segment, and there is no tessellation in ELVD (Property 22).

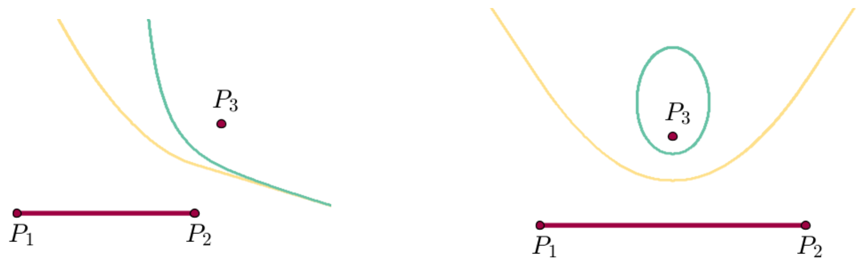

(a) $\mathsf{d}_2(P_1, P_2) \neq \mathsf{d}_2(P_2, P_3)$

(b) $\mathsf{d}_2(P_1, P_2) = \mathsf{d}_2(P_2, P_3)$

Figure 6.9: LVD (yellow) and ELVD (green) from a point and a line segment

Line Segments that Overlap Each Other

There are two possible scenarios: (1) $\overline{P_1P_2}$ and $\overline{P_3P_4}$ have a common line segment ($\overline{P_3P_2}$ in Figure 6.10a), (2) $\overline{P_3P_4}$ is a part of $\overline{P_1P_2}$ (Figure 6.10b). The disadvantage of LVD in both cases: it contains an area that creates an ambiguity. In ELVD, in the first case, a Voronoi edge is a multifocal hyperbola branch. In the second case, when $\overline{P_1P_2}$ encloses $\overline{P_3P_4}$, ELVD has no tessellation of space (Property 22).

Line Segments that Intersect Each Other

There are multiple ways to intersect line segments. An intersection point can be a common endpoint. If line segments have different lengths (Figure 6.11a), ELVD has a hyperbola branch (shown in green). If line segments have an

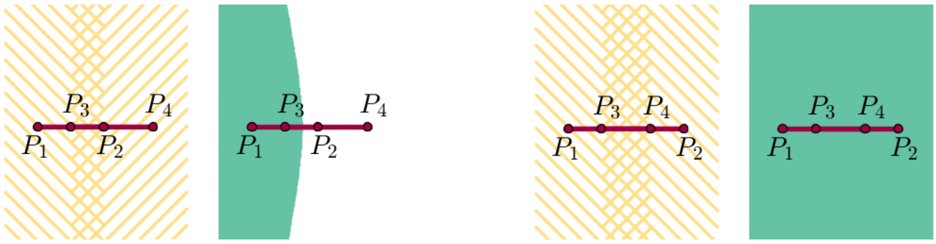

(a) $P_3 \in \overline{P_1P_2}$, $P_2 \in \overline{P_3P_4}$ (b) $\overline{P_3P_4} \in \overline{P_1P_2}$

Figure 6.10: Examples of Voronoi regions corresponding to LVD (yellow, left) and ELVD (green, right) generated from a pair of overlapping line segments

(a) $\mathsf{d}_2(P_1, P_2)<\mathsf{d}_2(P_2, P_3)$ (b) $\mathsf{d}_2(P_1, P_2)=\mathsf{d}_2(P_2, P_3)$

Figure 6.11: LVD (yellow) and ELVD (green) of the line segments sharing an endpoint

equal length (Figure 6.11b), ELVD contains a bisector passing through a common endpoint (P_2). Note, in this scenario, LVD contains an area which is rather a disadvantage for a representation. It means that a set of points have a non-unique mapping to sites. In relation to classification problems, such points are equally likely associated with more than one class.

The intersection point can split line segments into parts. If these parts have equal length (Figure 6.12a), LVD and ELVD create an identical tessellation. Otherwise, ELVD is a multifocal hyperbola that varies depending on relative size of line segments and an intersection point position (Figures 6.12b-6.12f). In special cases, such a Voronoi edge converges into a closed curve around the shortest parts. Observe the corresponding Voronoi regions in Figures 6.12b to 6.12d and 6.12f.

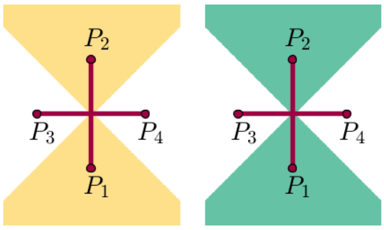

(a) $\mathsf{d}_2(P_1, P_2) = \mathsf{d}_2(P_3, P_4)$, cross at the center

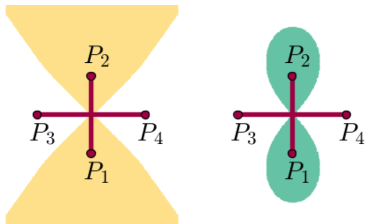

(b) $\mathsf{d}_2(P_1, P_2) < \mathsf{d}_2(P_3, P_4)$, cross at the center

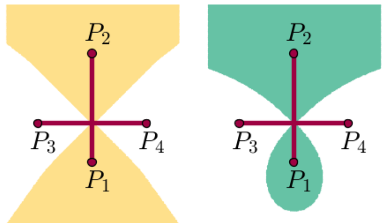

(c) $\mathsf{d}_2(P_1, O) < \mathsf{d}_2(P_2, O)$, where O is an intersection point; $\mathsf{d}_2(P_1, P_2) = \mathsf{d}_2(P_3, P_4)$

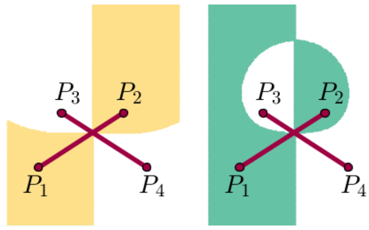

(d) $\mathsf{d}_2(P_1, P_2) = \mathsf{d}_2(P_3, P_4)$, cross not at a center

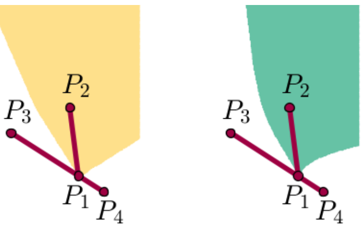

(e) $\mathsf{d}_2(P_1, P_2) < \mathsf{d}_2(P_3, P_4)$, $P_1 \in \overline{P_3 P_4}$

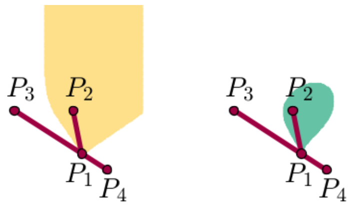

(f) $\mathsf{d}_2(P_1, P_2) \ll \mathsf{d}_2(P_3, P_4)$, $P_1 \in \overline{P_3 P_4}$

Figure 6.12: Examples of Voronoi regions corresponding to LVD (yellow, left) and ELVD (green, right) generated from a pair of intersecting line segments

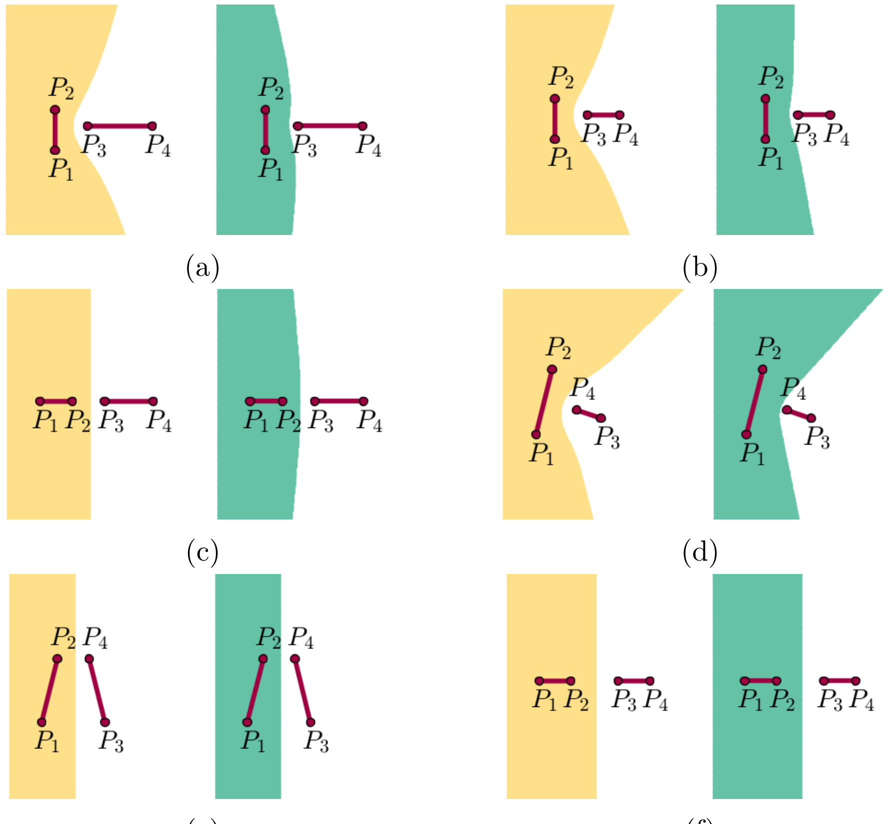

Figure 6.13: Examples of Voronoi regions corresponding to LVD (yellow, left) and ELVD (green, right) generated from a pair of non-intersecting line segments

Line Segments that do not Intersect

Consider that line segments do not intersect each other (Figure 6.13). A Voronoi edge in ELVD is a multifocal hyperbola branch that is shifted towards the shorter line segment. The equality of both representations happens when both line segments have a same length and are mirror-symmetric to each other with regard to some axis (Figures 6.13e and 6.13f). This axis is a Voronoi edge, which is a perpendicular bisector with regard to a closest pair of focal points connecting the line segments. For example, in Figure 6.13e the Voronoi edge is perpendicular to $\overline{P_2P_4}$ and $\overline{P_1P_3}$, and in Figures 6.13f – to $\overline{P_2P_3}$.

	VD	ELVD
Scope	• any 2D shape expressed by a set of points or line segments • extension to higher dimensions • identical representations for point sites	
Uniqueness	unique for a site set	
	Voronoi edge might contain area	Voronoi edge is always a curve
Invariance	equivariant to rotation, translation, and scaling	
Stability	every element affects the representation	stable in the cases satisfying Property 22
Accuracy	double-precision floating-point	$\frac{3\sqrt{2}}{2}$ pixel_edge_length
Efficiency	• Sequential:	
	$O(NlogN)$ [64, 210]	$O(N \times W \times H)$ [100]
	• Parallel:	
	$O(N)$ [191]	$O(N)$ [100]
Abstraction	enables hierarchical representation	

Table 6.1: Evaluation of the representations VD and ELVD

6.3 Discussion

So far, ELVD was empirically compared to VD according to various types of input data. Such a visual inspection provides an intuitive understanding of geometrical differences between the approaches. This section discusses ELVD and VD according to the proposed evaluation criteria for shape representation. The results are summarized in Table 6.1.

Scope

Regarding space tessellation in 2D, the observed approaches do not have algorithmic limitations and can be extended to 3D. Particularly, generalization of PVD to higher dimensions preserves the convexity of the Voronoi regions while losing linearity in size [13]. This stays true for ELVD of the point sites.

Uniqueness

ELVD, PVD, and LVD provide a unique partitioning of space that depends on the type and location of objects in the input site set. It is caused by the Euclidean metric used in these approaches. As noted in Sections 6.2.2-*Line Segments that Overlap Each Other* and *Line Segments that Intersect Each Other*, LVD may contain an area of points that are associated with multiple sites (refer to Figures 6.10 and 6.11). It is a disadvantage for a representation since creating a non-unique association with the sites. One way to solve the problem is to add a preprocessing step that resolves the ambiguity. For the line segments sharing an endpoint it is a common practice to make the line segments disjoint [13]. In the case of overlapping line segments, the ambiguity can be mitigated by restructuring the common region. ELVD does not require a preliminary decomposition.

Invariance

Since VD and ELVD use the Euclidean distance as a proximity measure, the resultant representation is equivariant to translation and rotation [148]. Applying the normalization strategy leads to scale invariance [140].

Stability

This property is interpreted as an ability to preserve space tessellation under changes of input sites. Especially in the digital domain, it relates to inevitable numerical errors that lead to a different position of sites, their size, or structure [153]. As noted in [11], VD is not stable under the continuous motion of sites. Indeed, the small change in the sites implies the small change in VD [153]. In ELVD, the representation is stable in the cases fulfilling Property 22. Otherwise, it is sensitive to each element in the site set.

Accuracy

Computing VD with algorithms using exact arithmetic is a cumbersome and expensive procedure [211]. Practical implementations rely on fixed-precision arithmetic, like single- or double-precision floating-point [76, 85, 86, 173]. Strzodka et al. [191] propose a GPU implementation, where, VD is computed with a single-precision floating point accuracy. To compute ELVD, it is proposed to apply $\mathrm{CEF}_{\mathrm{DT}_2}$ algorithms for computing separating curves:

Algorithm 5.2 and method of Langer [100]. In this case, the maximum error equals $\frac{3\sqrt{2}}{2}$ pixel_edge_length (Section 5.6-*Accuracy*).

Efficiency

There is a variety of methods creating VD [13]. From the complexity point, PVD requires $O(NlogN)$ time in the worst case [135], where N denotes the number of point-sites. So the efficient solutions are assumed to fulfil this condition. The sweepline algorithm, proposed by Fortune [49, 64], takes $O(NlogN)$ time and $O(N)$ space for computing PVD and LVD. The algorithm is sequential with interdependencies between its parts. It makes further optimization with parallel computation challenging [142]. Yap [210] proposed a divide & conquer approach for simple curve segments with $O(NlogN)$ complexity. It is a powerful algorithmic concept considering parallel VD computation for subsets of sites and merging the results together. Nevertheless, the implementation is not straightforward: the improper split into subsets causes difficulties while merging [4]. Another conceptually valuable method is based on incremental insertion [82, 193]. Here, the sites are added one by one to sequentially update VD. Although, the average complexity reaches $O(N)$, in the worst case scenario it equals $O(N^2)$.

A parallel computation of VD is proposed by Strzodka et al. [191]. The algorithm, first, assigns to each pixel the numeric label of the nearest site. Second, it thresholds the derivative applied to pixel labels to obtain VD. This method is suited for GPU processing, and has a linear complexity. A comparable approach proposed by Langer [100] also propagates the site labels. In contrast to [191], it uses the precomputed distance fields to accelerate processing. In addition, ELVD reduces the computational costs since there is no need in finding the proximity to all points belonging to the line segment.

6.4 Summary

This chapter further analyzed the distance field based on confocal ellipses from the VD perspective. The systematic analysis of all possible relations between the pairs of points and line segments provided an empirical comparison of ELVD and VD. In short, ELVD generalizes VD and degenerates to it in the special scenarios, like the site set containing only points or equally long line segments sharing an endpoint. From the geometric structure perspective, PVD and LVD are formed by parabolic arcs and straight lines. This property enables decomposing higher-order curves into a set of primitive components which are easy to compute. The Voronoi edge in ELVD could be a straight line, a hyperbola branch, or a multifocal hyperbola branch (higher-order curve). A possibility of decomposing such a higher-order curve into primitive components could be a potential question for future research. It is important to note that LVD of line segments sharing an endpoint requires a preprocessing step to avoid having an area in the structure. This is not the case for ELVD. The analysis of the ELVD properties in the case of a triangle enriches the semantic understanding of the proposed representation. Generalization of these properties to an arbitrary polygonal shape is yet an open question.

CHAPTER 7

Elliptic Line Voronoi Skeleton

This chapter is based on the following publications:

Aysylu Gabdulkhakova, Maximilian Langer, Bernhard W. Langer, Walter G. Kropatsch:
Line Voronoi Diagrams Using Elliptical Distances. In Proceedings of the Joint IAPR International Workshop on Structural, Syntactic, and Statistical Pattern Recognition, pages 258–267, 2018 [69]

A skeleton is a compact and effective representation encoding a shape by a subset of its inner points. The desirable characteristics include equivariance to transformations (rotation, translation, and scaling), topology consistency, connectivity, and reconstruction. In addition, it can provide equivariance to bending, elongation, decomposition, widening, and warping. Thus, the skeleton is used in a variety of application domains, such as image compression and retrieval, character recognition, path planning, and object recognition [11].

When applied to shape representation, a 2D skeleton is primarily associated with a set of 1D curves and the notion of a medial axis. The existing algorithms for computing the skeleton are generally classified into digital and continuous [162]. The continuous methods approximate the shape boundary by a curve or a polygon, work with real point coordinates, and rely on analytical computation. A group of methods evolves from VD [133], which preserves topological as well as geometrical information. The Voronoi Skeleton (VS) is a VD of the site set forming the shape boundary [133]. VS can be additionally modified by applying specific pruning techniques [9,16,17,97,107,134,177,197], whose crucial property is in preserving the shape topology.

Alternatively, the skeleton can be obtained by the grassfire transform [28]. Consider a set of fire fronts that are uniformly propagated from the shape boundary towards the interior. Then, the skeleton is a set of quenching points where these fire fronts meet. This idea is reflected in a group of approaches based on the curve propagation principle [31, 165]. The points of the medial axis are located at certain singularities in, for example, flux field [181], distance field [88, 105], or potential field [2].

Digital approaches rest on geometrical and topological rules to extract the skeleton from a digital grid [162]. One group of methods, called *thinning*, performs an iterative erosion of pixels starting from the shape boundary using the predefined templates under geometrical and topological constraints [104, 128, 141, 163, 214]. Another group of approaches performs erosion on the distance field [31, 81, 165]. It has an advantageous computational efficiency since using DT and not having a need to perform repetitive image scans. The disadvantage lies in the difficulty of parallelizing such algorithms [161].

An important drawback of digital and continuous approaches is their noise sensitivity: small perturbations on the boundary cause spurious branches in the resultant skeleton. There are many ways to solve this problem, including the boundary smoothing, polygonal approximation of the shape, a hierarchy of skeletons, weighting of the seed points [17].

The Elliptic Line Voronoi Skeleton (ELVS) is a continuous approach evolved from ELVD. As opposed to VS, using CED as a metric leads to a non-medial representation of a shape approximated by the line segments. This chapter aims at exploring the geometrical properties of ELVS and compares them to the classical VS.

7.1 Voronoi Skeleton (VS)

The shape representation by means of medial loci was proposed by Blum [28]. It defines the local symmetries of object by the set of points equidistant to the shape boundary.

Definition 57 (Maximal circle). *A circle* $\mathsf{C}(O; r) \in \mathbb{R}^2$ *is maximal if it is not inside any other circle* $\mathsf{C}(O'; r') \in \mathbb{R}^2$.

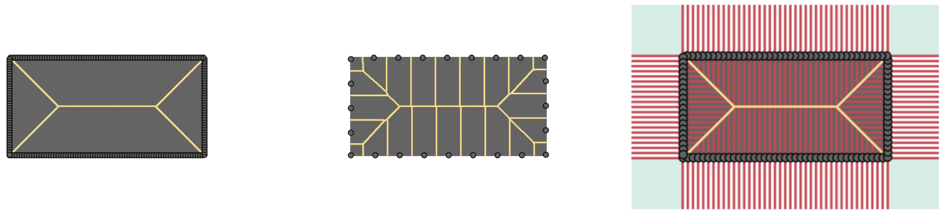

(a) medial axis (b) VS from 24 points (c) VS from infinitely many points

Figure 7.1: Discrepancy between a medial axis and VS extracted from PVD

Definition 58 (Medial axis)**.** *The medial axis of a shape in 2D is formed by the centers of maximal circles that are bitangent to the shape boundary and are entirely in its interior.*

The medial axis with the radius function of the maximal circles is called the Medial Axis Transform (MAT) [28]. MAT represents a 2D shape by the union of curves and arcs and enables reducing its dimensionality to a 1D set of points. MAT preserves symmetry and local thickness of shape and it is equivariant to rotation and translation. The union of circles, associated with each skeletal point, reconstructs the original shape [162] in the continuous space and covers the shape in the digital space [167].

The Voronoi Skeleton (VS) is computed as an intersection of the shape and VD. The shape boundary divides VS into *endoskeleton* (interior) and *exoskeleton* (background). The endoskeleton shows the internal structure, topology, and metrics of the shape, whereas the exoskeleton – the adjacency relation to the neighboring objects [133]. The discrepancy between the medial axis and VS depends on the boundary approximation [152] (Figure 7.1). Schmitt [170] proved that having an infinite number of points on the boundary leads to convergence in the limit of VS to the medial axis. Suppose, in Figure 7.1c, the boundary of the rectangle is expressed by infinitely many points (gray circles). The Voronoi regions of point-sites at the rectangle corners contain an area (green). For other point-sites, a Voronoi region is a ray that starts at the skeletal point and is orthogonal to the corresponding side of the rectangle [61]. For a convex polygon, Lee [103] showed that VS is identical to the medial axis (Figure 7.2a). If the polygon is non-convex, then the medial axis is a subset of VS (Figure 7.2b and 7.2c). The same holds true for the piecewise-linear/circular shape boundary. When the boundary is composed of free-form curves, generally, neither is a subset of the other [152].

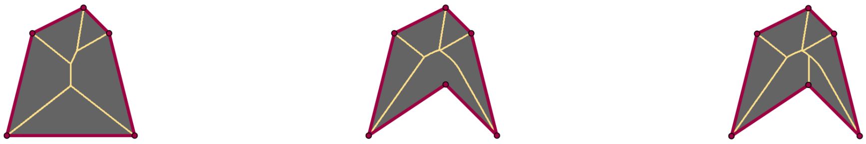

(a) medial axis equals VS (b) medial axis (c) VS

Figure 7.2: Discrepancy between a medial axis and VS extracted from LVD

7.2 Elliptic Line Voronoi Skeleton (ELVS)

Similarly to VS, the Elliptic Line Voronoi Skeleton (ELVS) is a subset of ELVD. As opposed to VS, the proposed representation is medial only in special cases.

Property 34 (Line segment length impact in ELVS)**.** *In ELVS, a site representing a long line segment pushes the Voronoi edges towards the smaller line segments.*

To illustrate this property intuitively, it is proposed to use the barycentric coordinates (Definition 6). Let the triangle $\triangle ABC$ have the side lengths a, b, and c (Figure 7.3). Its half-perimeter equals $s = \frac{1}{2}(a+b+c)$, whereas the area is computed by $\Delta = \sqrt{s(s-a)(s-b)(s-c)}$ [46]. According to Dergiades [51], the homogeneous barycentric coordinates of EDP are:

$$\begin{cases} m_A = a + \frac{\Delta}{s-a} \\ m_B = b + \frac{\Delta}{s-b} \\ m_C = c + \frac{\Delta}{s-c} \end{cases} \tag{7.1}$$

Consider the formula for the tangent of a half of an internal angle in a triangle [189]:

$$\begin{cases} \tan \frac{\hat{A}}{2} = \sqrt{\frac{(s-b)(s-c)}{s(s-a)}} \\ \tan \frac{\hat{B}}{2} = \sqrt{\frac{(s-a)(s-c)}{s(s-b)}} \\ \tan \frac{\hat{C}}{2} = \sqrt{\frac{(s-a)(s-b)}{s(s-c)}} \end{cases} \tag{7.2}$$

Then, (7.1) can be transformed by substituting the tangent formulas:

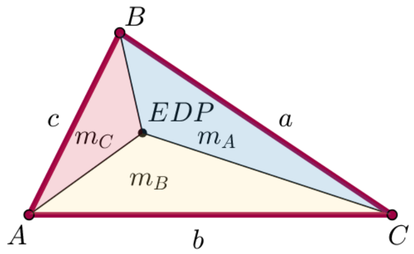

Figure 7.3: An interpretation of EDP using the barycentric coordinates

$$\begin{cases} m_A = a + s\tan\frac{\hat{A}}{2} \\ m_B = b + s\tan\frac{\hat{B}}{2} \\ m_C = c + s\tan\frac{\hat{C}}{2} \end{cases} \tag{7.3}$$

According to the triangle property [145], the shortest side is opposite to the smallest internal angle. The sum of all the internal angles of the triangle is 180° [145], so the half-angles range between 0° and 90°. The larger the internal angle – the larger the tangent of the angle. Applying the above statements to (7.3): the acute angle and the short length of the edge lead to a small value in the barycentric coordinates. Consider the examples in Figure 7.4. According to Property 2, the areas of the subtriangles are proportional to the barycentric coordinates of the point. In the case of acute angle at the vertex B (Figure 7.4a), m_B will have the smallest value among m_A and m_C. As a result, the subtriangle formed by EDP, A, and C has the smallest area. The opposite effect is observed when obtuse angle is at the vertex B (Figure 7.4b).

Corollary 1 (Angle priority in ELVS)**.** *An acute angle between the connected sites pushes the Voronoi vertex away from their common point. An obtuse angle – towards their common point.*

7.3 Comparison between VS and ELVS

VS, in its classical sense, is a medial representation whose points are visually in the middle of the shape. As followed from Property 34 and Corollary 1, ELVS implicitly prioritizes long line segments and acute angles (Figure 7.5b). Consequently, for the equilateral polygon without self-intersections, ELVS is identical to VS (Figure 7.5a).

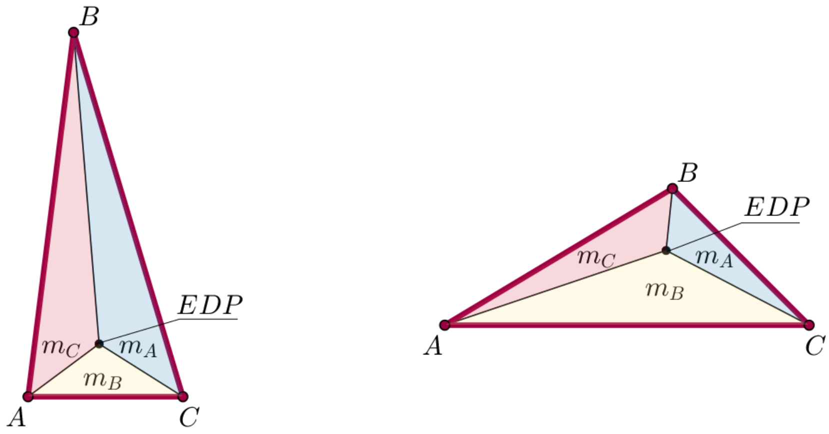

(a) acute (b) obtuse

Figure 7.4: Acute- and obtuse-angled triangles in the barycentric coordinates

From the geometrical point of view, VS is formed by the points having the same distance to at least two edges of the polygon. So, for the triangle, VS-exoskeleton contains only the curves that separate the nearest sides. It is not always the case for the ELVS-exoskeleton.

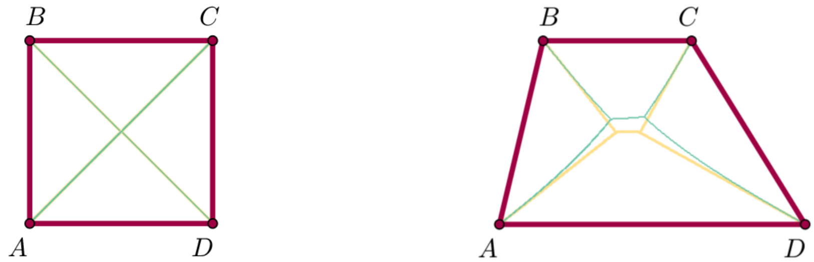

(a) square (b) trapezoid

Figure 7.5: Examples of VS (yellow) and ELVS (green) for convex polygons

Property 35. *In the obtuse-angled triangle the branches of ELVS passing through the vertices of the longest edge might cross each other twice: in endo- and exoskeleton.*

Proof. According to Sections 4.2.1-*Bisector* and *Hyperbola Branch*, in ELVS two line segments with a common endpoint are separated by a bisector or a hyperbola branch. Figure 7.6 illustrates various ELVS branches passing through the endpoints of $\overline{AC}$ (orange and blue curves). An area expresses Voronoi region of $\overline{AC}$. With regard to (4.5) and (6.1), the Voronoi region of $\overline{AC}$ satisfies:

$$\begin{cases} \mathsf{d}_2(\mathrm{A,P}){+}\mathsf{d}_2(\mathrm{C,P}){-}\mathsf{d}_2(\mathrm{A,C}){<}\ \mathsf{d}_2(\mathrm{A,P}){+}\mathsf{d}_2(\mathrm{B,P}){-}\mathsf{d}_2(\mathrm{A,B}) \\ \mathsf{d}_2(\mathrm{A,P}){+}\mathsf{d}_2(\mathrm{C,P}){-}\mathsf{d}_2(\mathrm{A,C}){<}\ \mathsf{d}_2(\mathrm{C,P}){+}\mathsf{d}_2(\mathrm{B,P}){-}\mathsf{d}_2(\mathrm{C,B}) \end{cases} \tag{7.4}$$

$$\begin{cases} \mathsf{d}_2(\mathrm{C,P}){-}\mathsf{d}_2(\mathrm{B,P}){<}\ \mathsf{d}_2(\mathrm{A,C}){-}\mathsf{d}_2(\mathrm{A,B}) \\ \mathsf{d}_2(\mathrm{A,P}){-}\mathsf{d}_2(\mathrm{B,P}){<}\ \mathsf{d}_2(\mathrm{A,C}){-}\mathsf{d}_2(\mathrm{C,B}) \end{cases} \tag{7.5}$$

It suffices to prove that only for the obtuse-angled triangle (Figure 7.6d), ELVS branches might intersect each other twice: in endo- and exoskeleton. To show that, consider all combinations of the side lengths in $\triangle ABC$ as compared to $\overline{AC}$.

1. all triangle sides, $\overline{AB}$, $\overline{BC}$, $\overline{AC}$, have an equal length

   If $\triangle ABC$ is an equilateral triangle, then the respective ELVS contains bisectors that intersect at CI [6]. Since the bisectors are lines, there is no possibility for them to intersect twice [77].

2. $\overline{AC}$ is either equal to $\overline{AB}$, or $\overline{BC}$

   Assume $\overline{AC}$ is equal to one of the remaining sides, for example, $\overline{AB}$. The ELVS branch passing through A is a bisector. The ELVS branch passing through C is a hyperbola branch with the foci at A and B. By definition, the hyperbola branch approaches the asymptotes. To intersect the hyperbola branch, thus, the asymptotes twice, one condition is to cross the line segment connecting the focal points ($\overline{AB}$) at the point belonging to $\overline{MB}$, where M is the middle of $\overline{AB}$. This is not possible since the bisector passes through A. So, there is only one intersection point between a line containing A and the hyperbola branch that passes through C.

The right sides in system of inequalities (7.5) contain the differences between the lengths of triangle sides. Here, the upper inequality defines the hyperbola branch passing through A, whereas the lower – through C. Depending on the sign of the difference, the resultant hyperbola branch is

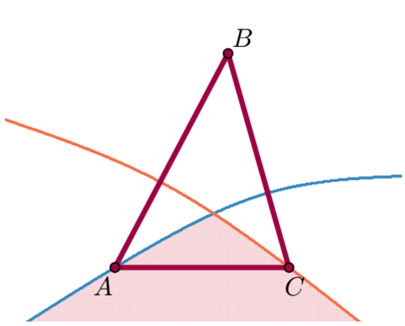

(a) $\mathsf{d}_2(A,C)<\mathsf{d}_2(A,B)$,
$\mathsf{d}_2(A,C)<\mathsf{d}_2(C,B)$

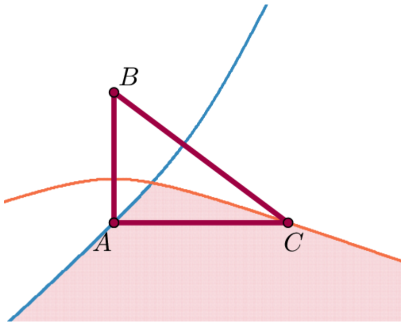

(b) $\mathsf{d}_2(A,C)>\mathsf{d}_2(A,B)$,
$\mathsf{d}_2(A,C)<\mathsf{d}_2(C,B)$

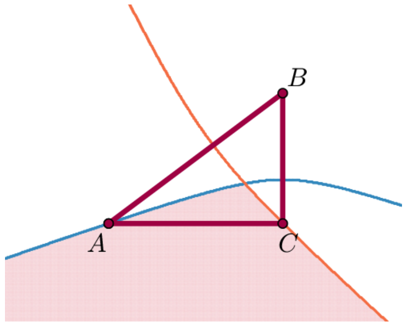

(c) $\mathsf{d}_2(A,C)<\mathsf{d}_2(A,B)$,
$\mathsf{d}_2(A,C)>\mathsf{d}_2(C,B)$

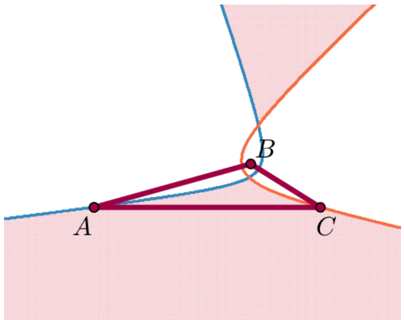

(d) $\mathsf{d}_2(A,C)>\mathsf{d}_2(A,B)$,
$\mathsf{d}_2(A,C)>\mathsf{d}_2(C,B)$

Figure 7.6: Voronoi edges in a triangle depending on the side lengths

directed upwards (for plus) or downwards (for minus). Consider now the remaining configurations of the side lengths by assigning the right sides in system of inequalities (7.5) to plus or minus.

3. $\overline{AB}$ and $\overline{BC}$ are longer than $\overline{AC}$ (Figure 7.6a), or:

$$\begin{cases} \mathsf{d}_2(\mathrm{C,P})-\mathsf{d}_2(\mathrm{B,P})<\text{“—”} \\ \mathsf{d}_2(\mathrm{A,P})-\mathsf{d}_2(\mathrm{B,P})<\text{“—”} \end{cases} \tag{7.6}$$

   Both hyperbola branches are directed downwards, leading to a single Voronoi region related to $\overline{AC}$. Consequently, ELVS contains two branches corresponding to $\overline{AC}$.

4. $\overline{AB}$ is shorter and $\overline{BC}$ is longer than $\overline{AC}$ (Figure 7.6b), or:

$$\begin{cases} \mathsf{d}_2(C,P) - \mathsf{d}_2(B,P) < \text{“+”} \\ \mathsf{d}_2(A,P) - \mathsf{d}_2(B,P) < \text{“—”} \end{cases} \tag{7.7}$$

The hyperbola branch passing through A is directed upwards, and the one passing through C – downwards. It makes it impossible to have more than one Voronoi region related to $\overline{AC}$.

5. $\overline{AB}$ is longer and $\overline{BC}$ is shorter than $\overline{AC}$ (Figure 7.6c), or:

$$\begin{cases} \mathsf{d}_2(C,P) - \mathsf{d}_2(B,P) < \text{“—”} \\ \mathsf{d}_2(A,P) - \mathsf{d}_2(B,P) < \text{“+”} \end{cases} \tag{7.8}$$

This case is symmetric to the previous: there is one Voronoi region related to $\overline{AC}$.

6. $\overline{AB}$ and $\overline{BC}$ are shorter than $\overline{AC}$ (Figure 7.6d), or:

$$\begin{cases} \mathsf{d}_2(C,P) - \mathsf{d}_2(B,P) < \text{“+”} \\ \mathsf{d}_2(A,P) - \mathsf{d}_2(B,P) < \text{“+”} \end{cases} \tag{7.9}$$

The hyperbola branches passing through A and C are directed upwards. Depending on the magnitude of the obtuse angle, these branches can intersect twice: in endo- and exoskeleton.

When $\triangle ABC$ is an isosceles triangle with $\overline{AB}$ being equal to $\overline{BC}$, the situation refers to one of the two cases above: 3. or 6.

□

7.4 Discussion

Despite a vast amount of literature on this topic, there is no universal definition or evaluation strategy for skeletons [162]. Thus, similar to the previous sections, VS and ELVS are compared with respect to the shape representation criteria. The results are summarized in Table 7.1.

	VS	ELVS
Scope	• any 2D shape expressed by a set of points or line segments • extension to higher dimensions • identical representations for point sites	
	medial representation	non-medial representation
Uniqueness	unique for a site set	
Invariance	equivariant to rotation, translation, and scaling	
Stability	every element affects the representation	stable in the cases satisfying Property 22
	improved by pruning, smoothing, and weighting [17, 134]	
Accuracy	double-precision floating-point	$\frac{3\sqrt{2}}{2}$ pixel_edge_length
Efficiency	• Sequential:	
	$O(NlogN)$ [90, 103]	$O(N \times W \times H)$ [100]
	• Parallel:	
	$O(N)$ [191]	$O(N)$ [100]
Abstraction	enables hierarchical representation	

Table 7.1: Evaluation of the representations VD and ELVD

Scope

Similar to VS, ELVS successfully represents any 2D object approximated by a set of line segments and points. As an example, consider a skeleton of an elephant shape from the MPEG-7 dataset [182] (Figure 7.8). The efficiency since computing fewer Voronoi regions comes at the price of skeleton accuracy. Infinitely many point sites lead to the medial axis [170], but cause a problem with spurious branches. Such branches reflect perturbations along the boundary rather than represent significant parts of the shape. They introduce complications to performance of recognition and matching [177]. Consider an example in Figure 7.7. Here, VS of a polygon with 170 line segments consists of spurious (blue) and non-spurious (yellow) branches. The skeletons of polygons with 50 line segments (Figures 7.8a and 7.8b) have less spurious branches than the skeletons generated from polygons containing 170

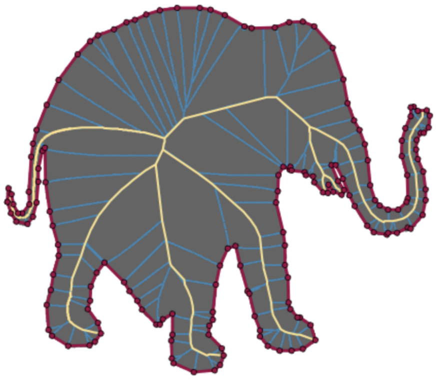

Figure 7.7: Example of spurious (blue) and non-spurious branches (yellow)

line segments (Figures 7.8c and 7.8d). On the other hand, the skeleton from 50 line segments is a worse approximation of a medial axis.

VS is a medial representation: its skeletal points are equally distant from the opposite borders of the shape. ELVS implicitly prioritizes long line segments. In Figure 7.8e, the polygonal approximation contains line segments of approximately similar length. So the discrepancy between VS and ELVS is comparably small. In the case of non-uniform sampling (Figure 7.8f), the shift between VS and ELVS is clearly stronger. Langer [100] analyzed the effect of varying density in polygons on ELVS: in fact, the strength of non-medial shift depends not only on the line segment length but also on the distance to the opposite line segment.

Similar to VD and ELVD (Section 6.3-*Scope*), VS and ELVS are present in higher dimensions. For example, the generalization of VS in 3D can be found in [8, 126, 178].

Uniqueness

The original shape can be completely and unambiguously reconstructed from Blum's representation of the medial axis [28]. This property indicates the presence of one-to-one mapping between the MAT and the shape. In relation to VS, the MAT procedure can be repeated when attributing the points of the Voronoi edges with the distance value. Regarding ELVS of the polygonal shape, the reconstruction process implies collecting points with zero distance value in $\mathrm{CEF}_{\mathrm{DT}_2}$.

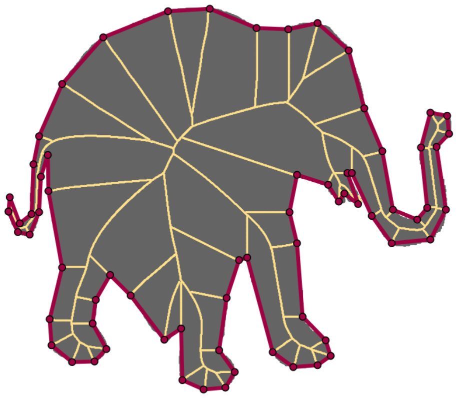

(a) VS from 50 line segments

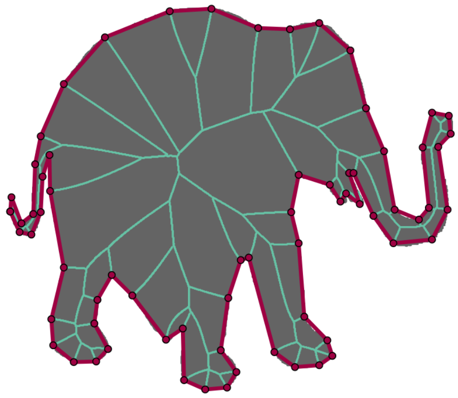

(b) ELVS from 50 line segments

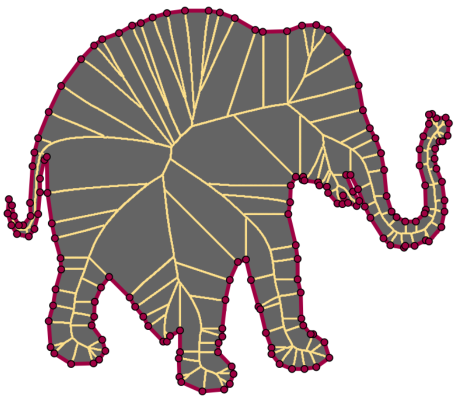

(c) VS from 170 line segments

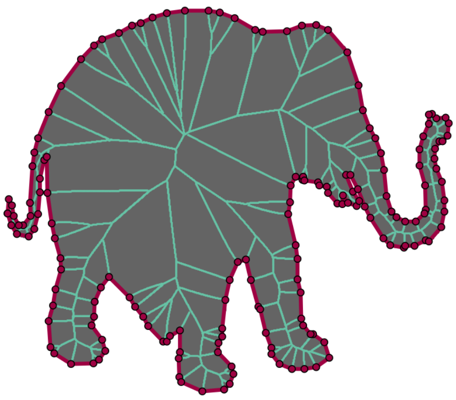

(d) ELVS from 170 line segments

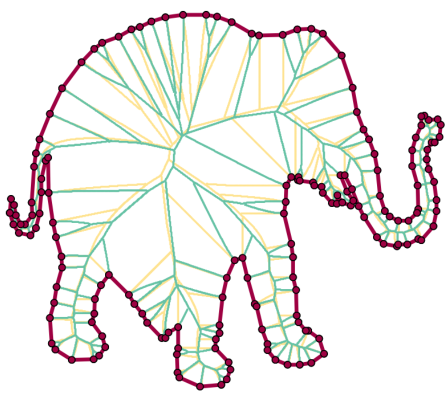

(e) VS and ELVS for uniform sampling

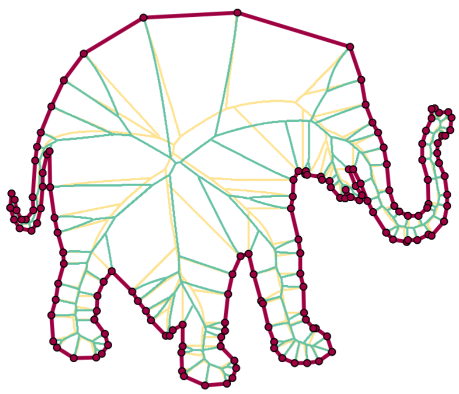

(f) VS and ELVS for non-uniform sampling

Figure 7.8: VS and ELVS of polygonal approximation of an elephant shape

Invariance

When VS and ELVS use the Euclidean distance as a proximity measure, the resultant representation is equivariant to translation, rotation [148], and scaling [18, 140].

Stability

VS is highly prone to local perturbations on the boundary. Attali et al. [7] claim that small modifications of shape introduce rather local spurious branches and do not highly influence the entire medial axis. Also, to preserve the topology and subtle details of the natural shapes, it is needed to have an accurate approximation with a high number of vertices [170]. In turn, each vertex induces the creation of additional spurious branches that do not correspond to the essential parts of this shape [134]. To guarantee stability, VS requires an additional pre/post-processing step for reducing the noise impact and make the skeleton closer to the medial axis [166]. Various authors introduced the residual functions for distinguishing curves that correspond to spurious branches from those that capture the essential parts of the object. Ogniewicz et al. [133, 134] attributed VS with supplementary information like measures of prominence and stability. Other pruning measures include region reconstruction [9, 16], residual branch length [107], bending ratio [177], visual contribution [17], and collapsed boundary length [197]. The preprocessing steps, such as boundary smoothing [150] or shape blurring [54], also cause the insensitivity of the representation to redundant artefacts.

Establishing pruning techniques for ELVS is a question for future research. In principle, the idea of attributing the skeletal points with a measure of significance is applicable to ELVS. Implicitly, there is already a prioritization of longer line segments and acute angles (Property 34) implying the noisy parts of the boundary to have shorter branches in the resultant skeleton.

Accuracy

The computational precision of VS and ELVS follows the results of VD and ELVD. In Section 6.3-*Accuracy*, the methods for VD are computed in a fixed-precision arithmetic [90, 103, 191]. The maximum error of the proposed in [100] algorithm is $\frac{3\sqrt{2}}{2}$ pixel_edge_length.

Efficiency

Since VS and ELVS are derived from VD and ELVD, the worst-case complexity of the VS algorithms equals $O(NlogN)$ and $O(N)$ for GPU implementation [90, 103, 191]. Here, N denotes the number of sites. Aggarwal et al. [1] presented a linear-time method for computing VD of a convex polygon.

Due to VD logic, VS contains elementary peripheral branches that do not correspond to significant parts of the shape [166]. Also, the higher sampling density increases the costs of pruning the spurious branches. Therefore, the methods from this category consider a trade-off between the accuracy of the medial axis and the computational costs [161].

Since ELVS is based on ELVD, the respective algorithms can be used to compute a skeleton. For instance, Langer [100] proposed a parallel linear-time algorithm for ELVS.

Abstraction

The medial axis concisely represents the shape and captures even its subtle details. Hierarchical approaches enable adapting the representation for the needs of the particular application by weighting the sites according to their importance [36, 53, 134].

7.5 Summary

One practical application of ELVD is skeletonization. As follows from the properties, ELVS implicitly prioritizes the longer edges and acute angles. This fact has an implication on the structure of the skeleton – in general, it is non-medial and is shifted towards the smaller edges. Only in special cases, ELVS is identical to VS. Such an implicit prioritization might cause the intersection of the pair of skeletal branches twice – in exo- and endoskeleton. This is not the case for VS.

CHAPTER 8

Applications

The previous chapters presented theoretical findings connected to conics and their generalizations. In computer vision there are problems that are geometric in nature. Here, the aim is to overview the application-driven solutions benefiting from the properties of the generalized conics.

8.1 Shape Smoothing

This section is based on the following publication:

Aysylu Gabdulkhakova, Maximilian Langer, Bernhard W. Langer, Walter G. Kropatsch: *Line Voronoi Diagrams Using Elliptical Distances.* In Proceedings of the Joint IAPR International Workshop on Structural, Syntactic, and Statistical Pattern Recognition, pages 258–267, 2018 [69]

Shape smoothing aims at preserving the object details and vanishing the irrelevant artefacts and noise (Figure 8.1). For instance, the robustness of medial representations such as VS highly depends on the presence of noise along the boundary [133]. Hence, one purpose of the shape smoothing approaches lies in mitigating the effect of contour perturbations to improve the reliability of further processing [106]. To control the extent of smoothing, the existing methods have an associated tuning parameter. It enables achieving

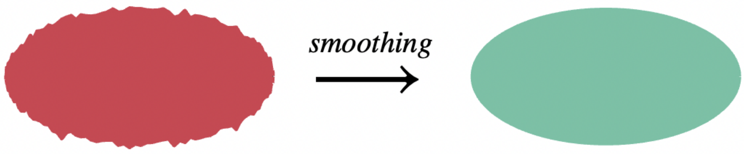

Figure 8.1: Idea behind the shape smoothing

representation of the object at different level of detail.

8.1.1 State-of-the-Art

The noise points might fluctuate locally around the shape or be further away creating high-frequency peaks. A variety of existing techniques relies on region and contour features for smoothing. The first group of methods performs shape smoothing by pruning its medial axis [79, 134]. The spurious branches do not contribute to the descriptive shape structure and their skeletal points have a low value according to the given measure of prominence. The idea of medial axis based approaches rests on keeping the skeletal points whose measure of prominence is above the threshold. For the measure of prominence, Ho et al. [79] focused on the distances between the chord or arc of maximal disk and the corresponding boundary points. Ogniewicz et al. [134] introduced a set of residual functions assuming the skeletal branches deep in the shape interior to be less sensitive to the boundary perturbations. By varying the pruning parameters it is possible to achieve a multiscale representation.

The contour-based methods smooth a particular feature in the local neighborhood of boundary points. This feature can be, for example, pixel coordinates [123] or local curvature [87]. The set of N consecutive neighbors form a *window of size* N. Here, it is considered that the window contains an odd number of points such that the smoothed point is located at its center. The larger the window size – the stronger the smooth [37]. A classical approach in this category is called *moving average* [84, 89, 123]. It successively substitutes each contour point by a non-weighted average of the points in the corresponding window. Despite the simplicity, fast processing, and strong reduction of random noise, the algorithm is not suitable for frequency domain [37, 183]. Iteratively applying the moving average to a contour is referred to as *multiple-pass moving average* [183]. After multiple passes the

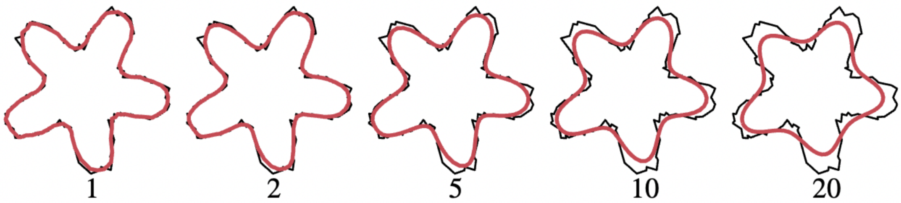

(a) multiple-pass moving average

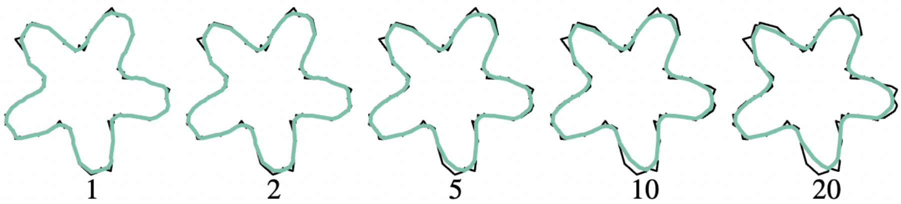

(b) EDP-based smoothing

Figure 8.2: Comparison of smoothing results after 1, 10 and 20 iterations. The original contour contains 100 points

result is similar to using a kernel. For example, after four or more iterations, the distribution of accumulated weights approaches the Gaussian [183]. The original global shape parameters, such as area, are influenced during this smoothing procedure. This effect is illustrated in Figure 8.2a. The multiple-pass moving average is applied to the flower shape (black) with noise. With an increase of iterations from 1 to 20, the resultant smoothed shape (red) shrinks. Another method directly applies a convolution with the Gaussian kernel [95, 110, 207]. Gaussian smoothing outperforms the moving average in frequency domain but takes more time due to convolution [183]. This approach enables creating the shape representation at multiple scales by changing the variance value [15, 95, 110, 207]. At the finest level the shape is original, whereas at the coarsest level the subtle details are suppressed. Lindeberg [106] formulated the scale-space theory for the discrete case.

Savitzky-Golay filter [168], considered a weighted moving average [48], fits an N-th degree polynomial with least-squares by applying convolution coefficients across the window. Here, the maximum N value is 5. Compared to the moving average, it preserves the high-frequency peaks better at the price of less noise reduction [138]. Locally weighted regression, or LOESS [43–45], performs successive weighted least-squares fitting of lower degree polynomials in a local neighborhood of each boundary point. In contrast to Savitzky-Golay filter, each neighbor gets a weight depending on a distance from the point to be smoothed. LOESS is sensitive to the presence of outliers and has high computational costs [22].

Wavelets [41] are efficiently and successfully applied to smoothing task and enable multiscale representation. The related methods are based on an assumption that the noise corresponds to high frequencies, whereas the significant parts of the object are located at low frequencies [96, 124]. One way to compute the multi-scale representation is by convolution with wavelet coefficients [112]. In the past decades, a variety of different wavelets with their properties and limitations has been discovered [5]. The problem is how to choose the wavelet for a particular application and data [111].

8.1.2 Equal-Detour-Point-based Smoothing

Langer [69] modified the moving average approach with three-point window by substituting the mean by EDP. In other words, let a shape boundary be formed by a set of points. The Equal-Detour-Point-based Contour Smoothing (or EDP-based smoothing) successively substitutes the vertex B by EDP for each triplet (A, B, C) of consecutive points.

Compared to the mean, EDP location depends on the angles. In Figure 8.3, the mean for various triangles is marked with a yellow diamond. It averages the coordinates of all vertices independent of the angle at the vertex B. EDP is marked with a green square. As follows from Corollary 1, in an acute-angled triangle, the Equal Detour Point (EDP) is shifted towards the side opposite to an acute angle (Figure 8.3b). In contrast, EDP is relatively close to the vertex corresponding to an obtuse angle (Figure 8.3c).

Without loss of generality, these EDP properties provide the following advantages for shape smoothing. First, in the presence of strong outliers (like in Figure 8.3b), EDP is much closer to $\overline{AC}$ than the mean. Second, when the angle at the vertex B is obtuse, EDP is spatially close to the vertex B. Consequently, the degree of smoothing decreases as compared to the mean. Thus, compared to multiple-pass moving average, with the increase of iterations the shape shrinkage is slower (Figure 8.2b). Finally, EDP enables better approximation of step-like contours. Figures 8.4a and 8.4c illustrate various triplets of points $(A_1, B, C), (A_2, B, C), \ldots, (A_7, B, C)$. Here, the circles mark the points, and the squares show the locations of EDP and mean. Various colors help finding the correspondence between them. Note

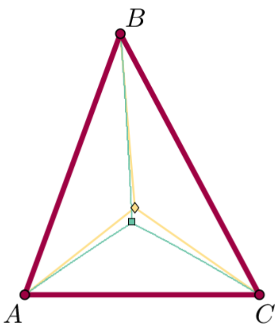

(a) angles are comparably similar

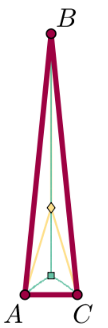

(b) vertex B has a much smaller angle

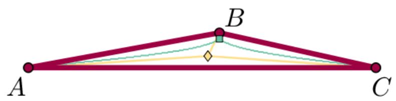

(c) vertex B has a much larger angle

Figure 8.3: EDP (square) and mean (diamond) in a triangle

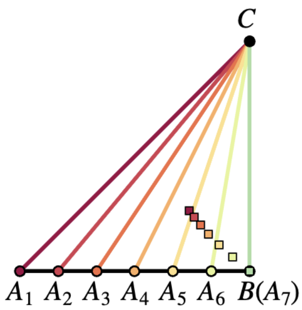

(a) EDP location

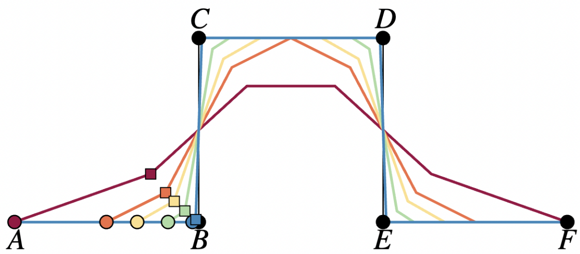

(b) EDP-based smoothing

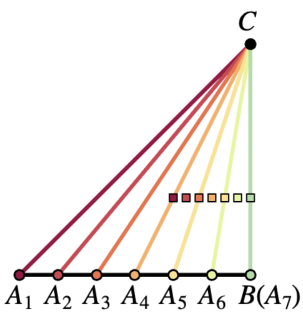

(c) mean location

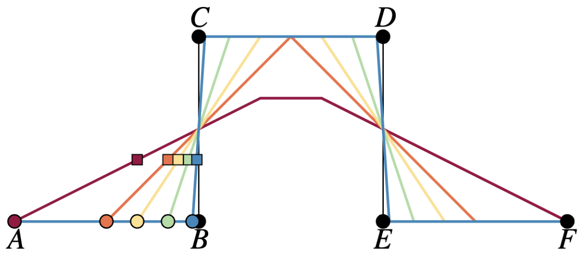

(d) moving average

Figure 8.4: EDP-based smoothing and moving average for sharp corners

that A_7 coincides with B and $\overline{CB}$ is perpendicular to the line containing $A_1, A_2, \ldots, A_7$. Figure 8.4a shows that decreasing the distance between the points A_i and B, where $i \in [1, \ldots, 7]$, leads to EDP approaching B. In Figure 8.4c, the mean points are located at a line parallel to A_1B. As a result, with an increase of discretization, EDP-based smoothing (Figure 8.4b) better approximates the step-like contours that the moving average (Figure 8.4d).

According to Property 31, EDP-based smoothing provides a possibility of preserving sharp corners or important details by keeping the original position of the corresponding points. It can be done by including such points twice in the contour: the triangle degenerates into a line segment, and EDP coincides with the duplicated point. This effect is observed in Figure 8.4a for the triplet (A_7, B, C), where A_7 and EDP coincide with B.

8.1.3 Experimental Results

The criteria for assessing shape smoothing techniques depend on features that are intended to be removed while keeping those that are considered being essential. In this section, the goal is to assess the properties of EDP when applied to smoothing.

Outlier removal

As mentioned in Section 8.1.2, EDP provides advantages in the presence of strong outliers. Here, EDP-based smoothing is compared to moving average, Gaussian smoothing, Savitzky-Golay filter, and LOESS. Selection of the wavelet-based approaches is a process requiring an expert knowledge and evaluation [56]. Hence, this algorithm is not considered for comparison. A critical argument is that the state of the art methods are applied to time series data [44, 168] which, in fact, reflects a sequential change of one value. Therefore, similar to [123], the successive change of point coordinates x and y is expressed with regard to the path length along the contour. The evaluation is performed on a camel shape from MPEG-7 dataset [182]. A point strongly deviating from the contour is added artificially (Figure 8.5a).

Figure 8.5 illustrates the results (red) of applying the above methods on the camel shape (green). The parameters used in each evaluated algorithm delivered the least number of pixels that do not belong to the outlier-free shape. Here, MA-3 and MA-22 denote moving average algorithm with a window size 3 and 22 correspondingly; G-6.5 is a Gaussian smoothing with sigma

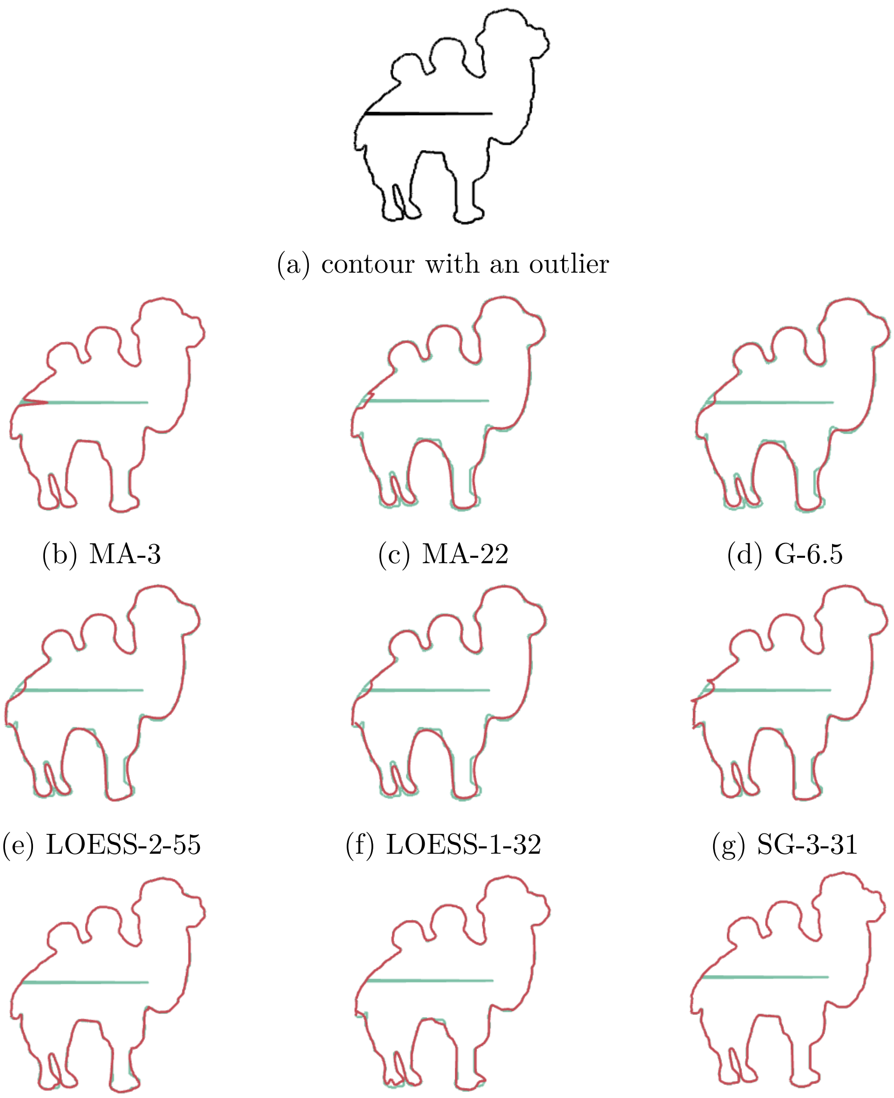

(a) contour with an outlier

(b) MA-3 (c) MA-22 (d) G-6.5

(e) LOESS-2-55 (f) LOESS-1-32 (g) SG-3-31

(h) R-LOESS-2-6 (i) R-LOESS-1-6 (j) EDP-1

Figure 8.5: Comparison of smoothing results on contour with a strong outlier. The acronyms of methods are: MA-N – moving average with window size N; G-S– Gaussian smoothing with sigma S; SG-D-N–Savitzky-Golay filter with a polynomial degree D and window size N; LOESS-D-N–LOESS with a polynomial degree D and window size N; R-LOESS-D-N–Robust LOESS with a polynomial degree D and window size N; EDP-I–EDP-based smoothing with I iterations

being equal to 6.5; SG-3-31 is a Savitzky-Golay approach with a polynomial degree 3 and the window size 31; LOESS-D-N expresses LOESS algorithm that uses a polynomial degree D and a window size N; R-LOESS-D-N is a robust version of LOESS algorithm.

As can be observed, the effect of the strong outlier is mitigated only by robust version of LOESS algorithm (Figures 8.5h and 8.5i) and EDP-based smoothing (Figure 8.5j). The moving average and Gaussian smoothing approaches decrease the magnitude of deviation. Applying multiple iterations on these methods causes shrinkage of the shape and stronger vanishing of the contour. Savitzky-Golay and LOESS algorithms are least-squares methods, thus, are sensitive to high-frequency peaks. The robust version of LOESS assigns a zero weight to the points that are far away from the local neighbors. Hence, the effect of such an outlier can be decreased. Regarding the precision, the smoothed outlier deviates from its location in the original outlier-free contour by less than a pixel for R-LOESS-2-6, R-LOESS-1-6, and EDP-based method. Although, the linear complexity of the proposed algorithm is comparably lower than the complexity of the LOESS method [184].

Detail preservation

The state of the art methods associate noise points with high frequences [41,44, 110,123,168,183,207] that are suppressed after smoothing. In particular cases it could be important to keep some high-frequency parts while smoothing the others. To exemplify, consider the deer shape (Figure 8.6a). Imagine a necessity of smoothing the body parts while keeping the head and tail without a change. The EDP-based strategy preserves parts of the original shape by duplicating the corresponding vertices in its contour. Regardless the number of iterations, these vertices remain at the original location since they coincide with EDP in the respective triplet of points (Property 31). Figure 8.6b shows the result of EDP-based smoothing after applying 100 iterations. Red curves highlight the points that were inserted twice in the contour, blue curves – the remaining points of the contour, green area illustrates the original shape. As can be seen, smoothing mitigated the presence of subtle perturbations, though, the head and tail (red) are identical to the corresponding parts in the original shape. Note, such detail preservation has a local effect. Figure 8.6c compares EDP-based smoothing of the contour with detail preservation (red) and without (blue). Except for the tail and head, the resultant curves coincide.

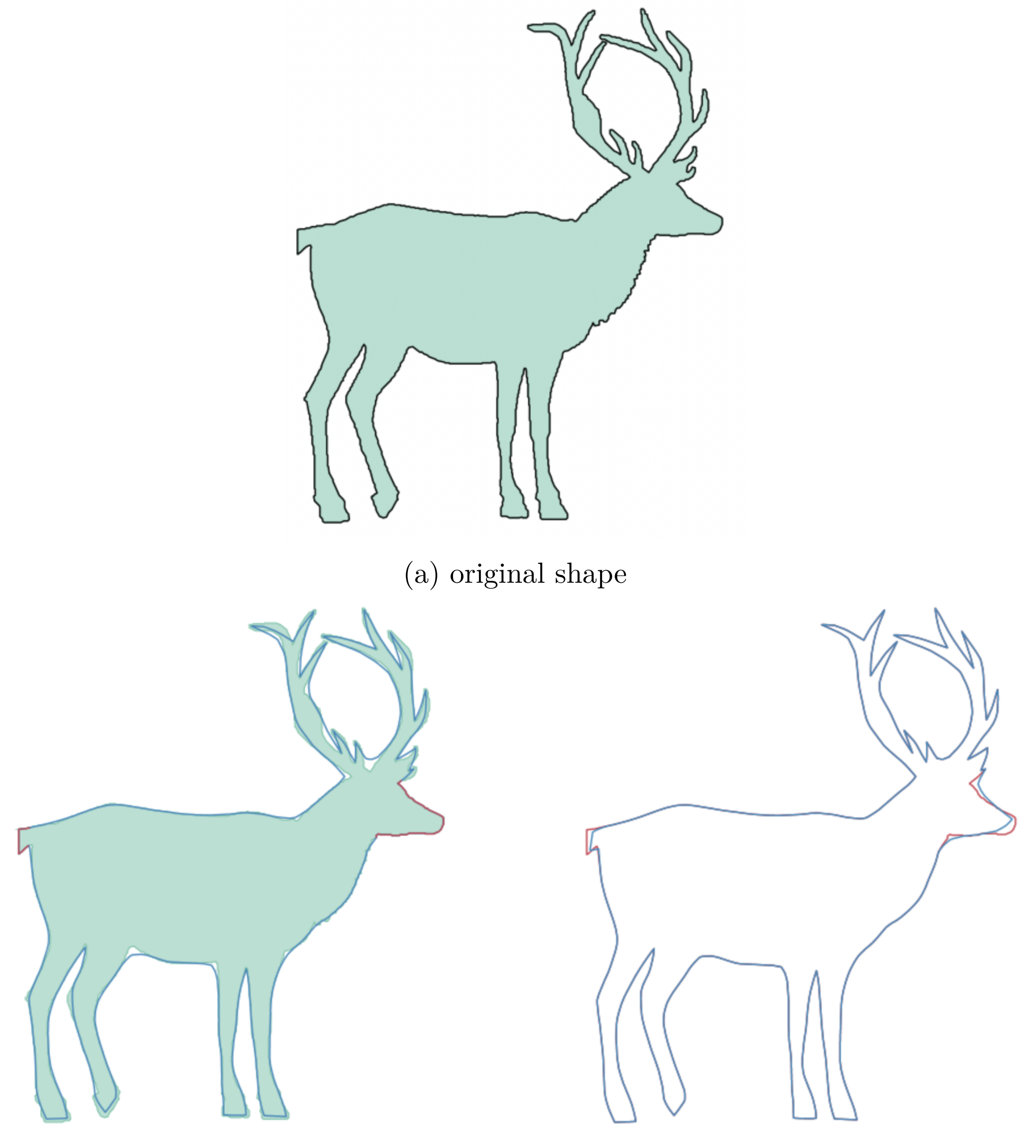

(a) original shape

(b) smoothed parts (blue), preserved parts (red), original shape (green)

(c) smoothing with detail preservation (red) and without (blue)

Figure 8.6: Comparison of EDP-based smoothing results after 100 iterations

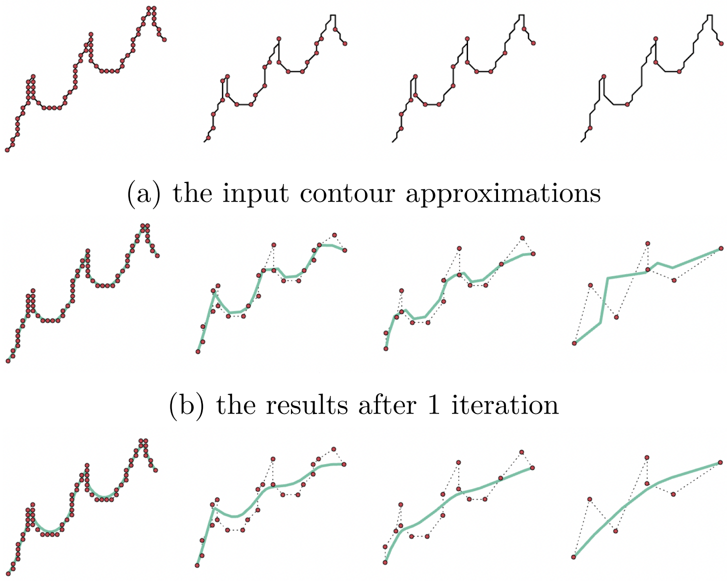

(a) the input contour approximations

(b) the results after 1 iteration

(c) the results after 10 iterations

Figure 8.7: Dependence of EDP-based smoothing on contour approximation

Dependence on contour approximation

EDP-based smoothing successively takes three consecutive points along the contour. Thus, in the case of a detailed contour approximation, where the points are densely located next to each other or even belong to the same line, the difference between the smoothed and noisy data is negligible.

Figure 8.7a shows various approximations (red points) of a scaled noisy contour part obtained by increasing the distance between consecutive points. Figures 8.7b and 8.7c illustrate the results of EDP-based smoothing (green curves) after 1 and 10 iterations respectively. As can be observed, for dense approximation (left column) the smoothed contour contains the noisy spikes even after 10 iterations. In such a case, the properties of EDP are not helpful, since the points remain at the same positions or slightly move in the local neighborhood. With the decrease of the number of points along the contour, the noisy spikes are smoothed out. The same issue with contour approximation applies to the state of the art methods. Apart from sparsification, [44, 110, 123, 168, 183, 207] consider increasing the window size. In relation to EDP-based smoothing, assuming a larger window is question for future research.

8.2 Optimal Path Planning

This section is based on the following publication:

Aysylu Gabdulkhakova, Walter G. Kropatsch: *Generalized conics: properties and applications.* In Proceedings of the International Conference on Pattern Recognition, pages 10728–10735, 2020 [67]

The demand for optimal path planning algorithms comes from a wide variety of fields, such as robotics, computer graphics, geographic information systems, architectural and VLSI design [25]. The problem is geometric in nature and is concerned with the question of finding a sequence of moves that bring the object from the source to the destination. The environment might additionally contain the disjoint obstacles that are supposed to be avoided. The collision-free path is evaluated according to certain criteria like the overall length and smoothness, computational costs and time [25, 72, 203, 209].

8.2.1 State-of-the-Art

The optimal path planning is a thoroughly and continuously researched topic with a great variety of approaches [72,209]. With the reference to classification in [72], this section is related to a particular category of global approaches called the roadmap methods. The global approaches consider a complete map of environment to be provided a priori. By definition, a roadmap is a set of curves that express possible collision-free paths in the given map [101]. The idea is to connect the source and the destination to the roadmap, in order to find the path between them. A group of approaches uses VD to compute the roadmap [25, 40, 203]. According to Definition 48, the resultant curves are equidistant to the obstacles and, thus, are at the maximum possible distance from them. Consequently, the obtained path is not the shortest, despite the computational efficiency [72]. Therefore, VD-based algorithms are combined with other techniques to improve optimality in the sense of path length [25, 203].

8.2.2 Elliptic-Line-Voronoi-Diagram-based Path

Elliptic Line Voronoi Diagram (ELVD) posesses beneficial properties for path planning applications. Let the map contain the set of line segments and polygonal objects that represent the obstacles. Each point in ELVD corresponds to the smallest increment to the length of at least two line segments from the set of obstacles. As confirmed by Property 34, the longer line segment pushes the Voronoi edges towards the shorter line segments. The advantage of such a non-centered representation is lower curvature at sharp corners. In practice, the vehicles using the ELVD-based trajectory could turn at a higher speed as compared to VD-based trajectory.

8.2.3 Experimental Results

The first experimental setup compares the paths extracted from VD and ELVD of the map that is a union of rectangles with different lengths but the same width (Figure 8.8). It could be associated with a long corridor forming a spiral shape. The task is to find a path in this corridor to connect the destination (red square) and the source (green circle). As discussed, according to Definition 48, each point in VD is equidistant to at least two boundaries of the shape (Figure 8.8a). In contrast, in ELVD there is a visible shift towards the corner that corresponds to the shorter border (Figure 8.8b). As a result, the path length in ELVD is shorter and the curvature at the sharp corners is lower than in VD. To have a quantitative comparison of the path length, Let the size of the bounding box around the spiral be 500 by 500 pixels (Figures 8.8a and 8.8b). The VD-based path length connecting the source and the destination equals 1391 pixels, whereas the ELVD-based path length – 1297 pixels. Note, in Figures 8.8a and 8.8b, the vehicle is represented by a point. To take the vehicle size into account it is possible to propagate the boundary of the shape towards its interior such that at the sharp corners there is sufficient space for the maneuver (Figure 8.8c).

The second experimental setup uses the map containing the set of obstacles that need to be avoided. It has six blue/yellow rectangles representing the obstacles and one bounding rectangle limiting the space (Figure 8.9). The green circle is the source, and the red square is the destination. The task is to find a collision-free path connecting the source and the destination. In VD-based path is equally distant from the obstacles regardless their size. Thus, the Voronoi edges separate only the nearest neighboring obstacles (yellow

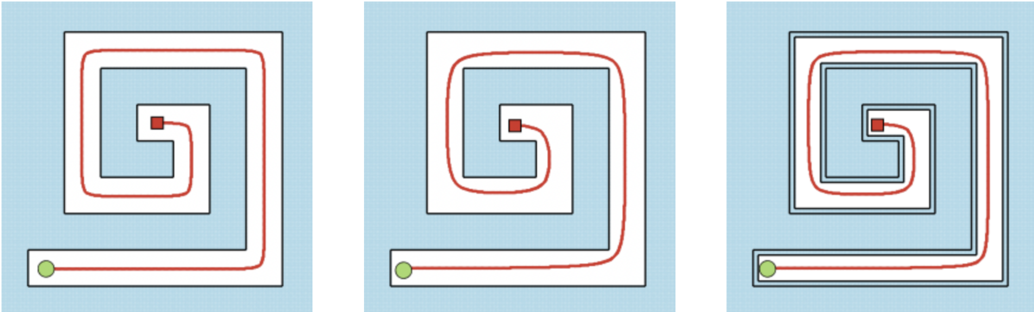

(a) VD-based path (b) ELVD-based path (c) ELVD-based path

Figure 8.8: Comparison of paths (red) in VD and ELVD of the spiral

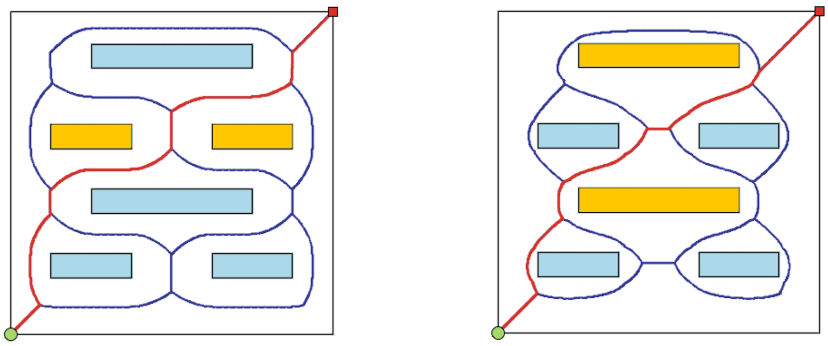

(a) VD-based path (b) ELVD-based path

Figure 8.9: Comparison of collision-free paths (red) in VD and ELVD

rectangles in Figure 8.9a). This is not the case for the non-centered path from ELVD. The intuition to this phenomena could be adopted from physics: the larger the planets are – the stronger is the attraction between them. Therefore, in ELVD the Voronoi edges can separate not the nearest but the largest obstacles (yellow rectangles in Figure 8.9b). Another observation relates to the angles at the turns. Compared to low curvatures in Figure 8.8b, the ELVD path in Figure 8.9b contains sharp turns that create a potential problem for the moving vehicle.

8.3 Optimal Facility Location

This section is based on the following publication:

Aysylu Gabdulkhakova, Walter G. Kropatsch: *Generalized conics: properties and applications.* In Proceedings of the International Conference on Pattern Recognition, pages 10728–10735, 2020 [67]

The problem of finding an optimal facility location is a classical optimization task [24]. It aims at finding a facility location that minimizes the sum of weighted distances to the given set of N point-locations with the positive weights $w_1, w_2, ..., w_N$. In principle, the point-location can be associated with a negative weight. In this case, its distance to the facility is maximized [130].

8.3.1 State-of-the-Art

In the literature, the optimal facility location problem is known under various names: minimum distance sum problem [119, 172], single facility location problem [125], Fermat-Weber problem [21,32]. The original formulation dates back to Fermat and Torricelli and considers only three points [127, 198, 199]. The solution for this particular scenario is referred to as Fermat point of a triangle [187]. Later, from the historical perspective, it became the first step in location theory and was related to the problem of locating the facility at a minimum transportation cost [204]. The existing methods include but are not limited to exact analytical solutions, enumeration of all the possible combinations, approximate statistical and heuristic methods, and linear programming [21, 24, 32, 119, 160, 172, 205]. The complexity of the problem increases with the number of points [19], causing the analytical or iterative solutions to become computationally expensive.

8.3.2 Optimal Facility Location from the Generalized Conics

As can be observed, the formulation of the optimal location problem with positive weights fits into multifocal ellipse (Definition 17), whereas with the positive and negative weights – into multifocal hyperbola (Definition 18). Thus, the solution is found by extracting the point from CMEF (or CMHF) with the smallest associated distance value. The implementation considers, first, computing DT_2s for the given set of N point-locations. Second, taking the pixel-wise sum among all these distance fields. Finally, the pixel associated with the smallest distance value defines a solution. The computational complexity equals $O(N \times W \times H)$, where W is the width, and H is the height of the image containing the area of interest. The parallel algorithm for CMEF enables loading the precomputed DT_2 and transferring the distance values with regard to N point-locations. The sums can be computed on a pixel-level leading to the total complexity of $O(N)$. This idea in relation to CEF is explained in [100]. The complexity of finding the minimum distance value equals $O(W \times H)$.

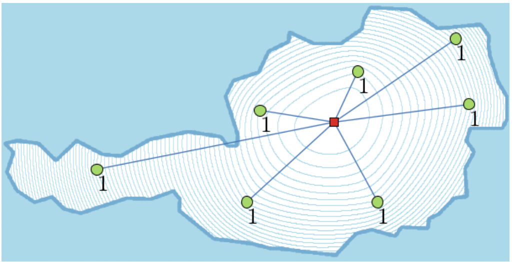

(a) all point-locations have identical weight

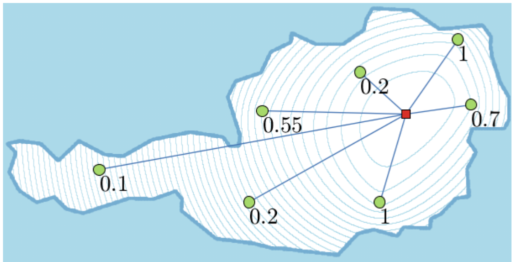

(b) the point-locations have various weights

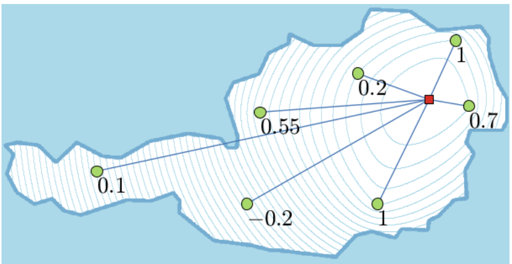

(c) the point-locations have positive and negative weights

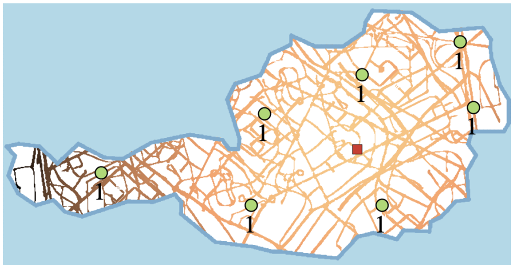

(d) the point-locations connected by the roads

Figure 8.10: The example of optimal facility location. The green circles correspond to seven point-locations, and the red square is the facility location. The level sets show the distance value distribution in CMEF (a)-(b) and CMHF (c)

8.3.3 Experimental Results

The results of the algorithm are illustrated in Figure 8.10. Consider an image showing a contour of Austria, where the green circles are the cities (point-locations) and the red square is the desired facility location. In Figures 8.10a and 8.10b, all the weights at the point-locations are positive, therefore, the red point corresponds to the global minimum of CMEF. Note, if there is an even number of collinear point-locations, there is more than one global minimum (Property 9). In Figure 8.10a, the point-locations have identical weights, as opposed to Figure 8.10b. As a result, the facility location is shifted towards the point-locations with the greater weights. Figure 8.10c illustrates the case when the weights have different signs: positively weighted point-locations attract the global minimum, whereas the negatively weighted – repulse.

So far the distance between two point-locations is measured with the Euclidean metric. To have a realistic picture, it is possible to apply the constraint distance transform [144] to the binary image of roads. Instead of a line segment connecting two point-locations, there will be a shortest path along the roads.

8.4 Shape Representation

This section is based on the following publication:

Aysylu Gabdulkhakova, Walter G. Kropatsch: *Generalized conics with the sharp corners.* In Proceedings of the Iberoamerican Congress on Pattern Recognition, pages 419–429, 2021 [68]

Shape representation is a fundamental part of solving any computer vision problem [47]. The intention is to efficiently preserve the essential object characteristics which depend on the requirements of a particular application [109]. It can work on a boundary level or consider the complete set of pixels belonging to the object. For example, Chapter 7 introduced ELVS which enables representing the internal structure of 2D shape using a set of 1D curves. This section intends to raise interest in the possibility of representing the shape boundary by using the properties of generalized conics (Chapter 3).

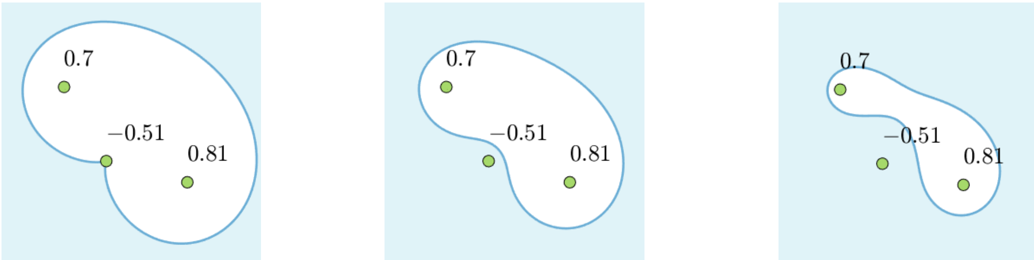

(a) varying the value of distance sum to the focal points

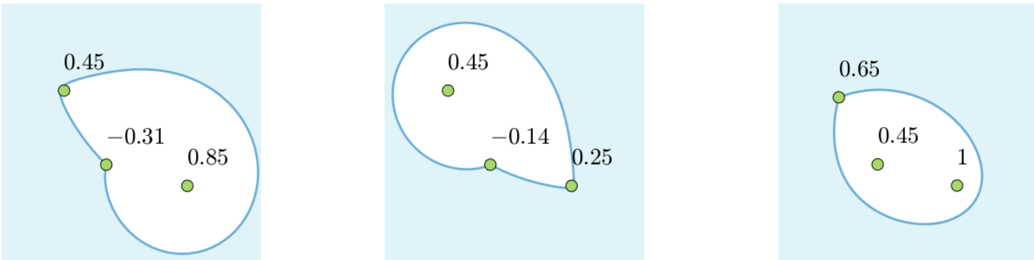

(b) varying the weights of the focal points

Figure 8.11: Examples of shapes generated from the same triplet of focal points

In order to specify a generalized conic, one needs locations of focal points, their associated weights, and the value of constant weighted sum. Consider the examples in Figure 8.11, where the locations of three focal points are fixed while changing the value of the constant weighted sum (Figure 8.11a) or the weights (Figure 8.11b). As can be observed, if the weights are all positive, then the generated shape is convex, whereas the concavities are obtained by introducing the negatively weighted focal point(s). Note the variety of complex shapes generated from the triplet of points. The computation of confocal generalized conics is performed efficiently by taking the pixel-wise sum of DT_2s generated from the focal points. In contrast, finding an analytical representation of such shapes has a higher computational complexity: the degree of the corresponding polynomial increases with every additional focal point [131].

The idea for the future work is to research the possibility of representing a complex shape by finding an appropriate number of focal points, their locations, weights, and the value for the sum of weighted distances. What

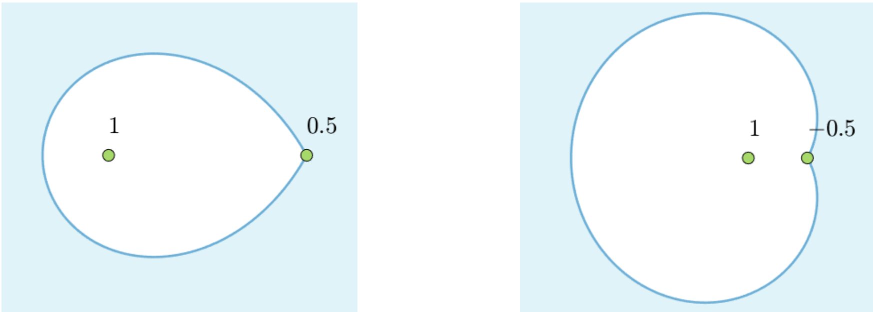

(a) egg-shape (b) hyperbolic shape

Figure 8.12: The examples of generalized conics with corners

is the minimum number of focal points that represent or approximate the shape? What is the best possible approximation of the shape for the given number of focal points? What shapes can be represented with the generalized conics? As can be observed, all the parameters are numeric. Thus, one way to answer such questions could be connected to using the advances of machine learning.

A particular scenario – an egg-shape (Figure 8.12a) or a hyperbolic shape (Figure 8.12b) with corner. On one side, it is possible to compute the parameters of such shapes given a boundary. On the other side, as compared to an ellipse, these shapes require only one additional parameter – the weight of focal point at the corner. Hence, the egg-shape and the hyperbolic shape enrich the ellipse advantages in the related applications.

CHAPTER 9

Conclusion

There is no branch of mathematics, however abstract, which may not some day be applied to phenomena of the real world.

Nikolai Ivanovich Lobachevsky

Computer vision is a scientific field whose central purpose is to gain semantic information about the environment from a digital image. It implies a selection of features providing a meaningful representation of objects. In this regard, mathematics introduces a *language* that enables *translating* a physical entity into a computational model. The richer the vocabulary – the broader the information spectrum describing the object. This thesis introduces the new word into the shape representation dictionary – *generalized conics.*

Conceptually, the generalized conics are the extension of primitives already used in image processing – a circle and an ellipse. Consequently, the relatively familiar geometric properties are generalized by accepting infinitely many focal points. It implies an establishment of a single theoretical framework that qualitatively enhances the explanation of existing ideas while presenting the advantages of the generic entity.

Apart from the study of geometrical concepts, this thesis exploits the identified properties of the generalized conics in the image processing domain. The proposed methods, on one side, generalize the existing shape representations based on the distance fields. On the other side, they enrich the variety of semantic information connected to the corresponding representation while improving the computational efficiency. The practical part of the thesis exemplifies the application scenarios, where the explored properties and methods are beneficial compared to the state-of-the-art.

The central question underlying this work is connected to the ways of measuring the distance from a point to an object. A classical approach finds a pair of the closest points. In the specific cases, this implies the need for object discretization. This thesis proposes the alternative solutions based on the properties of the generalized conics:

- Confocal-Ellipse-based Distance (CED) – metric for computing the distance between the points on confocal ellipses. Since an ellipse can degenerate into a line segment, CED is interpreted as a distance between a point and a line segment. Here, the latter is defined by the endpoints, implying the independence of discretization.

- Confocal Elliptic Field (CEF) – distance field that uses CED as a metric. The level sets in CEF of a line segment are confocal ellipses. The separating curve takes the form of a bisector, a hyperbola branch, or a multifocal hyperbola branch (higher-order curve). To compute CEF, it suffices to apply simple operations (addition, subtraction, and minimum) to several Euclidean Distance Fields (DF_2).

- Confocal Multifocal Elliptic Field (CMEF) – distance field containing multifocal ellipses. Each point in this field is associated with the sum of the distances to the objects in the set. Convexity of the level sets makes this representation useful for solving optimization problems. Similar to CEF, it can be decomposed into a set of DF_2s and computed by applying addition and multiplication to them.

- Confocal Multifocal Hyperbolic Field (CMHF) – distance field containing multifocal hyperbolas. Each point in this field is associated with the difference between the distance values in a pair of CMEFs. Conceptually, the zero level set is a set of points equidistant to the given pair of CMEFs.

Eventually, the distance fields that inherit the properties from ellipses or multifocal ellipses demonstrate the proximity of objects with respect to each other. The distance fields which are based on the properties of hyperbolas or multifocal hyperbolas show the regions of closest proximity for each object. Interpreting these notions in the digital space takes an advantage of the Distance Transform (DT). Let N be the number of points, line segments, or sites, and $W \times H$ be the number of pixels in an image.

- Confocal Elliptic Field in terms of DT (CEF_{DT}) – digital version of CEF with DT. The computational complexity of implementation reaches $O(N \times W \times H)$ [100].
- Confocal Multifocal Elliptic Field in terms of DT (CMEF_{DT}) – digital version of CMEF with DT. The computational complexity equals $O(N \times W \times H)$.
- Confocal Multifocal Hyperbolic Field in terms of DT (CMHF_{DT}) – digital version of CMHF with DT. Its computational complexity is $O(W \times H)$.
- Elliptic Line Voronoi Diagram (ELVD) – space tessellation extracted from CEF. It can be considered a generalization of the Voronoi Diagram (VD) since providing identical results for the point-sites. Compared to VD, in the case of connected and overlapping line segments, the Voronoi edges do not contain area. The efficient implementation of the algorithm [100] achieves $O(N \times W \times H)$.
- Elliptic Line Voronoi Skeleton (ELVS) – shape representation that is extracted from ELVD, hence, inheriting its properties. ELVS is a non-medial representation, as opposed to classical VS or medial axis. ELVS has an implicit prioritization of long line segments and acute angles. Its computational complexity is $O(N \times W \times H)$ [100].

Each of the above algorithms has a potential for parallel computation. It leads to further improvement of the computational complexity.

Broadly speaking, the generalized conics might become a promising research direction in computer vision and image processing. This thesis explores the geometrical properties of curves obtained from simple operations – addition and subtraction – in 2D space. The existing literature defines also another type of generalization [71], obtained as a weighted sum of distance products. Analysing such level sets might further enrich the representational power of the existing methods. From the perspective of shape representation, a particular emphasis of this work was on the special case – the generalized conics with sharp corners. Hence, it would be of interest to establish the correspondences between the weights and the smooth level sets. Another valuable theoretical prospect is related to ELVD and the exploration of its dual representation.

Understanding the specific aspects of problem together with knowledge of mathematical framework enables applying the generalized conics in the practical domain. This thesis outlined a problem variety, such as shape smoothing, optimal path planning, and optimal facility location. In shape representation, the generalized conics exhibit a representational power that might be used to connect machine learning and geometrical structure. Another idea is related to exploration of geometrical properties in N-dimensional space with an outlook to data mining algorithms. In particular, it implies the thorough analysis of the global minimum of confocal generalized conics in the presence of outliers, as well as the evaluation of its stability with the reference to state-of-the-art approaches. In general, the extension of the work to higher dimensions has a valuable impact on research and a variety of applications that can benefit from it.

Index

Bibliography

[1] A. Aggarwal, L. J. Guibas, J. Saxe, and P. W. Shor, “A linear-time algorithm for computing the Voronoi diagram of a convex polygon,” *Discrete & Computational Geometry*, vol. 4, no. 6, pp. 591–604, 1989.

[2] N. Ahuja and J.-H. Chuang, “Shape representation using a generalized potential field model,” *IEEE Transactions on Pattern Analysis and Machine Intelligence*, vol. 19, no. 2, pp. 169–176, 1997.

[3] O. Aichholzer, F. Aurenhammer, D. Chen, D. Lee, and E. Papadopoulou, “Skew Voronoi Diagrams,” *International Journal of Computational Geometry & Applications*, vol. 9, no. 03, pp. 235–247, 1999.

[4] O. Aichholzer, W. Aigner, F. Aurenhammer, T. Hackl, B. Jüttler, E. Pilgerstorfer, and M. Rabl, “Divide-and-conquer for Voronoi diagrams revisited,” *Computational geometry*, vol. 43, no. 8, pp. 688–699, 2010.

[5] C. M. Akujuobi, *Wavelets and Wavelet Transform Systems and Their Applications.* Springer, 2022.

[6] T. M. Apostol and M. A. Mnatsakanian, *New horizons in geometry.* The Mathematical Association of America, 2017, vol. 47.

[7] D. Attali, J.-D. Boissonnat, and H. Edelsbrunner, “Stability and computation of medial axes – a state-of-the-art report,” in *Mathematical*

Foundations of Scientific Visualization, Computer graphics, and Massive Data Exploration. Springer, 2009, pp. 109–125.

[8] D. Attali and A. Montanvert, "Computing and simplifying 2D and 3D continuous skeletons," *Computer Vision and Image Understanding*, vol. 67, no. 3, pp. 261–273, 1997.

[9] D. Attali, G. Sanniti di Baja, and E. Thiel, "Pruning discrete and semi-continuous skeletons," in *Proceedings of the International Conference on Image Analysis and Processing*, 1995, pp. 488–493.

[10] F. Aurenhammer, "Power diagrams: properties, algorithms and applications," *SIAM Journal on Computing*, vol. 16, no. 1, pp. 78–96, 1987.

[11] F. Aurenhammer, "Voronoi Diagrams – a survey of a fundamental geometric data structure," *ACM Computing Surveys*, vol. 23, no. 3, pp. 345–405, 1991.

[12] F. Aurenhammer, B. Jüttler, and G. Paulini, "Voronoi Diagrams for parallel halflines and line segments in space," in *Proceedings of the International Symposium on Algorithms and Computation*, 2017, pp. 7:1–7:10.

[13] F. Aurenhammer and R. Klein, "Voronoi Diagrams," *Handbook of computational geometry*, vol. 5, no. 10, pp. 201–290, 2000.

[14] F. Aurenhammer, R. Klein, and D.-T. Lee, *Voronoi Diagrams and Delaunay triangulations*. World Scientific, 2013.

[15] J. Babaud, A. P. Witkin, M. Baudin, and R. O. Duda, "Uniqueness of the Gaussian kernel for scale-space filtering," *IEEE Transactions on Pattern Analysis & Machine Intelligence*, vol. PAMI-8, no. 1, pp. 26–33, 1986.

[16] X. Bai and L. J. Latecki, "Discrete skeleton evolution," in *Proceedings of the International Workshop on Energy Minimization Methods in Computer Vision and Pattern Recognition*, 2007, pp. 362–374.

[17] X. Bai, L. J. Latecki, and W.-Y. Liu, "Skeleton pruning by contour partitioning with discrete curve evolution," *IEEE Transactions on*

Pattern Analysis and Machine Intelligence, vol. 29, no. 3, pp. 449–462, 2007.

[18] X. Bai, X. Yang, D. Yu, and L. J. Latecki, "Skeleton-based shape classification using path similarity," *International Journal of Pattern Recognition and Artificial Intelligence*, vol. 22, no. 04, pp. 733–746, 2008.

[19] C. L. Bajaj, "The algebraic degree of geometric optimization problems," *Discrete & Computational Geometry*, vol. 3, pp. 177–191, 1988.

[20] G. Barequet, M. T. Dickerson, and M. T. Goodrich, "Voronoi Diagrams for convex polygon-offset distance functions," *Discrete & Computational Geometry*, vol. 25, no. 2, pp. 271–291, 2001.

[21] A. Baskar, "Analysing a few trigonometric solutions for the Fermat-Weber facility location triangle problem with and without repulsion and generalising the solutions," *International Journal of Mathematics in Operational Research*, vol. 10, no. 2, pp. 150–166, 2017.

[22] A. B. Batista Júnior and P. S. d. M. Pires, "An approach to outlier detection and smoothing applied to a trajectography radar data," *Journal of Aerospace Technology and Management*, vol. 6, pp. 237–248, 2014.

[23] S. Berretti, A. Del Bimbo, and P. Pala, "Retrieval by shape similarity with perceptual distance and effective indexing," *IEEE Transactions on Multimedia*, vol. 2, no. 4, pp. 225–239, 2000.

[24] S. Bespamyatnikh, K. Kedem, and M. Segal, "Optimal facility location under various distance functions," in *Proceedings of the Workshop on Algorithms and Data Structures.* Springer, 1999, pp. 318–329.

[25] P. Bhattacharya and M. L. Gavrilova, "Voronoi diagram in optimal path planning," in *Proceedings of the International Symposium on Voronoi Diagrams in Science and Engineering*, 2007, pp. 38–47.

[26] P. Bhattacharya and M. L. Gavrilova, "Roadmap-based path planning – using the Voronoi Diagram for a clearance-based shortest path," *IEEE Robotics & Automation Magazine*, vol. 15, no. 2, pp. 58–66, 2008.

[27] J. Bloomenthal, C. Bajaj, J. Blinn, B. Wyvill, M.-P. Cani, A. Rockwood, and G. Wyvill, *Introduction to implicit surfaces.* Morgan Kaufmann Publishers, 1997.

[28] H. Blum, "A transformation for extracting new descriptors of shape," in *Models for the Perception of Speech and Visual Form.* MIT press, 1967, pp. 362–380.

[29] G. Borgefors, "Distance transformations in digital images," *Computer Vision, Graphics, and Image Processing*, vol. 34, no. 3, pp. 344–371, 1986.

[30] G. Borgefors, "On digital distance transforms in three dimensions," *Computer Vision and Image Understanding*, vol. 64, no. 3, pp. 368–376, 1996.

[31] G. Borgefors, I. Nyström, and G. Sanniti di Baja, "Computing skeletons in three dimensions," *Pattern Recognition*, vol. 32, no. 7, pp. 1225–1236, 1999.

[32] P. Bose, A. Maheshwari, and P. Morin, "Fast approximations for sums of distances, clustering and the Fermat–Weber problem," *Computational Geometry*, vol. 24, no. 3, pp. 135–146, 2003.

[33] M. Brady, "Criteria for representations of shape," in *Human and machine vision.* Elsevier, 1983, pp. 39–84.

[34] J. E. Bresenham, "Algorithm for computer control of a digital plotter," *IBM Systems Journal*, vol. 4, no. 1, pp. 25–30, 1965.

[35] R. A. Brualdi, *Introductory combinatorics.* Pearson, 2009.

[36] A. Bucksch and R. Lindenbergh, "CAMPINO – a skeletonization method for point cloud processing," *International Society for Photogrammetry and Remote Sensing Journal of Photogrammetry and Remote Sensing*, vol. 63, no. 1, pp. 115–127, 2008.

[37] A. Buja, T. Hastie, and R. Tibshirani, "Linear smoothers and additive models," *The Annals of Statistics*, vol. 17, no. 2, pp. 453–510, 1989.

[38] L. M. Chen, *Digital and discrete geometry: theory and algorithms.* Springer, 2014.

[39] L. P. Chew and R. L. (Scot) Drysdale, III, "Voronoi Diagrams based on convex distance functions," in *Proceedings of the Annual Symposium on Computational Geometry*, 1985, pp. 235–244.

[40] H. Choset and J. W. Burdick, "Sensor-based exploration: the hierarchical Generalized Voronoi Graph," *The International Journal of Robotics Research*, vol. 19, no. 2, pp. 96–125, 2000.

[41] G. C.-H. Chuang and C.-C. J. Kuo, "Wavelet descriptor of planar curves: Theory and applications," *IEEE Transactions on Image Processing*, vol. 5, no. 1, pp. 56–70, 1996.

[42] K. C. Ciesielski, X. Chen, J. K. Udupa, and G. J. Grevera, "Linear time algorithms for exact distance transform," *Journal of Mathematical Imaging and Vision*, vol. 39, no. 3, pp. 193–209, 2011.

[43] W. S. Cleveland, "Robust locally weighted regression and smoothing scatterplots," *Journal of the American statistical association*, vol. 74, no. 368, pp. 829–836, 1979.

[44] W. S. Cleveland and S. J. Devlin, "Locally weighted regression: an approach to regression analysis by local fitting," *Journal of the American Statistical Association*, vol. 83, no. 403, pp. 596–610, 1988.

[45] W. S. Cleveland and R. McGill, "Graphical perception and graphical methods for analyzing scientific data," *Science*, vol. 229, no. 4716, pp. 828–833, 1985.

[46] H. S. M. Coxeter and S. L. Greitzer, *Geometry revisited.* Mathematical Association of America, 1967.

[47] L. da Fontoura Costa and R. M. Cesar, Jr., *Shape analysis and classification: theory and practice.* CRC Press, 2000.

[48] W. Dai, I. Selesnick, J.-R. Rizzo, J. Rucker, and T. Hudson, "A nonlinear generalization of the Savitzky-Golay filter and the quantitative analysis of saccades," *Journal of vision*, vol. 17, no. 9, pp. 10–10, 2017.

[49] M. de Berg, O. Cheong, M. van Kreveld, and M. H. Overmars, *Computational geometry: algorithms and applications, 3rd Edition.* Springer, 2008.

[50] T. de Zeeuw, “Elliptical galaxies with separable potentials,” *Monthly Notices of the Royal Astronomical Society*, vol. 216, no. 2, pp. 273–334, 1985.

[51] N. Dergiades, “The Soddy circles,” *Forum Geometricorum*, vol. 7, pp. 191–197, 2007.

[52] S. L. Devadoss and J. O′Rourke, *Discrete and computational geometry.* Princeton University Press, 2011.

[53] T. K. Dey and W. Zhao, “Approximating the medial axis from the Voronoi Diagram with a convergence guarantee,” *Algorithmica*, vol. 38, no. 1, pp. 179–200, 2004.

[54] A. R. Dill, M. D. Levine, and P. B. Noble, “Multiple resolution skeletons,” *IEEE Transactions on Pattern Analysis and Machine Intelligence*, vol. 9, no. 4, pp. 495–504, 1987.

[55] G. L. Dirichlet, “Über die Reduction der positiven quadratischen Formen mit drei unbestimmten ganzen Zahlen,” *Journal für die reine und angewandte Mathematik (Crelles Journal)*, vol. 40, pp. 209–227, 1850.

[56] I. M. Dremin, O. V. Ivanov, and V. A. Nechitailo, “Wavelets and their uses,” *Physics-Uspekhi*, vol. 44, no. 5, p. 447, 2001.

[57] H. Edelsbrunner, *Algorithms in combinatorial geometry*, ser. Monographs in Theoretical Computer Science. An EATCS Series. Springer, 1987, vol. 10.

[58] H. Edelsbrunner, “Computational geometry,” in *Current Trends in Theoretical Computer Science - Essays and Tutorials (World Scientific Series Computer Science).* World Scientific Publishing, 1993, vol. 40, pp. 3–48.

[59] H. Edelsbrunner, L. J. Guibas, and J. Stolfi, “Optimal point location in a monotone subdivision,” *SIAM Journal on Computing*, vol. 15, no. 2, pp. 317–340, 1986.

[60] P. Erdös and I. Vincze, “On the approximation of convex, closed plane curves by multifocal ellipses,” *Journal of Applied Probability*, pp. 89–96, 1982.

[61] R. Fabbri, L. F. Estrozi, and L. Da F. Costa, “On Voronoi diagrams and medial axes,” *Journal of Mathematical Imaging and Vision*, vol. 17, pp. 27–40, 2002.

[62] I. D. Faux and M. J. Pratt, *Computational geometry for design and manufacture.* Horwood, 1979.

[63] A. R. Forrest, “II. Current developments in the design and production of three-dimensional curved objects - Computational geometry,” *Proceedings of the Royal Society A: Mathematical, Physical and Engineering Sciences*, vol. 321, no. 1545, pp. 187–195, 1971.

[64] S. Fortune, “A sweepline algorithm for Voronoi diagrams,” *Algorithmica*, vol. 2, no. 1-4, p. 153, 1987.

[65] M. Foskey, M. Garber, M. C. Lin, and D. Manocha, “A Voronoi-based hybrid motion planner,” in *Proceedings of the IEEE/RSJ International Conference on Intelligent Robots and Systems*, vol. 1, 2001, pp. 55–60.

[66] A. Gabdulkhakova and W. G. Kropatsch, “Confocal ellipse-based distance and confocal elliptical field for polygonal shapes,” in *Proceedings of the International Conference on Pattern Recognition*, 2018, pp. 3025–3030.

[67] A. Gabdulkhakova and W. G. Kropatsch, “Generalized conics: properties and applications,” in *Proceedings of the International Conference on Pattern Recognition*, 2020, pp. 10 728–10 735.

[68] A. Gabdulkhakova and W. G. Kropatsch, “Generalized conics with the sharp corners,” in *Proceedings of the Iberoamerican Congress on Pattern Recognition*, 2021, pp. 419–429.

[69] A. Gabdulkhakova, M. Langer, B. W. Langer, and W. G. Kropatsch, “Line Voronoi Diagrams using elliptical distances,” in *Proceedings of the Joint IAPR International Workshop on Statistical Techniques in Pattern Recognition and Structural and Syntactic Pattern Recognition*, 2018, pp. 258–267.

[70] W. Gellert, M. Hellwich, H. Kästner, and H. Küstner, *The VNR concise encyclopedia of mathematics.* Springer, 2012.

[71] G. Glaeser, H. Stachel, and B. Odehnal, *The Universe of Conics: From the ancient Greeks to 21st century developments.* Springer, 2016.

[72] C. Goerzen, Z. Kong, and B. Mettler, "A survey of motion planning algorithms from the perspective of autonomous UAV guidance," *Journal of Intelligent and Robotic Systems*, vol. 57, no. 1, pp. 65–100, 2010.

[73] R. Goldman, "Curvature formulas for implicit curves and surfaces," *Computer Aided Geometric Design*, vol. 22, no. 7, pp. 632–658, 2005.

[74] N. T. Gridgeman, "Lamé ovals," *The Mathematical Gazette*, vol. 54, no. 387, pp. 31–37, 1970.

[75] C. Groß and T.-K. Strempel, "On generalizations of conics and on a generalization of the Fermat-Torricelli problem," *The American Mathematical Monthly*, vol. 105, no. 8, pp. 732–743, 1998.

[76] M. Held, "VRONI: An engineering approach to the reliable and efficient computation of Voronoi diagrams of points and line segments," *Computational Geometry*, vol. 18, no. 2, pp. 95–123, 2001.

[77] D. Hilbert, *The foundations of geometry.* Open Court Publishing Company, 1902.

[78] D. Hilbert and S. Cohn-Vossen, "The cylinder, the cone, the conic sections, and their surfaces of revolution," in *Geometry and the imagination*, ser. AMS Chelsea Publishing. American Mathematical Society, 1999.

[79] S.-B. Ho and C. R. Dyer, "Shape smoothing using medial axis properties," *IEEE Transactions on Pattern Analysis and Machine Intelligence*, vol. 8, no. 4, pp. 512–520, 1986.

[80] F. K. Hwang, "An O($N\log N$) algorithm for rectilinear minimal spanning trees," *Journal of the ACM*, vol. 26, no. 2, pp. 177–182, 1979.

[81] S. Iglesias-Cofán and A. Formella, "Guided thinning," *Pattern Recognition Letters*, vol. 128, pp. 176–182, 2019.

[82] T. Imai, "A Topology oriented algorithm for the Voronoi diagram of polygons," in *Proceedings of the Canadian Conference on Computational Geometry*, 1996, pp. 107–112.

[83] A. Jaklič, A. Leonardis, and F. Solina, "Superquadrics and their geometric properties," in *Segmentation and recovery of superquadrics*. Springer, 2000, pp. 13–39.

[84] F. R. Johnston, J. E. Boyland, M. Meadows, and E. Shale, "Some properties of a simple moving average when applied to forecasting a time series," *Journal of the Operational Research Society*, vol. 50, no. 12, pp. 1267–1271, 1999.

[85] M. I. Karavelas, "A robust and efficient implementation for the segment Voronoi diagram," in *Proceedings of the International symposium on Voronoi diagrams in science and engineering*, 2004, pp. 51–62.

[86] M. I. Karavelas and M. Yvinec, "Dynamic additively weighted Voronoi diagrams in 2D," in *Proceedings of the European Symposium on Algorithms*, 2002, pp. 586–598.

[87] B. B. Kimia and K. Siddiqi, "Geometric heat equation and nonlinear diffusion of shapes and images," *Computer Vision and Image Understanding*, vol. 64, no. 3, pp. 305–322, 1996.

[88] R. Kimmel, D. Shaked, N. Kiryati, and A. M. Bruckstein, "Skeletonization via distance maps and level sets," *Computer Vision and Image Understanding*, vol. 62, no. 3, pp. 382–391, 1995.

[89] G. Kirchgässner, J. Wolters, and U. Hassler, *Introduction to modern time series analysis*. Springer, 2012.

[90] D. G. Kirkpatrick, "Efficient computation of continuous skeletons," in *Proceedings of the Annual Symposium on Foundations of Computer Science*, 1979, pp. 18–27.

[91] K. Kise, A. Sato, and M. Iwata, "Segmentation of page images using the area Voronoi Diagram," *Computer Vision and Image Understanding*, vol. 70, no. 3, pp. 370–382, 1998.

[92] C. O. Kiselman, *Elements Of Digital Geometry, Mathematical Morphology, And Discrete Optimization*. World Scientific, 2022.

[93] R. Klein and D. Wood, "Voronoi Diagrams based on general metrics in the plane," in *Proceedings of the Annual Symposium on Theoretical Aspects of Computer Science*, 1988, pp. 281–291.

[94] R. Klette and A. Rosenfeld, *Digital geometry: geometric methods for digital picture analysis.* Morgan Kaufmann, 2004.

[95] J. J. Koenderink, "The structure of images," *Biological cybernetics*, vol. 50, no. 5, pp. 363–370, 1984.

[96] Y. Kopsinis and S. McLaughlin, "Development of EMD-based denoising methods inspired by wavelet thresholding," *IEEE Transactions on Signal Processing*, vol. 57, no. 4, pp. 1351–1362, 2009.

[97] D. Kotsur and V. Tereshchenko, "Optimization heuristics for computing the Voronoi skeleton," in *Proceedings of the International Conference on Computational Science*, 2019, pp. 96–111.

[98] V. Kumar, J. K. Chhabra, and D. Kumar, "Performance evaluation of distance metrics in the clustering algorithms," *INFOCOMP Journal of Computer Science*, vol. 13, no. 1, pp. 38–52, 2014.

[99] G. Lamé, *Examen des différentes méthodes employées pour résoudre les problèmes de géométrie.* M$^{\text{ME}}$ V$^{\text{E}}$ Courcier, 1818.

[100] M. Langer, A. Gabdulkhakova, and W. G. Kropatsch, "Non-centered Voronoi Skeletons," in *Proceedings of the International Conference on Discrete Geometry for Computer Imagery*, 2019, pp. 355–366.

[101] J.-C. Latombe, *Robot motion planning*, ser. The Kluwer International Series in Engineering and Computer Science. Kluwer Academic Publishers, 1991, vol. 124.

[102] D.-T. Lee, "Two-dimensional Voronoi Diagrams in the L_p-metric," *Journal of the ACM*, vol. 27, no. 4, pp. 604–618, 1980.

[103] D.-T. Lee, "Medial axis transformation of a planar shape," *IEEE Transactions on Pattern Analysis & Machine Intelligence*, vol. 4, no. 4, pp. 363–369, 1982.

[104] T.-C. Lee, R. L. Kashyap, and C.-N. Chu, "Building skeleton models via 3-D medial surface axis thinning algorithms," *CVGIP: Graphical Models and Image Processing*, vol. 56, no. 6, pp. 462–478, 1994.

[105] F. F. Leymarie and M. D. Levine, "Simulating the grassfire transform using an active contour model," *IEEE Transactions on Pattern Analysis and Machine Intelligence*, vol. 14, no. 1, pp. 56–75, 1992.

[106] T. Lindeberg, "Scale-space theory: a basic tool for analyzing structures at different scales," *Journal of applied statistics*, vol. 21, no. 1-2, pp. 225–270, 1994.

[107] H. Liu, Z. Wu, D. F. Hsu, B. S. Peterson, and D. Xu, "On the generation and pruning of skeletons using generalized Voronoi Diagrams," *Pattern Recognition Letters*, vol. 33, no. 16, pp. 2113–2119, 2012.

[108] E. H. Lockwood, *A book of curves.* Cambridge University Press, 1961.

[109] S. Loncaric, "A survey of shape analysis techniques," *Pattern Recognition*, vol. 31, no. 8, pp. 983–1001, 1998.

[110] C. Lopez-Molina, B. De Baets, H. Bustince, J. Sanz, and E. Barrenechea, "Multiscale edge detection based on Gaussian smoothing and edge tracking," *Knowledge-Based Systems*, vol. 44, pp. 101–111, 2013.

[111] S. Mallat, *A wavelet tour of signal processing.* Elsevier, 1999.

[112] S. G. Mallat, "A theory for multiresolution signal decomposition: the wavelet representation," *IEEE Transactions on Pattern Analysis and Machine Intelligence*, vol. 11, no. 7, pp. 674–693, 1989.

[113] F. Malmberg, R. Strand, J. Zhang, and S. Sclaroff, "The Boolean Map Distance: theory and efficient computation," in *Proceedings of the International Conference on Discrete Geometry for Computer Imagery*, 2017, pp. 335–346.

[114] D. Marr and H. K. Nishihara, "Representation and recognition of the spatial organization of three-dimensional shapes," *Proceedings of the Royal Society B: Biological Sciences*, vol. 200, no. 1140, pp. 269–294, 1978.

[115] C. R. Maurer Jr., R. Qi, and V. Raghavan, "A linear time algorithm for computing exact Euclidean distance transforms of binary images in arbitrary dimensions," *IEEE Transactions on Pattern Analysis and Machine Intelligence*, vol. 25, no. 2, pp. 265–270, 2003.

[116] J. C. Maxwell, *The Scientific Letters and Papers of James Clerk Maxwell: Volume 1, 1846-1862*. Cambridge University Press, 1990.

[117] N. Mayya and V. T. Rajan, "Voronoi Diagrams of polygons: a framework for shape representation," *Journal of Mathematical Imaging and Vision*, vol. 6, no. 4, pp. 355–378, 1996.

[118] K. Mehlhorn, *Data Structures and Algorithms 3: Multi-dimensional searching and computational geometry*, ser. Monographs in Theoretical Computer Science. An EATCS Series. Springer, 1984.

[119] L. F. Mello and L. R. dos Santos, "On the location of the minimum point in the Euclidean distance sum problem," *São Paulo Journal of Mathematical Sciences*, vol. 12, no. 1, pp. 108–120, 2018.

[120] Z. A. Melzak and J. S. Forsyth, "Polyconics. I. Polyellipses and optimization," *Quarterly of Applied Mathematics*, vol. 35, no. 2, pp. 239–255, 1977.

[121] F. Meyer, "Cytologie quantitative et morphologie mathématiques," Ph.D. dissertation, École nationale supérieure des mines de Paris, 1979.

[122] M. Minsky and S. A. Papert, *Perceptrons: an introduction to computational geometry.* MIT Press, 1987.

[123] F. Mokhtarian and A. K. Mackworth, "Scale-based description and recognition of planar curves and two-dimensional shapes," *IEEE Transactions on Pattern Analysis and Machine intelligence*, vol. 8, no. 1, pp. 34–43, 1986.

[124] S. R. Moosavi, J. Qajar, and M. Riazi, "A comparison of methods for denoising of well test pressure data," *Journal of Petroleum Exploration and Production Technology*, vol. 8, no. 4, pp. 1519–1534, 2018.

[125] E. Moradi and M. Bidkhori, "Single facility location problem," in *Facility Location*, ser. Contributions to Management Science. Physica, 2009, pp. 37–68.

[126] M. Näf, G. Székely, R. Kikinis, M. E. Shenton, and O. Kübler, "3D Voronoi skeletons and their usage for the characterization and recognition of 3D organ shape," *Computer Vision and Image Understanding*, vol. 66, no. 2, pp. 147–161, 1997.

[127] Á. Nagy, “A short review on the theory of generalized conics,” *Acta Mathematica Academiae Paedagogicae Nyíregyháziensis*, vol. 31, no. 1, pp. 81–96, 2015.

[128] G. Németh, P. Kardos, and K. Palágyi, “Thinning combined with iteration-by-iteration smoothing for 3D binary images,” *Graphical Models*, vol. 73, no. 6, pp. 335–345, 2011.

[129] W. K. Nicholson, *Linear algebra with applications.* Lyryx Learning Inc., 2020.

[130] S. Nickel and E.-M. Dudenhöffer, “Weber’s Problem with Attraction and Repulsion under Polyhedral Gauges,” *Journal of Global Optimization*, vol. 11, no. 4, pp. 409–432, 1997.

[131] J. Nie, P. A. Parrilo, and B. Sturmfels, “Semidefinite representation of the k-ellipse,” in *Algorithms in Algebraic Geometry*, ser. The IMA Volumes in Mathematics and its Applications. Springer, 2008, vol. 146, pp. 117–132.

[132] J. Öfverstedt, J. Lindblad, and N. Sladoje, “Stochastic Distance Transform,” in *Proceedings of the International Conference on Discrete Geometry for Computer Imagery*, 2019, pp. 75–86.

[133] R. Ogniewicz and M. Ilg, “Voronoi skeletons: theory and applications,” in *Proceedings of the Conference on Computer Vision and Pattern Recognition*, 1992, pp. 63–69.

[134] R. L. Ogniewicz and O. Kübler, “Hierarchic Voronoi Skeletons,” *Pattern Recognition*, vol. 28, no. 3, pp. 343–359, 1995.

[135] A. Okabe, B. Boots, K. Sugihara, and S. N. Chiu, *Spatial tessellations: concepts and applications of Voronoi diagrams.* John Wiley & Sons, 2000.

[136] N. Okabe, J.-I. Toriwaki, and T. Fukumura, “Paths and distance functions on three-dimensional digitized pictures,” *Pattern Recognition Letters*, vol. 1, no. 4, pp. 205–212, 1983.

[137] A. Oldknow, “The Euler-Gergonne-Soddy triangle of a triangle,” *The American Mathematical Monthly*, vol. 103, no. 4, pp. 319–329, 1996.

[138] S. J. Orfanidis, *Introduction to signal processing.* Prentice-Hall, Inc., 1995.

[139] L. M. Ostresh Jr., "On the convergence of a class of iterative methods for solving the Weber location problem," *Operations Research*, vol. 26, no. 4, pp. 597–609, 1978.

[140] D. W. Paglieroni, "Distance transforms: properties and machine vision applications," *CVGIP: Graphical models and image processing*, vol. 54, no. 1, pp. 56–74, 1992.

[141] K. Palágyi and G. Németh, "1-attempt parallel thinning," *Journal of Combinatorial Optimization*, 2021.

[142] A. Paudel, J. Yang, and S. Puri, "Parallelization of Plane Sweep based Voronoi Construction with Compiler Directives," in *Proceedings of the IEEE Annual Computer Software and Applications Conference*, vol. 1, 2019, pp. 908–911.

[143] T. Pavlidis, "A review of algorithms for shape analysis," *Computer Graphics and Image Processing*, vol. 7, no. 2, pp. 243–258, 1978.

[144] S.-C. Pei and J.-H. Horng, "Finding the optimal driving path of a car using the modified constrained distance transformation," *IEEE Transactions on Robotics and Automation*, vol. 14, no. 5, pp. 663–670, 1998.

[145] O. Perry and J. Perry, *Mathematics I.* Palgrave Macmillan London, 1981.

[146] J. C. Peterson and R. D. Smith, *Mathematics for Machine Technology.* Cengage Learning, 2018.

[147] M. Petrović, B. D. Banjac, B. Malešević, and R. Mijailović, "Curve fitting by multifocal ellipses in architectural structures geometry," in *Proceedings of the International Scientific Conference on Geometry and Graphics–moNGeometrija*, 2016, pp. 160–164.

[148] M.-T. Pham, O. J. Woodford, F. Perbet, A. Maki, B. Stenger, and R. Cipolla, "A new distance for scale-invariant 3D shape recognition and registration," in *Proceedings of the International Conference on Computer Vision*, 2011, pp. 145–152.

[149] C. A. Pickover, *The math book: from Pythagoras to the 57th dimension, 250 milestones in the history of mathematics.* Sterling Publishing Company, 2009.

[150] S. M. Pizer, W. R. Oliver, and S. H. Bloomberg, "Hierarchical shape description via the multiresolution symmetric axis transform," *IEEE Transactions on Pattern Analysis and Machine Intelligence*, vol. 9, no. 4, pp. 505–511, 1987.

[151] F. P. Preparata and M. I. Shamos, *Computational geometry: an introduction*, ser. Monographs in Computer Science. Springer, 1985.

[152] R. Ramamurthy and R. T. Farouki, "Voronoi diagram and medial axis algorithm for planar domains with curved boundaries I. Theoretical foundations," *Journal of Computational and Applied Mathematics*, vol. 102, no. 1, pp. 119–141, 1999.

[153] D. Reem, "The geometric stability of Voronoi Diagrams with respect to small changes of the sites," in *Proceedings of the Annual Symposium on Computational Geometry*, 2011, pp. 254–263.

[154] J. R. Rice, "Weight function theory for three-dimensional elastic crack analysis," in *Proceedings of the Symposium on Fracture Mechanics: Perspectives and Directions*, 1989, pp. 29–61.

[155] W. Richards and D. D. Hoffman, "Codon constraints on closed 2D shapes," *Computer Vision, Graphics, and Image Processing*, vol. 31, no. 3, pp. 265–281, 1985.

[156] É. O. Rodrigues, "Combining Minkowski and Chebyshev: new distance proposal and survey of distance metrics using k-nearest neighbours classifier," *Pattern Recognition Letters*, vol. 110, pp. 66–71, 2018.

[157] A. Rosenfeld and J. L. Pfaltz, "Sequential operations in digital picture processing," *Journal of the ACM*, vol. 13, no. 4, pp. 471–494, 1966.

[158] A. Rosenfeld and J. L. Pfaltz, "Distance functions on digital pictures," *Pattern Recognition*, vol. 1, no. 1, pp. 33–61, 1968.

[159] P. L. Rosin and G. A. W. West, "Multi-scale salience distance transforms," in *Proceedings of the British Machine Vision Conference*, 1993, pp. 579–588.

[160] G. Rushton, *Optimal location of facilities.* COMPress, 1979.

[161] P. K. Saha, G. Borgefors, and G. Sanniti di Baja, "A survey on skeletonization algorithms and their applications," *Pattern Recognition Letters*, vol. 76, pp. 3–12, 2016.

[162] P. K. Saha, G. Borgefors, and G. Sanniti di Baja, *Skeletonization: theory, methods and applications.* Academic Press, 2017.

[163] P. K. Saha, B. B. Chaudhuri, and D. D. Majumder, "A new shape preserving parallel thinning algorithm for 3D digital images," *Pattern Recognition*, vol. 30, no. 12, pp. 1939–1955, 1997.

[164] P. V. Sahadevan, "The theory of the egglipse - a new curve with three focal points," *International Journal of Mathematical Education in Science and Technology*, vol. 18, no. 1, pp. 29–39, 1987.

[165] G. Sanniti di Baja, "Well-shaped, stable, and reversible skeletons from the (3, 4)-distance transform," *Journal of Visual Communication and Image Representation*, vol. 5, no. 1, pp. 107–115, 1994.

[166] G. Sanniti di Baja, "On medial representations," in *Proceedings of the Iberoamerican Congress on Pattern Recognition*, 2008, pp. 1–13.

[167] C. Sansone, D. Pucher, N. M. Artner, W. G. Kropatsch, A. Saggese, and M. Vento, "Shape normalizing and tracking dancing worms," in *Proceedings of the Joint IAPR International Workshop on Statistical Techniques in Pattern Recognition and Structural and Syntactic Pattern Recognition*, 2016, pp. 390–400.

[168] A. Savitzky and M. J. E. Golay, "Smoothing and differentiation of data by simplified least squares procedures," *Analytical chemistry*, vol. 36, no. 8, pp. 1627–1639, 1964.

[169] B. F. Schaudt and R. L. (Scot) Drysdale, III, "Multiplicatively weighted crystal growth Voronoi Diagrams," in *Proceedings of the Annual Symposium on Computational Geometry*, 1991, pp. 214–223.

[170] M. Schmitt, "Some examples of algorithms analysis in computational geometry by means of mathematical morphological techniques," in *Proceedings of the French Workshop on Geometry and Robotics*, 1988, pp. 225–246.

[171] T. Schreiber, “A Voronoi Diagram based adaptive k-means-type clustering algorithm for multidimensional weighted data,” in *Proceedings of the Workshop on Computational Geometry*, 1991, pp. 265–275.

[172] J. Sekino, “n-ellipses and the minimum distance sum problem,” *The American Mathematical Monthly*, vol. 106, no. 3, pp. 193–202, 1999.

[173] S. Sethia, M. Held, and J. S. B. Mitchell, “PVD: A stable implementation for computing Voronoi diagrams of polygonal pockets,” in *Workshop on Algorithm Engineering and Experimentation.* Springer, 2001, pp. 105–116.

[174] M. I. Shamos, “Problems in computational geometry,” Ph.D. dissertation, Yale University, 1978.

[175] M. I. Shamos and D. Hoey, “Closest-point problems,” in *Proceedings of the Annual Symposium on Foundations of Computer Science*, 1975, pp. 151–162.

[176] A. Sheffer, M. Etzion, A. Rappoport, and M. Bercovier, “Hexahedral mesh generation using the embedded Voronoi graph,” *Engineering with Computers*, vol. 15, no. 3, pp. 248–262, 1999.

[177] W. Shen, X. Bai, R. Hu, H. Wang, and L. J. Latecki, “Skeleton growing and pruning with bending potential ratio,” *Pattern Recognition*, vol. 44, no. 2, pp. 196–209, 2011.

[178] E. C. Sherbrooke, N. M. Patrikalakis, and E. Brisson, “An algorithm for the medial axis transform of 3D polyhedral solids,” *IEEE Transactions on Visualization and Computer Graphics*, vol. 2, no. 1, pp. 44–61, 1996.

[179] F. Y. Shih, *Image processing and mathematical morphology: fundamentals and applications.* CRC Press, 2009.

[180] K. Siddiqi, A. Shokoufandeh, S. J. Dickinson, and S. W. Zucker, “Shock graphs and shape matching,” *International Journal of Computer Vision*, vol. 35, no. 1, pp. 13–32, 1999.

[181] K. Siddiqi, S. Bouix, A. Tannenbaum, and S. W. Zucker, “Hamilton-Jacobi skeletons,” *International Journal of Computer Vision*, vol. 48, no. 3, pp. 215–231, 2002.

[182] T. Sikora, "The MPEG-7 visual standard for content description - an overview," *IEEE Transactions on Circuits and Systems for Video Technology*, vol. 11, no. 6, pp. 696–702, 2001.

[183] S. Smith, *Digital signal processing: a practical guide for engineers and scientists.* Elsevier, 2013.

[184] M. Smolik, V. Skala, and O. Nedved, "A comparative study of LOWESS and RBF approximations for visualization," in *International Conference on Computational Science and Its Applications*, 2016, pp. 405–419.

[185] F. Soddy, "The kiss precise," *Nature*, vol. 137, p. 1021, 1936.

[186] P. Soille, *Morphological image analysis: principles and applications.* Springer, 2004.

[187] P. G. Spain, "The Fermat point of a triangle," *Mathematics Magazine*, vol. 69, no. 2, pp. 131–133, 1996.

[188] V. Stelmashuk, "New approach to an underwater discharge simulation using elliptic coordinates," *AIP Advances*, vol. 10, no. 1, pp. 015 102.1–015 102.7, 2020.

[189] M. J. Sterling, *Trigonometry for dummies.* John Wiley & Sons, 2014.

[190] R. Strand, "Minimal paths by sum of distance transforms," in *Proceedings of the International Conference on Discrete Geometry for Computer Imagery*, 2016, pp. 349–358.

[191] R. Strzodka and A. C. Telea, "Generalized distance transforms and skeletons in graphics hardware," in *Proceedings of the Joint Eurographics - IEEE TCVG conference on Visualization*, 2004, pp. 221–230.

[192] A. Sud, N. Govindaraju, and D. Manocha, "Interactive computation of discrete generalized Voronoi Diagrams using range culling," in *Proceedings of the International Symposium on Voronoi Diagrams in Science and Engineering*, 2005, pp. 1–10.

[193] K. Sugihara, M. Iri, H. Inagaki, and T. Imai, "Topology-oriented implementation – an approach to robust geometric algorithms," *Algorithmica*, vol. 27, no. 1, pp. 5–20, 2000.

[194] G. Sz.-Nagy, "Tschirnhaus´sche Flächen und Kurven," *Acta Mathematica Academiae Scientiarum Hungarica*, vol. 1, pp. 167–181, 1950.

[195] H. Talbot and B. C. Appleton, "Elliptical distance transforms and the object splitting problem," in *Proceedings of the International Symposium on Mathematical Morphology*, 2002, pp. 229–240.

[196] T. Tayebi and H. F. Öztop, "Entropy production during natural convection of hybrid nanofluid in an annular passage between horizontal confocal elliptic cylinders," *International Journal of Mechanical Sciences*, vol. 171, p. 105378, 2020.

[197] A. C. Telea and J. J. van Wijk, "An augmented fast marching method for computing skeletons and centerlines," in *Proceedings of the Joint Eurographics-IEEE TCVG Symposium on Visualization*, 2002, pp. 251–259.

[198] E. Torricelli, "Opere di Evangelista Torricelli," *Edited by G. Vassura and G. Loria and G. Montanari*, vol. I/2, pp. 90–97, 1919.

[199] E. Torricelli, "Opere di Evangelista Torricelli," *Edited by G. Vassura and G. Loria and G. Montanari*, vol. III, p. 426–431, 1919.

[200] G. R. Veldkamp, "The isoperimetric point and the point(s) of equal detour in a triangle," *The American Mathematical Monthly*, vol. 92, no. 8, pp. 546–558, 1985.

[201] Cs. Vincze and Á. Nagy, "On the theory of generalized conics with applications in geometric tomography," *Journal of Approximation Theory*, vol. 164, no. 3, pp. 371–390, 2012.

[202] G. Voronoy, "Nouvelles applications des paramètres continus à la théorie des formes quadratiques. Deuxième mémoire. Recherches sur les parallélloèdres primitifs," *Journal für die reine und angewandte Mathematik*, vol. 134, pp. 198–287, 1908.

[203] J. Wang and M. Q.-H. Meng, "Optimal path planning using generalized Voronoi graph and multiple potential functions," *IEEE Transactions on Industrial Electronics*, vol. 67, no. 12, pp. 10 621–10 630, 2020.

[204] A. Weber, *Über den Standort der Industrien.* J. C. B. Mohr, 1922.

[205] G. O. Wesolowsky and R. F. Love, "Location of facilities with rectangular distances among point and area destinations," *Naval Research Logistics Quarterly*, vol. 18, no. 1, pp. 83–90, 1971.

[206] B. Williamson, "The properties of the Cartesian oval treated geometrically," *Hermathena*, vol. 2, no. 4, pp. 509–518, 1876.

[207] A. P. Witkin, "Scale-space filtering," in *Readings in computer vision: issues, problems, principles, and paradigms.* Elsevier, 1987, pp. 329–332.

[208] M. Yang, K. Kpalma, and J. Ronsin, "Shape-based invariant feature extraction for object recognition," in *Advances in Reasoning-Based Image Processing Intelligent Systems: Conventional and Intelligent Paradigms.* Springer, 2012, pp. 255–314.

[209] Y. Yang, J. Pan, and W. Wan, "Survey of optimal motion planning," *IET Cyber-systems and Robotics*, vol. 1, no. 1, pp. 13–19, 2020.

[210] C. K. Yap, "An O($N\log N$) algorithm for the Voronoi Diagram of a set of simple curve segments," *Discrete & Computational Geometry*, vol. 2, no. 4, pp. 365–393, 1987.

[211] C. K. Yap, "Towards exact geometric computation," *Computational Geometry*, vol. 7, no. 1-2, pp. 3–23, 1997.

[212] J. R. Young, *Elements of Geometry: With Notes.* Carey, Lea & Blanchard, 1833.

[213] D. Zhang and G. Lu, "Review of shape representation and description techniques," *Pattern Recognition*, vol. 37, no. 1, pp. 1–19, 2004.

[214] T. Y. Zhang and C. Y. Suen, "A fast parallel algorithm for thinning digital patterns," *Communications of the ACM*, vol. 27, no. 3, pp. 236–239, 1984.